Transient Current Technique characterization of bonded interfaces for monolithic silicon radiation detectors

THÈSE N^O 7451 (2018)

PRÉSENTÉE LE 16 NOVEMBRE 2018
À LA FACULTÉ DES SCIENCES ET TECHNIQUES DE L'INGÉNIEUR
GROUPE DE SCIENTIFIQUES IEL
PROGRAMME DOCTORAL EN MICROSYSTÈMES ET MICROÉLECTRONIQUE

ÉCOLE POLYTECHNIQUE FÉDÉRALE DE LAUSANNE

POUR L'OBTENTION DU GRADE DE DOCTEUR ÈS SCIENCES

PAR

Jacopo BRONUZZI

acceptée sur proposition du jury:

Prof. M. A. Ionescu, président du jury
Dr J.-M. Sallese, Dr A. Mapelli, directeurs de thèse
Dr M. Luciano, rapporteur
Dr F. Fournel, rapporteur
Prof. Ph. Renaud, rapporteur

EPFL

ÉCOLE POLYTECHNIQUE
FÉDÉRALE DE LAUSANNE

Suisse
2018

La semplicità è l'ultima sofisticazione.
- Leonardo da Vinci

Abstract

This thesis aims at demonstrating a novel technique for the characterization of interfaces obtained by a CMOS-compatible Surface Activated Bonding (SAB) process between silicon wafers. This enables the optimization of the two main components of monolithic silicon detectors, the CMOS circuitry for the read-out and the sensing layer, by fabricating them in different substrates and then by bonding them together. Therefore, to be collected by the read-out circuitry, charges generated by radiation in the bulk have to traverse the bonding interface, whose electrical properties need to be characterized.

The first part of this thesis is focused on the evaluation of Transient Current Technique (TCT) for this purpose. TCT is largely used for the study of radiation damage in silicon detectors, and consists in the injection of a localized cloud of electrons inside a detector based on a reverse-biased diode, that is drifted by the electric field. A transient current signal is generated, whose shape is related to the electric field profile that may be affected by lattice defects generated by radiation. In this context, the bonding process is expected to generate a thin amorphous silicon interface between the two bonded substrates. This layer can be seen as full of defects and therefore it is expected to influence the electric field, and the TCT current signal. This is demonstrated by means of Sentaurus TCAD numerical simulations and an analytical model, using a diode with the bonding interface in the middle of the bulk as test structure.

The second part of the thesis describes the characterization of the interface, generated by bonding high resistivity wafers at CEA-Leti in Grenoble. For this purpose, Schottky diodes are fabricated on these stacks at EPFL, and then characterized with CV, IV and TCT techniques. The results obtained are compared to simulation data, to show that the electric field did not extend to the bulk, preventing charges to be collected. This is an issue for the fabrication of radiation detectors, since there would not be collection of charges generated at the sensing bulk. Following these conclusions, two solutions are proposed. First, the optimization of the bonding process to reduce the number of traps. Second, a modification of the detector design in such a way that the bonding interface is located at the PN junction, since the electric field is maximum at this position, and therefore the influence of traps is less important.

The last part of this thesis is devoted to the description of a new charge injection technique for TCT measurements. Instead of using a laser, charges are injected by means of nanosecond voltage pulses, applied to dedicated wells fabricated on the PN junction contact. Injection occurs by thermionic emission, while the charges drift, as in standard TCT measurements. This novel method of charge injection is called electrical injection TCT (el-TCT). It could allow to perform on-line TCT measurements during experiments.

Sintesi

L'obiettivo di questa tesi è presentare un lavoro di caratterizzazione dell'interfaccia prodotta da un processo di bonding SAB (Surface Activated Bonding) compatibile con la tecnologia CMOS. Questo processo permetterebbe l'ottimizzazione delle due principali componenti dei sensori monolitici, attraverso la loro fabbricazione su due differenti tipi di wafer, poi fusi insieme: il circuito di read-out e il volume sensibile alle radiazioni. Le cariche, che normalmente vengono generate nel volume sensibile alla radiazione, devono essere raccolte dal circuito di read-out, e quindi passare attraverso l'interfaccia di bonding, ragione per cui la caratterizzazione delle sue proprietà elettriche è di fondamentale importanza.

La prima parte di questa tesi sarà dedicata alla valutazione della Transient Current Technique (TCT) a questo scopo. La TCT è largamente utilizzata per lo studio del danno da radiazione in sensori di silicio, e consiste nell'iniezione di una nuvola di cariche localizzata in un diodo in polarizzazione inversa, che viene trasportata dal campo elettrico. Ne risulta un segnale di corrente transitoria, la cui forma è legata a quella del profilo del campo elettrico, che puó essere influenzato dalla presenza di difetti nel reticolo cristallino. In studi precedenti è stato evidenziato il fatto che il processo di bonding genera una sottile interfaccia di silicio amorfo, che puó essere considerato come uno strato pieno di difetti nel reticolo cristallino, che puó quindi influenzare il campo elettrico e in ultima analisi il segnale TCT. Questo fenomeno viene dimostrato attraverso simulazioni di un diodo con l'interfaccia situata nel mezzo del suo volume, utilizzando il software Sentaurus TCAD e un modello analitico.

La seconda parte di questa tesi riguarda il metodo di caratterizzazione dell'interfaccia, generata in wafer di silicio ad alta resistività, fusi da CEA-Leti a Grenoble. Il metodo consiste nella fabbricazione di diodi Schottky sui wafer, e nello studio delle loro caratteristiche CV, IV e TCT, che combinato a simulazioni, dimostra che il campo elettrico non si estende al di là dell'interfaccia, bloccando di fatto la raccolta di cariche. Questo rappresenta un importante problema per i sensori di radiazione, dato che nel caso di una fabbricazione tramite il processo di bonding, questi non potrebbero raccogliere la carica generata. Per questo motivo vengono proposte due soluzioni: la prima consiste nell'ottimizzazione del processo di bonding, per ridurre il numero di difetti all'interfaccia, la seconda nella modifica del design del sensore in modo tale che la giunzione PN si trovi alla stessa posizione dell'interfaccia, avendo quindi il massimo del campo elettrico in quel punto, rendendo l'influenza dei difetti meno importante.

L'ultima parte di questa tesi riguarderà la descrizione di una nuova tecnica di iniezione di carica per misure TCT. In questo caso, al posto di un'iniezione di carica basata sull'utilizzo di un laser pulsato (tecnica standard), essa sarà basata sull'utilizzo di un impulso di tensione

lungo un nanosecondo, applicato a particolari contatti fabbricati sulla giunzione PN. Questa tecnica viene chiamata electrical injection TCT (el-TCT), e permetterebbe di effettuare misure TCT durante gli esperimenti.

Parole chiave: *Caratterizzazione di dispositivi in silicio, CERN, Compatibilità CMOS, Fisica dei semiconduttori, Microfabbricazione di silicio, Modello analitico e TCAD, Sensori di radiazione monolitici, SAB (Surface Activated Bonding), Transient Current Technique, Wafer bonding.*

Résumé

Cette thèse présente une étude portant sur la caractérisation électrique de l'interface qui est générée par un processus de collage SAB (Surface Activated Bonding) de wafers en silicium compatible avec la technologie CMOS. Celui-ci permettrait l'optimisation des deux composants du capteur monolithique de radiation réalisés sur deux substrats différents qui seront collés: un abritant le circuit CMOS pour la détection du signal, l'autre pour la zone de d'interaction avec les particules . Cependant, les charges générées par radiation dans le substrat doivent être collectées par le circuit CMOS, et donc passer à travers l'interface de collage. Il est donc essentiel que ses propriétés électriques de cet interface soient évaluées.

La première partie de ce travail sera dédiée à l'étude de la Transient Current Technique (TCT) en tant qu'outil de caractérisation. La TCT est largement utilisée pour évaluer les dommages de radiation dans les capteurs en silicium. Celle-ci est basée sur l'injection d'un nuage de charges localisé dans la zone de déplétion étendue d'une diode PIN polarisée en inverse. Ces charges sont ensuite transportées par le champ électrique créant un courant électrique. La forme de ce courant transitoire est liée au profil du champ électrique, lui-même influencé par la présence de défauts dans le réseau cristallin du silicium. Dans des études antérieures, il a été démontré que le collage covalent introduit une interface de silicium amorphe, qui peut être vue comme une couche ayant une forte concentration de défauts, et donc de pièges pour les porteurs de charge, ce qui peut influencer le champ électrique et donc le signal TCT. Cette hypothèse est démontrée en utilisant des simulations numériques réalisées avec l'outil Sentaurus TCAD, puis avec un modèle analytique, pour une diode où l'interface de collage est située dans le volume.

La deuxième partie de cette thèse est dédiée à la description de la méthode de caractérisation de l'interface généré par un collage réalisé par le CEA-Leti à Grenoble. Après la fabrication de diodes Schottky sur ces plaques, leurs caractéristiques CV, IV et TCT sont mesurées. Cette analyse conclue que le champ électrique est écranté par l'interface, et que les charges qui sont générées au delà ne peuvent plus être collectées. Ceci pourrait s'avérer être un problème majeur pour les capteurs de radiation qui ne pourront plus collecter les charges induites. Dans ce cas, deux solutions sont proposées. La première est l'optimisation du processus de collage pour réduire la présence de pièges à l'interface. La deuxième est le design du capteur de sorte que l'interface se situe au niveau de la jonction PN, là où le champ électrique est maximum et donc où l'influence des pièges est plus faible.

La troisième et dernière partie de cette thèse se consacre à la description d'une nouvelle technique pour réaliser l'injection des charges pour les mesures TCT. Au lieu d'utiliser une

lumière laser pulsée, comme dans les mesures standard, l'injection se base sur l'application de pulses de tension d'une durée d'une nanoseconde. Cette technique est appelée electrical injection TCT (el-TCT), et pourrait aider à réaliser des analyses TCT des capteurs pendant les expériences.

Mots-clés: *Capteurs de radiation monolithiques, Caractérisation de dispositifs en silicium, CERN, Collage de plaques en silicium, Compatibilité CMOS, Microfabrication en silicium, Modèle analytique et TCAD, Physique des semiconducteurs, SAB (Surface Activated Bonding), Transient Current Technique.*

Acknowledgments

PhD is a long path, during which you evolve and grow, both professionally and personally. I met many new people that, together with old friends and family, allowed me to have three stimulating and exciting years.

First of all, I would like to thank my supervisors: Professor Jean-Michel Sallese and Dr Alessandro Mapelli, for all the precious advices (both personal and professional) they gave me during these three years and for the continuous and friendly support. They taught me how to solve problems that seemed to be impossible at the beginning, with calm and lucidity. Without their guide, the work presented in this thesis could not be possible. I want also to thank them for having set up a friendly environment in the groups, a necessary condition to carry out successful project.

I would like to thank the jury members: Dr Luciano Musa, Dr Frank Fournel, Professor Philippe Renaud and Professor Mihai Adrian Ionescu, for the interest showed in my work and for the very interesting discussion during the defense. Moreover, I would like to thank them for their suggestions, helping me to considerably improve the thesis value.

My experience at CERN has been one of the most exciting and educational I had, thanks to all the people with whom I worked.

I would like to thank the Solid State Detectors group, headed by Michael Moll, who gave me essential advices for my work. Thanks to Matteo, Joaquin, Marcos, Laura, Sofia, William, Pedro, Esteban, Isidro, and all the other members, for helping me to solve difficult problems, and for the nice time I spent with them.

I would like also to express my gratitude to the IRRAD group: thanks to Federico Ravotti for the priceless advices and for giving me the possibility of having new working experiences in the radiation field. Thanks to him and to Georgi, Ina, Giuseppe (always available to help) for the friendship and kindness they showed me.

Thanks also to all the support I received from the Engineering Office: thanks to Diego, François, Jordan, Andrea, Francisco.

Thanks for the fundamental help I received from the people of the ALICE experiment: thanks to Luciano, Jacobus, Qasim, Petra, Walter.

And thank to my office mates at CERN, for the advices and the friendly environment: Guillaume, Adrien, Luca, Tiago, Clémentine, Riccardo.

Finally, I would like to thank Veronique for being always available and kind, and for helping me in all the administrative issues.

I would like to thank also all the people from CEA-Leti in Grenoble, for the very exciting

Contents

Contents

Contents

List of Figures

List of Tables

Nomenclature

Nomenclature

MM	Mini-matrix
MOS	Metal Oxide Semiconductor
SAB	Surface Activated Bonding
SRP	Spreading Resistance Profiling
SSD	Solid State Detectors
TCAD	Technology Computer-Aided Design
TCT	Transient Current Technique
TPA-eTCT	Two Photons Absorption edge TCT
TPC	Time Projection Chamber
UHV	Ultra High Vacuum

Constants

ϵ_0	Vacuum permittivity	[8.82×10^{-12} F/m]
ϵ_{Si}	Silicon relative permittivity	[11.68]
$\mu_{e,0}$	Low field electrons mobility in silicon	[1417 cm^2/Vs]
ξ	Exponential decay of diffusion in undepleted bulk	[0.0203 ns^{-1}]
A^*	Richardson constant	[1.20173×10^6 A/m^{2}K^2]
c	Light velocity	[3×10^8 m/s]
e	Electron charge	[1.6×10^{-19} C]
k_b	Boltzmann constant	[1.38×10^{-23} J/K]
m_e	Electron mass at rest	[9.10×10^{-31} kg]
$v_{sat,0}$	Saturation velocity at $T = 300$ K	[1.07×10^7 cm/s]

Variables

β	Particle velocity expressed as multiple of light velocity c	[-]
$\delta(\beta\gamma)$	density effect correction to ionization energy loss	[-]
γ	Lorentz factor, $\gamma = 1/\sqrt{1-\beta^2}$	[-]
λ_{LASER}	Laser wavelength	[nm]

$\left\langle \frac{dE}{dx} \right\rangle$	Mean rate of energy loss	[MeV cm^2/g]
μ	Charges drift mobility	[cm^2/Vs]
μ_e	Electrons mobility	[cm^2/Vs]
ω	Weigthing parameter	[-]
$\Phi_{B,-t}$	Potential barrier before voltage pulse	[eV]
$\Phi_{B,0}$	Potential barrier during voltage pulse	[eV]
Φ_B	Potential barrier	[eV]
Ψ	Electrostatic potential	[eV]
τ	Decay time constant	[s]
$\tau_{eff,e,h}$	Effective trapping times for electrons and holes	[s]
θ_{air}	Angle of incidence in air	[rad]
θ_{Si}	Angle of refraction in silicon	[rad]
ε	Electric field	[V/cm]
$\varepsilon(x_t^+)$	Electric field evaluated at the right of the traps layer	[V/cm]
$\varepsilon(x_t^-)$	Electric field evaluated at the left of the traps layer	[V/cm]
ε_w	Weighting electric field	[μm^{-1}]
Ξ	Scaling geometrical parameter to match TCAD and analytical model	[m C]
A	Atomic mass	[kg]
B	Amplification constant	[-]
$C_{B,n}$	Peak N-type doping concentration at surface on node B	[cm^{-3}]
$C_{C,n}$	Peak N-type doping concentration at surface on node C	[cm^{-3}]
$c_{n,a}$	Electrons capture coefficient for acceptors traps	[cm^{-3}/s]
$c_{n,d}$	Electrons capture coefficient for donors traps	[cm^{-3}/s]
$c_{p,a}$	Holes capture coefficient for acceptors traps	[cm^{-3}/s]
$c_{p,d}$	Holes capture coefficient for donors traps	[cm^{-3}/s]
C_{px}	Pixel input capacitance	[F]
C_p	Peak P-type doping concentration at surface	[cm^{-3}]

D_n	Diffusion constant	[cm^2/s]
d_t	Thickness of the traps layer	[nm]
d_{tot}	Detector total thickness	[μm]
$DL_{B,n}$	N-type doping Gaussian width at node B	[μm]
$DL_{C,n}$	N-type doping Gaussian width at node C	[μm]
DL_p	P-type doping Gaussian width	[μm]
E_F	Fermi level	[eV]
E_i	Intrinsic Fermi level	[eV]
E_v	Valence band energy level	[eV]
$E_{at,0}$	Acceptor traps energy level referred to valence band	[eV]
E_{at}	Acceptor traps energy level	[eV]
$E_{dt,0}$	Donor traps energy level referred to valence band	[eV]
E_{dt}	Donor traps energy level	[eV]
g	Degeneracy factor	[-]
i	Current	[A]
J	Emission current density	[A/m^2]
L	Distance between parallel plates in capacitor	[μm]
L_W	Lambert W function of x	[-]
N	Doping concentration	[cm^{-3}]
n	Distribution of electrons cloud	[cm^{-3}]
N_A	Concentration of acceptors	[cm^{-3}]
N_D	Concentration of donors	[cm^{-3}]
n_i	Intrinsic carriers concentration	[cm^{-3}]
N_t	Volume concentration of charged traps	[cm^{-3}]
n_{air}	Refractive index of air	[-]
$N_{at,0}$	Acceptor traps volume concentration	[cm^{-3}]
$N_{at,e}$	Charged acceptor traps volume concentration at equilibrium	[cm^{-3}]

$N_{at,oe}$	Charged acceptor traps volume concentration out of equilibrium	[cm^{-3}]
$N_{dt,0}$	Donor traps volume concentration	[cm^{-3}]
$N_{dt,e}$	Charged donor traps volume concentration at equilibrium	[cm^{-3}]
$N_{dt,oe}$	Charged donor traps volume concentration out of equilibrium	[cm^{-3}]
$N_{e,h}$	Number of generated electrons and holes	[-]
N_{eff}	Effective doping concentration	[cm^{-3}]
$n_{el,max}$	Maximum number of generated electrons	[-]
$n_{el/mV}$	Number of electrons per mV of voltage drop	[-]
n_{inj}	Number of injected electrons	[cm^{-2}]
n_{Si}	Refractive index of silicon	[-]
N_W	Width of N-type doped area	[μm]
P_W	Width of P-type doped area	[μm]
q	Charge	[C]
Q_{ev}	Charge generated by radiation interaction with silicon	[C]
Q_{in}	Injected charge	[C]
r	Position of the traveling charge inside the diode	[μm]
S	Spacing between P-type and N-type doped areas	[μm]
Sch_W	Schottky contacts width	[μm]
T	Temperature	[K]
t	Time	[s]
t_1	Time needed to reach position 0	[s]
t_2	Time needed to reach the end of the depletion region	[s]
t_n	Time needed to reach the traps layer	[s]
t_{end}	Time needed to reach the thickness of the N-type doped bulk	[s]
t_{pulse}	Pulse length	[ps]
t_{px}	Thickness of sensitive region of one pixel	[μm]
Th	Device thickness	[μm]

V	Voltage	[V]
$v(t)$	Time dependent velocity	[m/s]
V_{-x_L}	Voltage applied to the P+ side of PiN diode	[V]
$V_{5.9}$	Voltage drop due to 5.9 keV photons	[V]
V_{AC}	Voltage difference between nodes A and C	[V]
V_{bb}	Back bias voltage	[V]
$V_{bias,B}$	Bias voltage applied to node B	[V]
$V_{bias,C}$	Bias voltage applied to node C	[V]
V_{bi}	Built in potential	[V]
V_{bulk}	Bias voltage applied to bulk in light injection TCT	[V]
V_{ev}	Voltage drop due to interaction with radiation particle	[V]
V_{fd}	Full depletion voltage	[V]
v_{sat}	Saturation drift velocity	[cm/s]
$V_{trans,B}$	Voltage pulse applied to node B	[V]
V_{x_R}	Voltage applied to the N+ side of PiN diode	[V]
W	Depth of a diode depletion region	[µm]
W_t	Width of depletion region generated by traps layer	[µm]
$x(t)$	Time dependent position	[µm]
x_L	Front side contact position of diode	[µm]
x_n	Depletion region edge in N-type doped silicon	[µm]
x_p	Depletion region edge in P-type doped silicon	[µm]
x_R	Back side contact position of diode	[µm]
x_t	Position of the traps layer	[µm]
x_{end}	Thickness of the N-type doped bulk	[µm]
Z	Atomic number of absorber material	[-]
z	Charge of incident particle	[C]

1 Introduction

The work presented in this thesis concerns two main topics. The first one deals with the characterization of electrical properties of thin interfaces inside silicon bulk, generated by a CMOS-compatible, low temperature silicon covalent bonding process, to study the feasibility of using this process for the fabrication of silicon pixel detectors for CERN experiments. For this purpose, the Transient Current Technique (TCT) , largely used for the assessment of radiation damage in silicon detectors, is selected. The work on TCT led to the realization of a new device to perform measurements with this technique, that is the second topic of this thesis. The chapters structure is the following:

Chapter 1: This is the introduction chapter. It summarizes the history of CERN and then introduces silicon radiation detectors, with a focus on pixel detectors. After this, an analysis of low temperature silicon bonding processes and a description of different kinds of TCT measurements are proposed.

Chapter 2: In this chapter, the study of TCT measurements applied to the characterization of bonding interfaces is described with the aid of Technology Computer-Aided Design (TCAD) analysis and the development of an analytical model to study the physics behind TCT in this particular case.

Chapter 3: In this chapter, measurements and characterization of thin bonding interfaces by means of TCT on Schottky diodes are performed, introducing a method that can be used for any case in which characterization of thin interfaces in bulk silicon need to be performed.

Chapter 4: In this chapter, the development of a new TCT method, to perform measurements with a setup simpler than the standard one, and to implement in-situ characterization of detectors during their use in experiments, is described.

Chapter 5: In this last chapter, conclusions about this thesis are drawn, and outlooks for future developments are listed.

1.1 CERN and HEP experiments

The first idea of a european atomic laboratory in which scientists from different countries could work together was conceived in 1949. The location for this laboratory was chosen to be the Meyrin site in Switzerland, where construction started in 1954. The European Organization for Nuclear Research (CERN, from the french name Conseil Européen pour la Recherche Nucléaire), was born in the same year, for the study of particle physics with high energy physics (HEP) experiments [1]. An HEP experiment consists in the collision of particles that have been previously accelerated, that generate radiation [2]. Tracking its position and energy using radiation detectors, that will be introduced in the next section, allows the study of the composition and nature of matter, and the origins of universe. The start-up of the first CERN accelerator, the synchrocyclotron, that provided the beams for the CERN first experiments, was in 1964. After this, the number of CERN accelerators started to increase, leading to the important discoveries carried on in this research center (the first observation of antinuclei in 1965, the discovery of particles related to weak interaction in 1983, the production of the first antiatom, the antihydrogen, in 1995). Following these results, in 1994 the construction of the biggest accelerator, the Large Hadron Collider (LHC), was approved, to reveal the physics beyond the Standard Model with center of mass collision energies of up to 14 TeV [3]. HEP experiments using this machine started to be designed. In 1997, two important general purpose experiments, designed to explore the fundamental nature of matter, were approved, CMS (Compact Muon Solenoid) [4] and ATLAS (A Toroidal LHC ApparatuS) [5]. Two other experiments were approved in 1997 and 1998, respectively the ALICE (A Large Ion Collider Eperiment) experiment, for the study of physics of strongly interacting matter at extreme energy densities [6][7], and the LHCb (Large Hadron Collider beauty experiment), to explore the universe evolution in the instants after the Big Bang occurred [8][9]. The construction of LHC, in figure 1.1, started in 2000 [10].
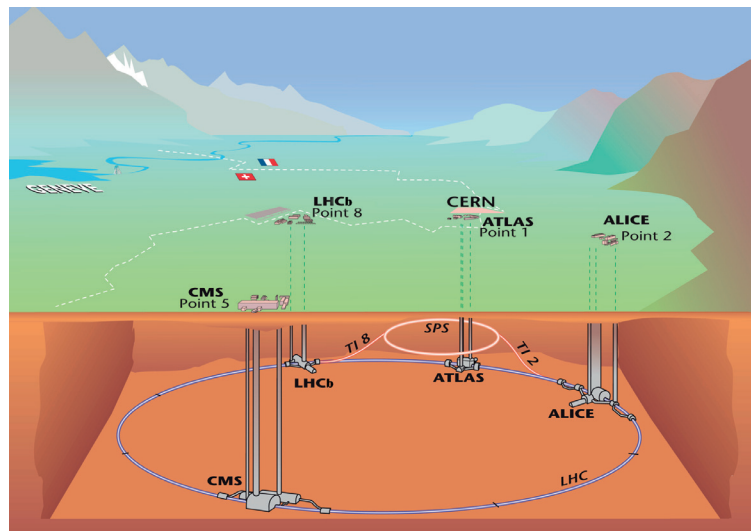
Figure 1.1 – View of the accelerators complex at CERN [11].

From a technological point of view, this is a very challenging machine. Indeed, the highest

luminosity (ratio of the number of events detected per second versus the interaction cross section) required for experiments is 10^{34} cm^{-2}s^{-1}, and to achieve these values, the needed magnetic field (to allow the circular path of charged particles inside the accelerator ring) is 8.33 T. Moreover, an enormous amount of energy (more than 1 GJ) is stored inside the machine (energy that needs to be dissipated at the end of each run) [10]. Data analysis in HEP physics is also a challenge, considering that experiments have a very high data rate generated by the detectors during runs. In HEP experiments, radiation detectors apparatus are disposed around the collision point. Figure 1.2 shows the composition of the ALICE experiment, where it is possible to observe examples of radiation detectors: the Inner Tracking System (ITS, made of silicon detectors, for particle tracking), the Time Projection Chamber (TPC, a gaseous detector for particle tracking and identification) [13], and the ElectroMagnetic Calorimeter (EMCal, a scintillation detector to study the physics fo jet quenching) [7]. The biggest achievement obtained thanks to LHC, has been the discovery of a new particle in 2012, the Higgs boson [1]. This was the confirmation of the theory of Robert Brout, Francois Englert and Peter Higgs, that explains the origin of the mass of subatomic particles as the result of the interaction with the Higgs field, whose visible manifestation is therefore the Higgs boson [14].
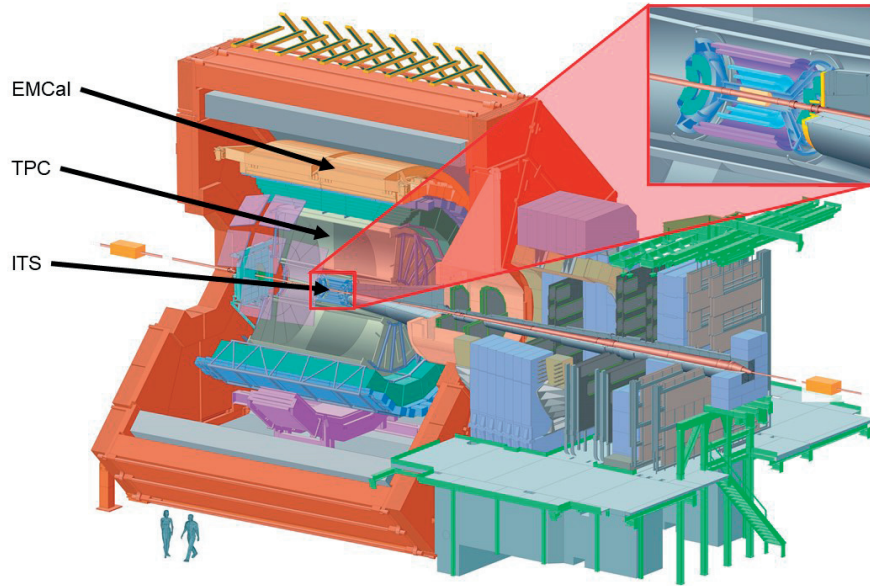
Figure 1.2 – Scheme of the ALICE experiment apparatus, with different types of radiation detectors: silicon detectors (ITS), gas detectors (TPC), scintillation detectors (EMCal) [7].

1.2 Radiation detectors

Radiation detectors are devices that convert the energy of a particle (whose passage is called event) into an electrical signal [15]. Radiation particles are divided in two main categories: charged (fast electrons, heavy charged particles) and uncharged (Neutrons and electromagnetic radiation). Radiation detectors can operate in three different modes: the pulse mode, the current mode and the mean square voltage mode. In pulse mode, each event is detected,

generating a current pulse. At high event rates, this mode becomes impractical. The current mode is based on recording the current from events in a fixed integration time. The mean square voltage mode is based on filtering the average integrated current and detecting only the fluctuating signal [15]. Pulses amplitude is realted to the energy and the type of particle that causes the event. Therefore, one of the outputs from this kind of detectors is the amplitude distribution of pulses. Important properties of radiation detectors are the threshold level for detection (a property of the counter circuit, that is the minimum pulse amplitude for the event to be detected), energy resolution (that is how much the output energy distribution from a monoenergetic radiation source is wide), detection efficiency (that is the numebr of recorded pulses versus the number of impinging particles) and the dead time (that is the minimum time needed between two subsequent events to be detected)[15]. Different radiation detectors are available for HEP experiments:

- **Ionization chambers:** detectors filled of gas (as the TPC in figure 1.2), that is ionized by the passage of a particle. The resulting charge is collected using an electric field.

- **Scintillation detectors:** based on the use of materials that generate light once traversed by a radiation particle. Light is then collected by photodetection devices [15]. An example is the EMCAL in figure 1.2.

- **Semiconductor radiation detectors:** based on the use of devices fabricated with semiconductors as silicon, that is the most used (as the ITS in figure 1.2). They present important advantage with respect to the other types: they are much more compact than gas filled detectors, and they present better energy resolution than scintillation detectors [15].

Since the topic of this thesis is related to silicon pixel detectors, the following sections will be focused in the introduction of this particular kind of radiation detectors.

1.2.1 Silicon radiation detectors

Silicon radiation detectors have been studied since the early 1960s, due to their high energy and spatial resolution, linearity of characteristics over a wide range of particles energy, possibility of realizing experiments geometries, insensitivity to magnetic fields, working capacity at low temperatures, compact design, mechanical strength, etc. [16][17]. The possibility of using silicon detectors for HEP experiments has been demonstrated since 1965, and then studied for many particle accelerators since 1970s. Advancements in development of fabrication processes and electronics design led to the possibility of implementing silicon in position-sensitive detectors [16].

Particles interaction with silicon detectors

To understand the behavior of a silicon detector, it is necessary to know how the energy is transferred from the impinging particle. Particles traveling inside a material lose energy along their path due to interactions with atoms, that depend on the particle type.

- In case of neutrons, it is possible to observe interactions only with atomic nuclei, and not with orbital electrons. Two different interactions are possible: elastic scattering (where the neutron is scattered by a nucleus, whose structure is not modified and could be left in an excited state due to recoil velocity, leading to the release of gamma radiation) and inelsastic scattering (where the neutron is captured by the nucleus, leading to radiation generation or fission).

- In case of heavy charged particles, interactions are mostly with electrons surrounding the nucleus. This leads to excitation of electrons, or ionization, in case the electron gains enough energy to escape from the atom. These interactions cause energy loss of the particle traveling inside silicon. Once the majority of the energy is lost, elastic collision with nuclei could occurs [18]. For heavy charged particles, the energy loss (or stopping power) along the track is described by the Bethe equation (1.1) [19].

$$-\left\langle \frac{dE}{dx} \right\rangle = K z^2 \frac{Z}{A} \frac{1}{\beta^2} \left[\frac{1}{2} ln \frac{2 m_e c^2 \beta^2 \gamma^2 T_{max}}{I^2} - \beta^2 - \frac{\delta(\beta\gamma)}{2} \right] \qquad (1.1)$$

Where $\left\langle \frac{dE}{dx} \right\rangle$ is the mean rate of energy loss, z is the charge of the incident particle, Z is the atomic number of absorber material, A is the atomic mass, β is the particle velocity expressed as multiple of light velocity c, m_e is the electron mass at rest, c is the light velocity, γ is the Lorentz factor, $\gamma = 1/\sqrt{1-\beta^2}$, $\delta(\beta\gamma)$ is the density effect correction to ionization energy loss. An example of the behavior of stopping power with the particle momentum (or kinetic energy) in case of a positive muon in copper is shown in figure 1.3.

- In case of fast electrons, the Bethe formula should be modified, since they could lose energy also by radiative processes (bremsstrahlung or electromagnetic radiation) [15].

- In case of electromagnetic radiation (X-rays and gamma rays), they are completely absorbed by the material, exciting electrons.

Electrons excitation results in the generation of electrons holes pairs. Radiation detectors are designed in such a way that these pairs are generated in a region where an electric field is present, or close to it. Therefore, they are drifted by the field, generating a current that is then detected by read-out electronics [15].
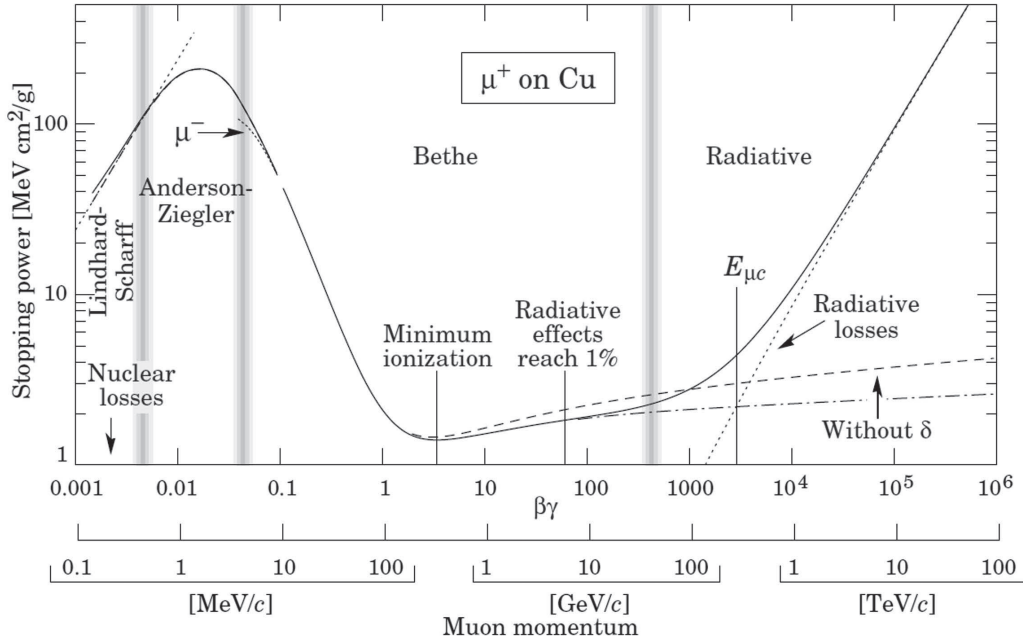
Figure 1.3 – Stopping power of positive muons in copper. The Bethe function predict the stopping power for a range between 10 MeV/c and 10 GeV/c.

Radiation damage in silicon

The energy transferred to the silicon substrate of a detector generates the electrons holes pairs needed for the detection, but also damages the material. Two type of radiation damages are possible: atomic displacement (where silicon atoms are displaced from their position inside the cystalline lattice) and ionization. Common defects caused by atomic displacement in silicon are the Frenkel pairs, consisting in a couple of so-called intrinsic defects, a vacancy (the absence of a silicon atom in the crystalline lattice) and an interstitial (the presence of an atom, in this case silicon, in normally unoccupied positions of the lattice) [20]. Defects could aggregate, generating groups that behaves in a different way compared to the single defect, such as dual vacancies [21] and dual interstitials [22]. Moreover, they can aggregate with impurities inside silicon, such as oxygen, phosphorus, boron. Many of these defects are electrically active, introducing energy level inside the silicon forbidden energy band. These levels are responsible for recombination processes, trapping, change of effective doping concentration in silicon bulk, and therefore also of the electric field profile [23]. Ionization consists in the generation of electron hole pairs [20]. In silicon detectors, this is not a problem since it is the mechanism through which particle detection occurs, while this could be a problem for dielectrics, since charges generated in these materials could be trapped [24], generating a fixed charge that influences the properties of electronics devices [20]. A category of silicon detectors used for particle tracking are the pixel detectors, whose fabrication is of interest in this thesis.

1.2.2 Pixel detectors

Silicon pixel detectors are commonly used for the detection of radiation in particle physics and imaging applications [25], as well as in the biomedical field [26]. They are fast (able to take millions of picture per second), allowing to detect short-lived particles, matching the requirements for HEP experiments at CERN [27]. The operation of a pixel detector is based on the reverse bias configuration of a PiN (or NiP) diode, composed of an high doped P-type (or N-type) implant, and a low doped N-type (or P-type) bulk, also called high resistivity bulk, that is the sensor part of the detector. In reverse bias configuration, it is depleted up to a depth W that depends on the applied voltage following equation (1.2).

$$W = \sqrt{2\epsilon_0 \epsilon_{Si} \left(\frac{V}{eN} \right)} \tag{1.2}$$

Where ϵ_0 is the vacuum permittivity, ϵ_{Si} is the silicon relative permittivity, V is the applied voltage, e is the electron charge and N is the doping concentration in the high resistivity bulk. Particles crossing the detector will generate charge carriers, that themselves generate a current pulse, detected by the read-out electronics, in case they are collected by the electrode of the diode. Collection can occur in two ways: by drift, if charges are generated inside the depletion region (short collection time), or by diffusion, if they are generated outside the depletion region (long collection time, and therefore they are more subjected to recombination). Figure 1.4 shows the cross section of a pixel detector and the two collection mechanisms [27]. As explained in section 1.2.1, radiation damages increase recombination rate in silicon [28], and a slow charge collection leads to charge, and therefore signal, loss. A detector based on diffusion collection is therefore less radiation hard than drift [29]. Two main approaches can be followed when manufacturing pixel detectors, the hybrid approach and the monolithic approach [27].

Hybrid pixel detector

Hybrid pixel detectors (in figure 1.4) consist in devices where the sensor matrix and the read-out electronics are fabricated on two different substrates and then matched, typically by bump bonding [27]. The reverse bias is usually applied on the back side of the detector, while the front side is connected to ground. Hybrid pixel detectors are radiation hard, with an high signal to noise ratio close to 100, and provide high space resolution in three dimensions and high time resolution [27]. This has been shown to work in HEP experiments [31]. Examples of hybrid pixel detectors are the MEDIPIX chip (for X-ray radiography) [34] and the Medipix 2 SINGLE chip [35], in which a CdTe sensor is used [26]. Capacitive coupled hybrid detectors have been also proposed. In this case, the signal can be transmitted from the sensor to the read-out electronics through capacitive coupling, avoiding expensive bump bonding [33].

Monolithic pixel detector

Monolithic pixel detectors integrate the detection sensor and the read-out electronics on the same substrate and technological process (see figure 1.5) [27]. This avoids the high density of interconnections, allows to lower the noise and it is a more robust solution. Since both parts share the same bulk, two different cases are possible: one in which the sensor drives
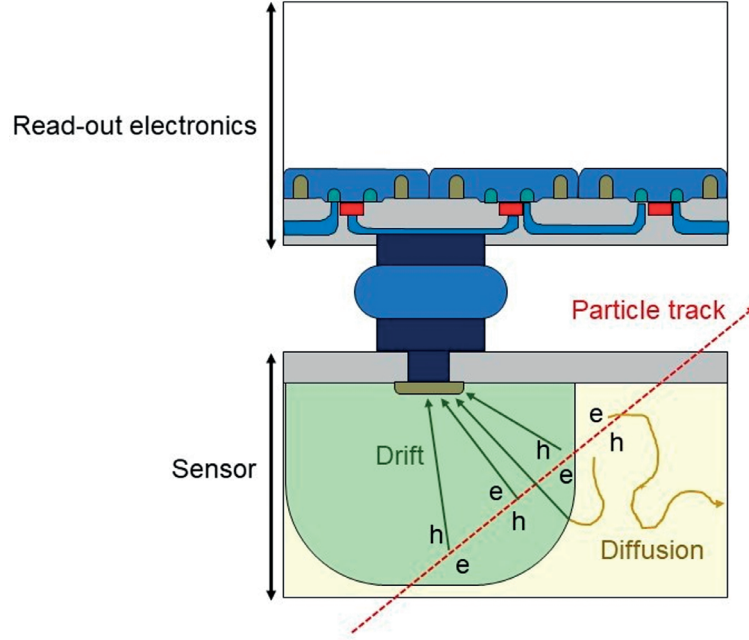
Figure 1.4 – Cross section of an hybrid pixel sensor. The read-out electronics is connected through a bump bonding to the sensor. Charge generated by the passage of a particle is collected by drift inside the depletion region, in green inside the sensor. Diffusing charges follow a random path, and they are collected only when they reach the depletion region (adapted from Petra Riedler [30]).

the development, and one in which the read-out electronics drives the development [27]. An example of a monolithic detector is the DEPFET (DEPleted Field Effect Transistor) design [36]. In this case, the bulk is chosen to be of high resistivity type. Therefore, the width of the depletion region is large, and drift collection occurs. However, since the existing read-out electronics device has been developed for low resistivity silicon bulks, it is necessary to perform a considerably design effort for this part of the detector [27]. Another is the Monolithic Active Pixel Sensor (MAPS) [37]. The first prototype was fabricated on a low resistivity silicon, and therefore the depletion region width was smaller than in the previous case [27]. The charge collection relied therefore on diffusion (low radiation tolerance). A MAPS design that results into an higher radiation tolerance is composed by a high resistivity epitaxial silicon layer deposited on a low resistivity silicon wafer. Even if in this case the detector is not fully depleted, and charge collection by diffusion is higher than in other cases [29]. However, the depletion region is larger, leading to a higher radiation tolerance [38]. This design has been proposed for the ALICE ITS upgrade [39]. Another CERN experiment for which monolithic pixel detectors have been chosen for future applications is ATLAS. The HVCMOS (High Voltage CMOS) represents a possibility for the ATLAS Phase-II upgrade [33]. The term high voltage refers to the fact that for this particular design, the working voltage for transistors is higher than the standard voltage applied in CMOS applications. The substrate is a P-type doped silicon, and transistors are fabricated on a deep N-type doped well, to which high voltage is applied
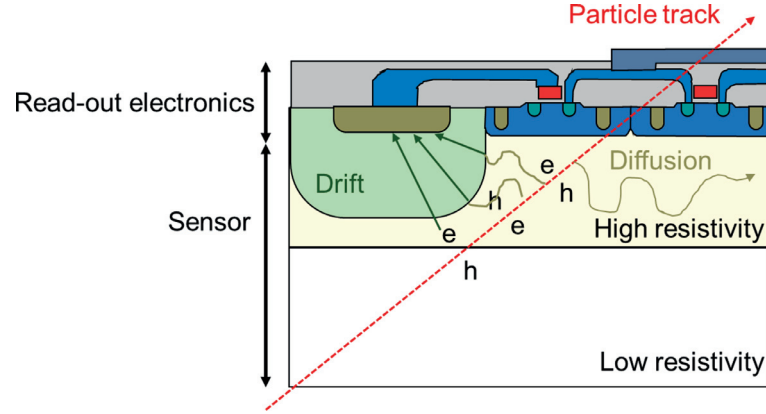
Figure 1.5 – Cross section of a monolithic pixel sensor. The read-out electronics is integrated inside the same bulk of the sensor. Collection by drift occurs inside the depletion region, in green, while collection by diffusion occurs outside this region (adapted from Petra Riedler [30]).

(50 V). PMOS are fabricated directly inside the deep N-type doped well, while NMOS are fabricated on a P-type doped well implanted in the deep well. Charge collection occurs at the junction between the deep N-well and the P-type substrate [32]. Another monolithic design investigated by ALICE and then by ATLAS for the outer layer of the Inner Tracker is a modified version of the MAPS, where a N-type doped layer is added under the CMOS electronics and the N-type collection electrode. In this way, depletion of the P-type silicon immediately start along the entire width of the pixel [40, 41]. After all these considerations, it is possible to conclude that an important issue related to monolithic pixel detectors is the choice of the silicon type for the their fabrication. In order to have the same flexibility of hybrid detectors, and therefore to have low resistivity silicon wafers for read-out electronics and high resistivity silicon for the sensor, one alternative process flow is to fabricate separately the two components on different silicon wafers, and then bonding them to obtain a monolithic-like device. The next section will analyze some silicon bonding technique for this purpose.

1.3 Silicon wafer bonding

The bonding process for the fabrication of pixel detectors includes a wafer with CMOS electronics, therefore bonding temperatures should not exceed the melting temperature of aluminium (660.32°C [42]), since it is one of the most used metals in CMOS technology. Temperatures below 450°C can be considered safe for this purpose [43]. In the next sections, various techniques for silicon bonding are summarized, focusing on safe process temperatures.

1.3.1 Fusion silicon bonding

Fusion silicon bonding is the most diffused technique to perform direct bonding between two different silicon wafers. Surfaces to be bonded need to be clean (free of organic or metallic particles that affect the mechanical and electrical properties of the resulting substrate), flat, parallel and smooth. During the bonding process, surfaces are subjected to processing such as

dip into acid solutions or exposed to plasma [44], that influence the adherence of wafers [43], and then placed in contact. Wafers are annealed at temperatures up to 1100°C. Two standard surface treatment are possible: the hydrophobic and the hydrophilic treatments (that gives the name to the corrensponding bonding processes).

Hydrophobic bonding

Hydrophobic treatment consists in deeping wafers into a HF (hydrofluoric acid) solution, to eliminate any presence of silicon dioxide. After this treatment, silicon atoms at the surfaces are connected to hydrogen atoms, constituting electric dipoles [45]. Once in contact, a pressure is applied [46], and wafers adhesion is mainly due to dipole-dipole van der Waals forces [45]. To increase the bonding strength, it is necessary to anneal the bonded wafers at temperatures higher than the room temperature. The effect of annealing is the conversion of weaker bonds between the two silicon surfaces into covalent bonds [47]. After annealing, dislocations are generated at the bonding interface due to matching of differences between the crystalline lattices of the two wafers. The value of bonding strength increases from 0.03 J/m^2 without annealing to 3 J/m^2 with annealing at 900°C, that however cannot be used for the fabrication of pixel detectors. Annealing at temperatures lower than 400°C does not change the bonding strength from the value obtained at room temperature [45]. This is not optimal for the purpose of monolithic detectors fabrication.

Hydrophilic bonding

Bonding with hydrophilic surface treatment is easier than the hydrophobic bonding [46]. The bonding occurs between two hydrophilic (with silicon oxide) silicon surfaces, that are placed in contact without pressure applied. At room temperature, the bonding strength reaches values higher than 0.13 J/m^2, much stronger than in the case of hydrophobic bonding. To reach higher bonding strength, higher annealing temperatures are needed [48]. Another possibility is to activate the surface with a chemical solution or a plasma [44]. Wafers bonded with oxygen plasma activation and not subjected to annealing reached bonding strength up to 0.85 J/m^2 [49]. The issue related to the use of this technique for the fabrication of pixel detectors is that a silicon oxide layer is present at the bonding interface. This would impede the electrical connection between the two components of the detector.

1.3.2 Intermediate layer silicon bonding

A different strategy to bond silicon at low temperature is the use of intermediate layers.

Sodium silicate bonding

Sodium silicate bonding interests two oxidized wafers, that are first subjected to a hot nitric acid treatment, to generate an hydrophilic surface. Then wafers are spin coated with a sodium silicate water solution, placed in contact and finally annealed at temperatures above 200°C. This process allows to obtain a high bonding strength at temperatures that are compatible with CMOS circuitry (for annealing at 400°C, bonding strength of 3 J/m^2 is reached) [50]. However, the presence of an interface layer could affect the electrical behavior of a silicon detector

fabricated with this technique.

Glue and glass bonding

Another strategy for a low temperature bonding is to use a glue. Glue bonding consists in spinning a polymeric material on the wafers surface and then, while wafers are in contact, curing it to obtain the bond. This technique is poor in reproducibility, and outgassing products could cause corrosion. Moreover, the glue layer thermal instability and moisture penetration represent an issue for the process. Another possibility is the use of glasses with low softening temperatures (such as glass number 7570). Also in this case, the poor control of the thickness of the glass layer is a problem for this technique [51]. Both the techniques cannot be used if electrical connection between the bonded components is needed.

Eutectic silicon bonding

Eutectic bonding is used to bond dies to packaging. A silicon die is placed on the package that has been coated with a gold layer. By applying a contact force and increasing the temperature over 363°C (gold-silicon eutectic temperature), the gold-silicon eutectic compound is formed, from the diffusion of silicon into the gold layer, generating a bond between the die and the package. A similar process can be performed to achieve wafer bonding. In this case, gold is deposited on silicon wafers that are subsequently placed in contact and heated up to a temperature higher than the eutectic temperature [52]. In this case, the presence of gold could affect the electrical properties of the detector, since gold is a dopant for silicon [53].

1.3.3 Low temperature Surface Activated Bonding (SAB)

To obtain a low temperature silicon bonding, another possibility, that would not require additional intermediate layers, and would lead to reconstruct covalent bonding between silicon atoms at the interface, is to use an ultra high vacuum (UHV) apparatus during the bonding process[47]. First tests on germanium [54] showed that it is possible to obtain covalent bonds with UHV setups [47]. Hydrophobic silicon surface reconstruction has also been demonstrated at room temperature. In this case, wafers surfaces were first dipped into HF to eliminate oxide, then annealed with temperatures cycles between 600 and 800°C to eliminate hydrogen. Since they were in UHV environment, surfaces were not oxidized, with dangling bonds, and therefore they could be bonded by simply placing them in contact at room temperature, under pressure. The bonding process was therefore propagating along the wafer surface, obtaining a pure silicon interface, with crystalline defects due to lattice mismatch between the two substrates [55]. A room temperature bonding process was demonstrated by Suga et al. [56], based on surface activation by plasma etching (SAB). Takagi et al. [57] demonstrated a SAB with argon plasma at room temperature for silicon, resulting into a strength higher than in case of standard bonding. A CMOS-compatible conductive SAB has been demonstrated by Flötgen et al.[58], using a EVG® 580 ComBond® machine with different annealing temperatures between 100°C and 300°C were tested. Wafer were first placed into a surface treatment module to remove native oxide and minimize the damage to the bulk silicon. Then bonding was performed by pressing at 0.06 MPa and annealing at the same time

the samples, for 60 minutes. For annealing temperatures higher than 200°C, the bulk fracture strength of silicon was reached (5 J/m^2). Moreover, after a first bonding inside the EVG® 580 ComBond®, annealing of the samples could be performed inside or outside the machine without any observed difference. Energy dispersive X-ray spectroscopy (EDXS) was performed at the bonding interface, and no trace of silicon oxide was observed. Therefore the interaface was oxide-free, and conductive. HR-TEM (High Resolution Trasmission Electron Microscopy) showed an amorphous silicon layer at the bonding interface, with a thickness of 2.6 nm [58]. Stacking of thin silicon wafers by fusion bonding at low temperature was demonstrated by Burggraf et al. [59], following the process shown in figure 1.6.
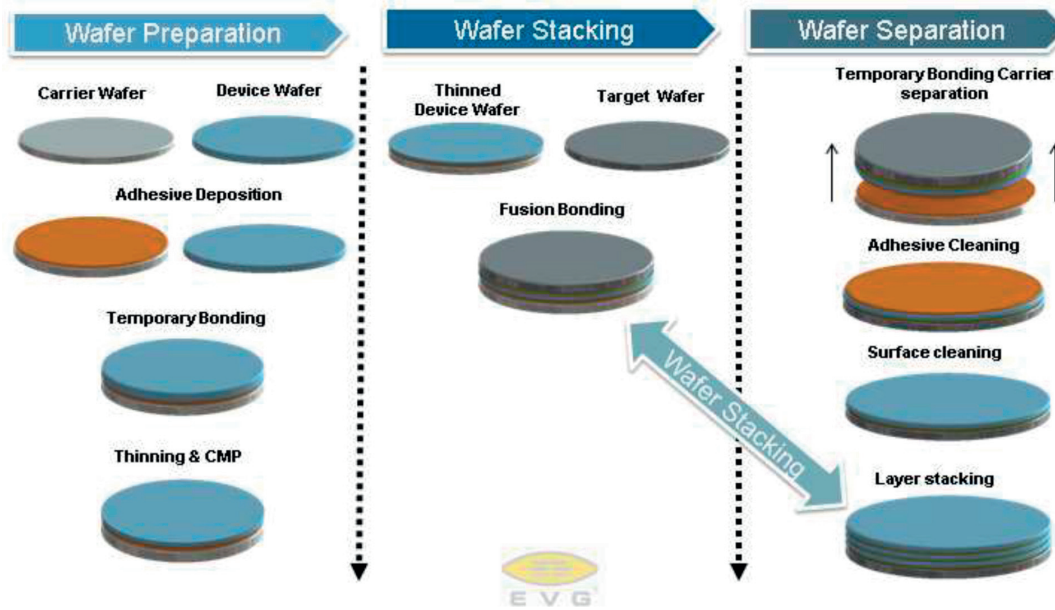
Figure 1.6 – Process flow for thin wafers stacking [59].

The silicon wafer to be thinned was first bonded using a glue (deposited by spin coating) to a carrier wafer. Then, a first rough step of grinding and a subsequent CMP (Chemical Mechanical Polishing) step were preformed to thin down the wafer to a thickness of about 10 μm. After this process, the thinned wafer (still bonded to the carrier wafer) was bonded to a full thickness (775 μm) target wafer, after a plasma activation of the surface with N$_2$. After annealing, performed at 250°C for 2 hours, the carrier wafer was separated from the bonded wafers.

1.3.4 CMOS-compatible SAB for pixel detectors fabrication

The two works from Flötgen et al. and Burggraf et al. show that a silicon conductive covalent bonding at CMOS-compatible annealing temperatures is possible. This would allow to have a monolithic-like silicon bulk starting from different substrates. Moreover, given that thin wafers stacking for CMOS integration has been demonstrated, this would also enable the development of monolithic pixel detectors, by starting from two different substrates, one with CMOS circuitry fabricated on low resistivity silicon substrate, and one with high resistivity

silicon for the sensor part of the detector, following a process similar to the one proposed by Burggraf et al. [59], with the thinning of the CMOS wafer, to eliminate the low resistivity silicon under the collection well, that would reduce the depth of the depleted silicon (see section 1.2.2) and then the bonding to the high resistivity wafer, as shown in figure 1.7, to obtain a monolithic detector with the properties of an hybrid detector (low resistivity silicon for the reaad-out and high resistivity silicon for the sensor).
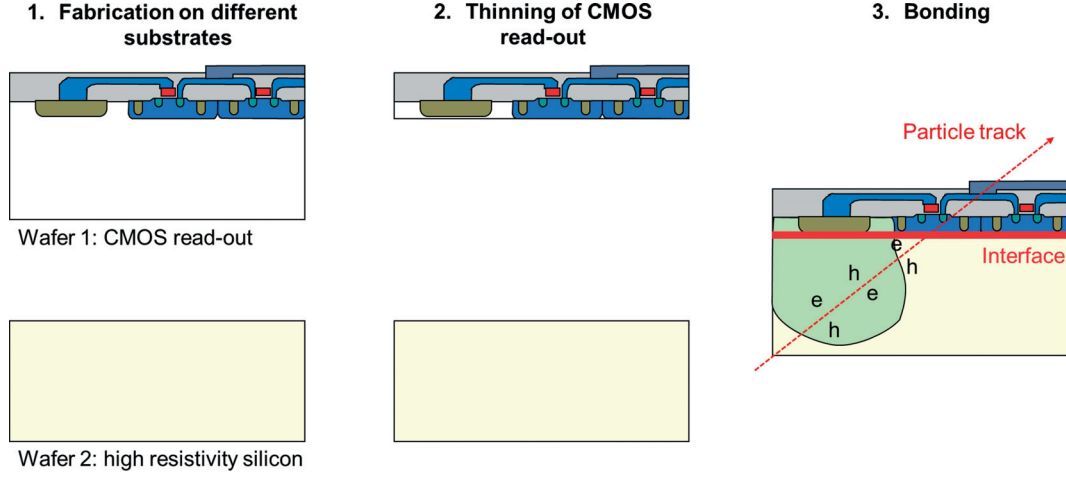
Figure 1.7 – Fabrication of monolithic pixel detector by CMOS-compatible SAB. The two components of the detector (CMOS read-out and sensor) are separately fabricated. The CMOS wafer is thinned to eliminate the low resistivity silicon, and bonded to the high resistivity sensor, to obtain a hybrid-like monolithic detector.

Since the charge generated by the radiation would need to pass through the bonding interface, its electrical properties are a key factor for the development of this process. Their characterization can be performed using the TCT.

1.4 Transient Current Technique

TCT is a technique generally used for the characterization of silicon radiation detectors. It can be used for the measurement of effective doping concentration in silicon, for the evaluation of radiation damage [60], the analysis of charge collection, drift velocity and electric field [61], over the entire volume of the detector [62]. TCT consists in the injection of charges inside the detector and in the analysis of a resulting transient current pulse. It is divided into two categories: surface illumination TCT and edge illumination TCT.

1.4.1 Surface illumination TCT

One way to perform charge injection for TCT measurements is to illuminate the surface of a semiconductor radiation detector with alpha particles. Quaranta et al. performed a transient signal analysis with alpha particles in 1965 inside a solid state radiation detector. Its working principle is based on the charge collection thanks to an electric field inside the semiconductor, as in silicon pixel detectors described in section 1.2.2. Thanks to this analysis, the charge

collection time and information about the angle of incidence of the particle on the detector surface were analyzed [63]. A study of the current pulse shape to extract the electric field profile of a surface barrier detector was performed by Cohen et al. in 1967 [64]. Other authors measured alpha particles TCT on semiconductor materials different from silicon such as cadmium telluride [65] for the study of transport properties and trapping parameters. TCT was used for the characterization of radiation damage in silicon detectors by Kraner et al. [66], especially type inversion of N-type doped silicon after neutron irradiation. In this case, a reverse biased diode was subjected to alpha particles irradiation, from a ^{244}Cm source, with an energy at the surface of 5.5 MeV, that reached a depth in the silicon bulk of 20 μm. The drifting charges generated in this thickness caused a transient current related to the electric field through the equation (1.3).

$$i(t) = q\varepsilon_w v(t) \tag{1.3}$$

Where q is the drifting charge, $i(t)$ is the generated current pulse, ε_w is the weighting field, that in this case is equal to $1/W$, and $v(t)$ is the velocity of charges, related to the electric field value at their position through equation (1.4).

$$v(t) = \mu\varepsilon(x(t)) \tag{1.4}$$

Where μ is the charges drift mobility, ε is the electric field and $x(t)$ is the position of injected charges at time t. Therefore, the field was probed by charges for the entire depth of the depletion region [66]. In figure 1.8 the principle of TCT is shown, where the detector is represented as a simple PiN diode. The type of charge carriers that are drifted along the detector changes according to the side that is illuminated. Indeed, if charge injection occurs on the side where positive sign of voltage is applied, electrons will be immediately collected by the electrode, holes will drift along the detector thickness, and the TCT signal will be generated by them. On the other hand, electrons will drift if injection occurs at the side where negative voltage is applied. Eremin et al. described a method for the analysis of TCT signal to study radiation damage from neutrons [60]. In this case, charge injection was obtained by applying a laser pulse (with an absorption length smaller than 30 μm) on the surface of the detector. The TCT signal was analyzed to extract the effective doping concentration in silicon bulk with 4 different methods:

- Analysis of the decay time constant of the current pulse, that is related to the electric field and therefore to the effective doping concentration with the relation in equation (1.5).

$$\tau = \frac{d}{\mu}\sqrt{\frac{\epsilon_0\epsilon_{Si}}{2eN_{eff}}}\frac{1}{\sqrt{V}} \tag{1.5}$$

  Where τ is the decay time and N_{eff} is the effective doping concentration.

- Determination of the full depletion voltage V_{fd} (by looking at the applied voltage at which appearance of a step in the pulse decay occurs), and then evaluation of N_{eff}
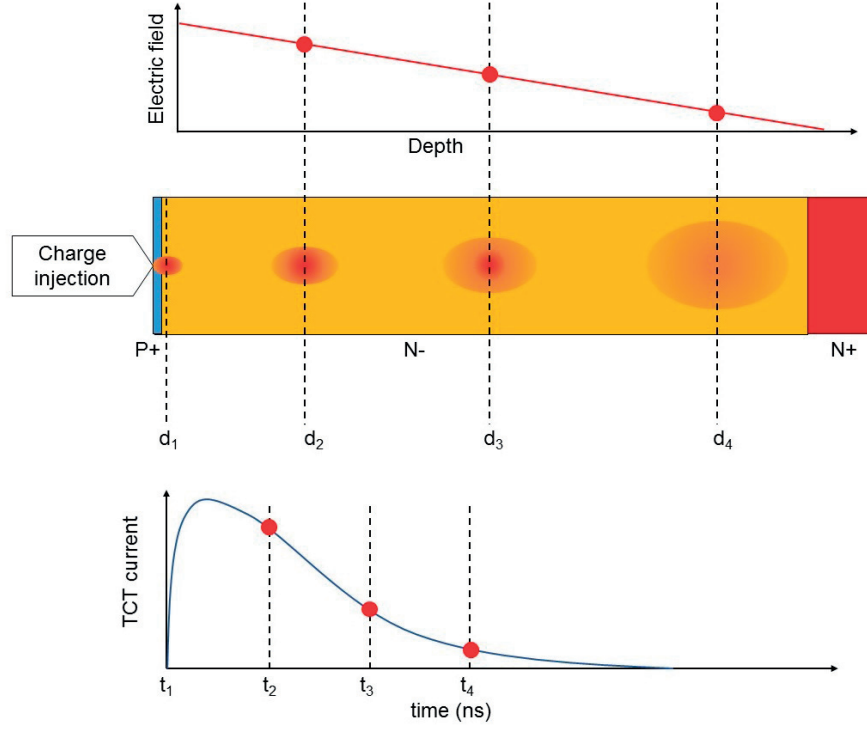
Figure 1.8 – Working principle of TCT. The silicon detector is presented as a PiN junction, in reverse bias configuration. Charges are injected on one side of the junction, and drifted along the thickness of the detector by the electric field. Points in the transient current pulse correspond to the electric field at positions reached by charges: at time t_2 charges are at position d_2, at time t_3 charges are at position d_3 and at time t_4 charges are at position d_4.

using equation (1.2), considering that at V_{fd} the depth of the depletion region is equal to the thickness of the detector d_{tot}.

- Determination of V_{fd} with the analysis of the charge variation with time when injection is performed on the high field side of the detector, and then evaluation of N_{eff} following the same method of the previous point.

- Determination of V_{fd} by analyzing the charge shapes but with illumination on the other side of the detector.

Analysis of the current pulse shape allows to study particular effects related to high radiation damage such as the double peak of electric field due to the occurring of a double junction, where trapping of charges due to radiation induced energy levels generates junctions on each side of the detector [23]. TCT was also used for purposes different from the characterization of radiation damage, such as the study of the influence of process temperature on effective doping concentration [67] and oxide traps in MOS (Metal Oxide Semiconductor) transistors [68].

15

1.4.2 Edge illumination TCT

Another method to perform TCT analysis is to generate charges by illuminating the side of the detector. To perform these measurements, an infrared laser is used, to generate electron hole pairs along the entire length of the detector since light penetration length with wavelengths used for this purpose (1060 nm) is around 912 μm in silicon [69]. The focus point of the laser is located inside the silicon bulk, as shown in figure 1.9. Therefore, electrons and holes are mainly generated around this point, and then separated by the electric field inside the detector, drifting in opposite directions. The transient current signal is generated with the same mechanism explained for surface illumination TCT. This technique is called edge TCT (eTCT) [61]. The signal is composed by two current peaks generated by charge carriers, and
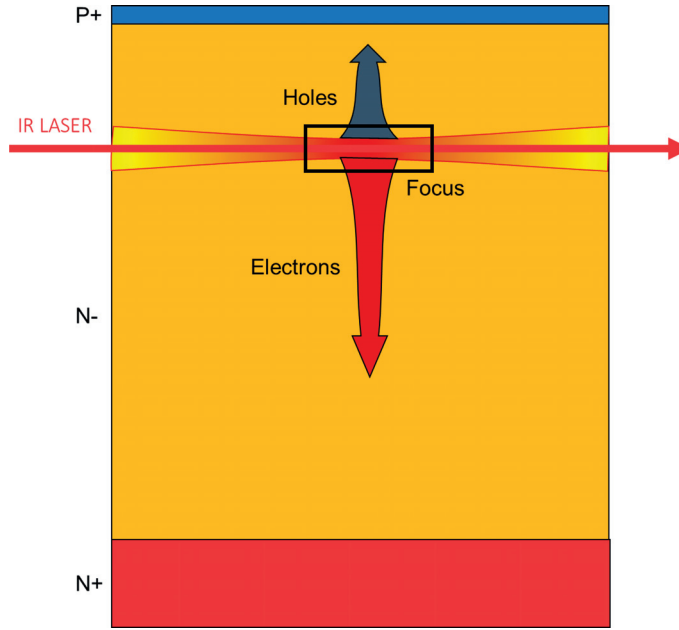
Figure 1.9 – Working principle of eTCT. In this case, charges are generated along the width of the detector, and drift in opposite directions.

can be separated since the signal from electrons is faster and higher in amplitude than the one from holes (holes mobility is 1/3 of the electrons mobility). The current signals for electrons and holes at a given position are therefore related to the electric field by equation (1.6).

$$I_{e,h}(t) = BeN_{e,h} \exp\left(-\frac{t}{\tau_{eff,e,h}}\right) v_{e,h}(t)\varepsilon_w \tag{1.6}$$

Where B is the amplification constant from the amplifier, $N_{e,h}$ is the number of generated electrons and holes, $\tau_{eff,e,h}$ is the effective trapping time for electrons and holes, $v_{e,h}(t)$ is the drift velocity for electrons and holes (that is related to the electric field by equation (1.4)). The total current $I_{tot}(t)$ is therefore the sum of the two contributions $I_{tot}(t) = I_e(t) + I_h(t)$. By considering the current amplitudes at small times, such as 300 ps (for which the drift length is around 30 μm, considering that the applied voltage causes the velocity saturation, comparable

with the laser beam diameter), it is possible to extract the effective doping concentration and electric field profiles. Moreover, by looking at the change of current peak time with the laser position in the depth direction, it is also possible to measure the drift velocity of electrons. Another information that can be extracted from the eTCT signal is the charge collection efficiency along the depth of the detector, for a given position in the width direction [61]. A more recent analysis of silicon strips detectors with eTCT was performed by Mandic et al. [70]. Charge injection for eTCT can be performed also with a collimated high energy hadron beam. In this case, electrons and holes are uniformly generated along the path of the beam, reaching the entire depleted volume. Measurements with this kind of setup were performed on a MAPS [71]. A recently developed method for charge injection in eTCT is based on the two photon absorption process. It consists in the generation of an electron hole pair by the absorption of two photons with an energy that is smaller than the direct energy gap of silicon ($\lambda \geq 1150$ nm [62]), but higher than the half of this value [72], process that was predicted by Maria Göppert-Mayer in 1931 [73]. García et al. [62] performed Two Photons Absorption eTCT (TPA-eTCT) with a femtosecond pulse laser (pulses every 243 fs, necessary to obtain absorption) with a wavelength equal to 1300 nm. Laser was focused in 1 μm (another important condition to perform). Due to the non linearity of two photons absorption, generation of electrons and holes occurred only in a volume with a length equal to 13 μm and a radius equal to 0.8 μm, allowing high resolution scans of the collected charge along the transversal cross section of an HVCMOS pixel detector cell [62]. The same method of charge injection was used also for single-event effects study in microelectronic circuitry [74].

In the previous sections, TCT has been selected as the measurement technique for the characterization of bonding interfaces from CMOS-compatible silicon direct bonding. In the next chapter, a TCAD and an analytical model will be developed to study this kind of measurements, and its results.

2 Modeling of TCT for the characterization of thin interfaces in bulk silicon

*This chapter is based on the paper **"Principle and modelling of Transient Current Technique for interface traps characterization in monolithic pixel detectors obtained by CMOS-compatible wafer bonding"**, edited by JINST, volume 11, August 2016, doi: 10.1088/1748-0221/11/08/P08016, by **J. Bronuzzi, A. Mapelli, M. Moll and J.M. Sallese**, and on the paper **"Analytical model for Transient Current Technique (TCT) signal prediction and analysis for thin interface characterization"**, edited by JINST, volume 11, December 2016, doi: 10.1088/1748-0221/11/12/C12080, by **J. Bronuzzi, A. Mapelli and J.M. Sallese**. Both the papers are original works performed by me, with the supervision of the other authors.*

In this chapter, TCT will be investigated through TCAD (using the Sentaurus TCAD software package by Synopsys [75]) and analytical modeling to demonstrate the possibility of traps detection in thin layers inside diodes, such as the ones obtained by CMOS-compatible SAB process similar to the one performed by Flötgen et al., where the interface is 3 nm thick [58]. TCAD simulations allow to predict the behavior of TCT signals, as shown in figure 2.1, where measurements of a non-irradiated diode are compared with simulations.
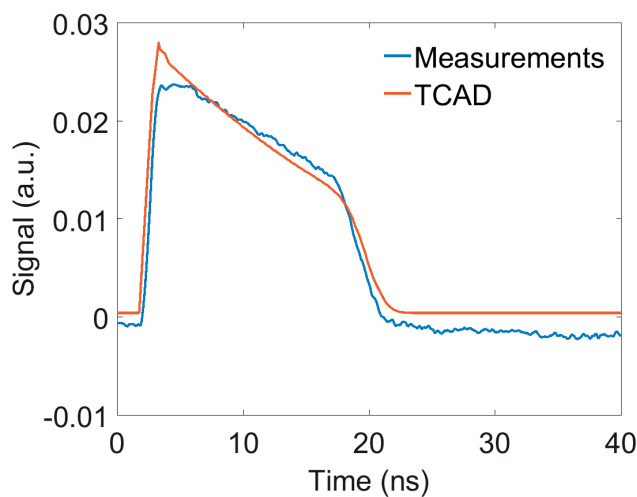
Figure 2.1 – Example of TCAD modeling of TCT signal, where the two curves, from measurements and TCAD simualtions, are of the same shape.

2.1   Assessment of TCT applied to thin interfaces characterization

2.1.1   Test structure, modeling of bonding interface

The simulated diode structure is shown in figure 2.2. For didactic purposes a PiN structure with a low doped N-type bulk has been chosen. The bonding interface is located inside the diode at the depth of 50 μm. As for the bulk characterization, the diode is reverse biased so that the low-doped silicon layer becomes depleted and carriers injection is performed by illuminating the P-doped side of the diode with a laser pulse in the ps range. Electrons that are generated inside the space charge region of the diode (near the surface) will be transported by the electric field towards the N+ contact. Holes moving in the opposite direction will be collected instantaneously. As predicted by the Ramo's theorem (see section 1.4.1), the current transient signal will be controlled by the motion of electrons in the depleted region. This is a displacement current, i.e. charges generate a current during their displacement even though they are not yet collected by the electrodes. In this example, the bonding interface
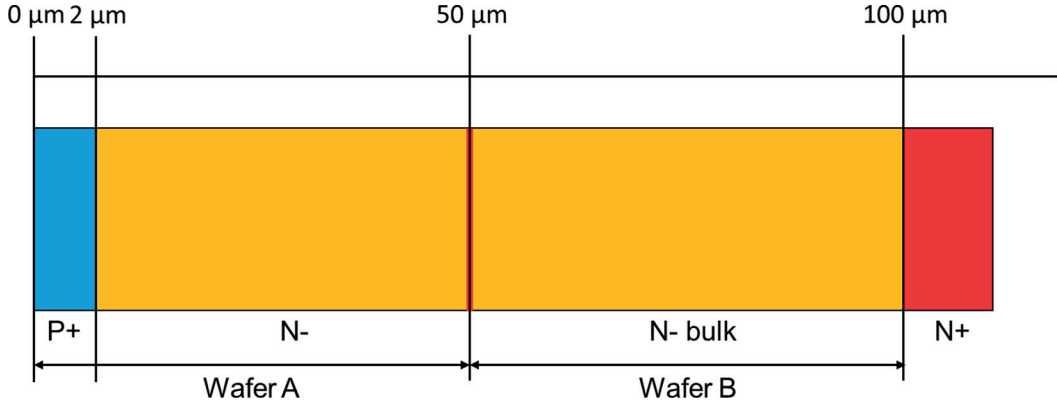
Figure 2.2 – Test diode structure. Doping of the P+ region is 2×10^{16} cm^{-3}. Doping of the N-region is 10^{12} cm^{-3}.

(red line inside the diode) is located 48 μm away from the PiN junction (it is generated by low temperature bonding between the wafer A, that hosts the diode, and the wafer B). Following the characterization done by Flötgen et al. [58], at the bonding interface an amorphous silicon layer of 3 nm thickness is expected, without evidence for an oxide layer. In this case, it will be modeled as a 3 nm thick silicon layer with a traps concentration in line with data reported for a-Si. According to Fahrner et al. [76], trap energies are essentially distributed in the mid-gap of the amorphous silicon. Therefore, the same energy range will be mainly considered, which is also what is reported by other authors [23]. In addition, the concentration of traps inside the amorphous layer will be set to 10^{16} cm^{-3} with cross sections of 10^{-14} cm^2, identical for electrons and holes. These values have been considered based on previous works on traps modelling for radiation damaged silicon devices [77]. In literature, traps cross sections range from 10^{-14} cm^2 and 10^{-16} cm^2 [23] but no significant differences have been observed for the induced space charge in TCAD simulations using equal cross sections for electrons and holes equal to 10^{-15} cm^2.

2.1.2 TCAD simulations of TCT on bonded devices

TCAD simulations of transient currents with picosecond light pulses are first run to estimate the relevance of the technique for interface traps characterization. To this purpose, the dependence of TCT on physical parameters such as the nature of the traps, their concentration and energy level is analyzed. Typical values for TCT parameters are listed in table 2.1. TCAD

Parameter name	Value
Temperature	253 K
Light wavelength	680 nm
Penetration depth (depth at which intensity is 13% of the surface value)	9.23 μm
Light intensity	0.06 W/cm^2
Light pulse time width (Gaussian pulse)	50 ps

Table 2.1 – TCT parameters used for simulations.

simulation results with these parameters are shown in figure 2.3. The TCT response subsequent to a light excitation is plotted for a mid-gap acceptor trap $E_t - E_v = 0.55$ eV (where E_v is the valence band energy level) with a concentration of 3×10^9 cm^{-2} (that is the equivalent concentration of traps per unit surface inside the thin layer, given by computing the traps volume concentration times the thickness of the traps layer). In addition, since the TCT signal is also sensitive to the reverse voltage on the PN junction, this variable was also modified. For a low reverse bias, the current decreases monotonically with time without showing any particular feature. Conversely, when increasing the reverse voltage, a non-monotonic behavior is observed, which finally turns into a clearly visible peak. This is the signature of an abrupt change of the free carrier velocity inside the depletion region, indicating that the electric field is affected by the space charge in the interface layer. Such a dependence will be explained in more details in the section dealing with the analytical model, but it is possible to safely assert that this supports that the TCT is able to reveal the existence of an anomalous charge density in a very localized region, a premise which was not anticipated before. Increasing further the reverse voltage moves the peak towards shorter times, which is consistent since the time carriers will spend to reach the counter electrode decreases while increasing their velocity. However, there is an optimum to get the highest peak-to-valley signal in the double peak shape. For instance, when the voltage goes higher than 4 V, this double peak starts to be less visible (see for an applied bias of 6 V in figure 2.3).

The influence of the main trap parameters on the TCT signal is now analyzed in order to estimate the limits of this technique. These are the concentration and the energy level of traps. Changing the traps concentration while keeping the bias voltage to 4 V (close to the optimum value for the present case) and the energy level of the acceptor traps to $E_v + 0.55$ eV, the TCT shows a double peak for concentrations higher than 3×10^9 cm^{-2} (see figure 2.4). However, it is possible to expect that when the trap density is below 3×10^9 cm^{-2}, interface traps characterization might be hardly accessible by TCT. Interestingly such a concentration is in line with typical densities reported by Fahrner et al. [76] in amorphous silicon layers. Concerning the nature of traps, i.e. donors or acceptors, simulations were run still choosing
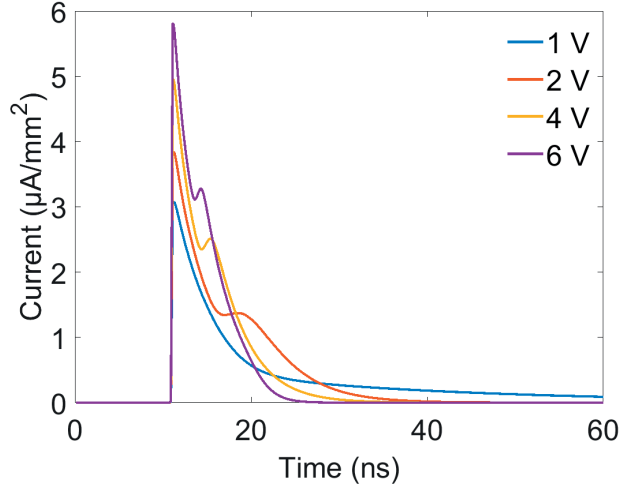
Figure 2.3 – Dependence of the TCT signal on the applied voltage. Acceptor traps level $E_v + 0.55$ eV, concentration 3×10^9 cm^{-2}.

the optimum 4 V bias together with a trap energy level and a trap concentration of $E_v + 0.55$ eV and 3×10^9 cm^{-2} respectively. Figure 2.5 reveals that the presence of charged donors only does not give rise to a double current peak and thus cannot give a precise signature (even if the shape is different from the case without traps). This suggests that in the case of low doped N-type silicon bulk, only acceptor traps can be clearly identified through the double peaked current. The presence of both acceptor and donor traps (with a concentration equal to 3×10^9 cm^{-2}) will still cause a double peak, but this is less pronounced than for acceptor traps alone. Conversely, in low doped P-type silicon, donors would be more visible. The reason for this behavior will be explained in section 2.2.4. The last parameter to be investigated is the energy level of traps. Indeed, TCT is sensitive to the electric field distorted by the presence of charged defects. Acceptors could modify substantially the TCT signal because these are charged negatively. However, depending on the energy level, traps can have different ionization states. Figure 2.6 displays the simulated TCT signal for different traps energies (referenced with respect to the valence band) at a bias voltage of 4 V and with a concentration of 3×10^9 cm^{-2}. As expected, when the energy level is higher than mid-gap, acceptor traps do not influence the TCT shape, i.e. there is no occurrence of any double peak, the reason being that the level gets less and less occupied with electrons as being shifted towards the conduction band (see section 2.2.2). Finally, based on numerical simulations, it is possible to already conclude that the TCT technique can probably be used to estimate the density of mid-gap acceptor traps at a bonding interface of a monolithic detector provided the concentration is higher than 3×10^9 cm^{-2} in an N-type doped silicon bulk. Considering donors in the same concentration range, these are still 'transparent' (exhibit a weak signature) and can be better characterized in a P-type doped layer (with symmetric configuration with respect to what used, see section 2.2.4). An additional information can be extracted from TCT signal shape. Integrating the current over time gives the total collected charge. Comparing this parameter with ($N_t = 3 \times 10^9$ cm^{-2},
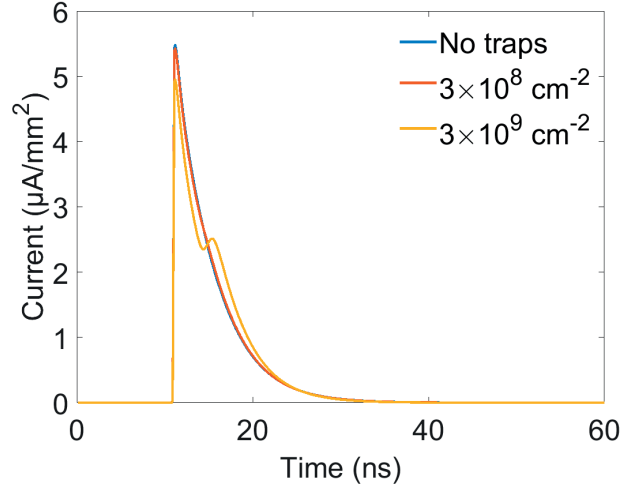
Figure 2.4 – Dependence of the TCT signal on the traps concentration inside the interface layer. Acceptor traps level $E_v + 0.55$ eV, bias voltage 4 V.
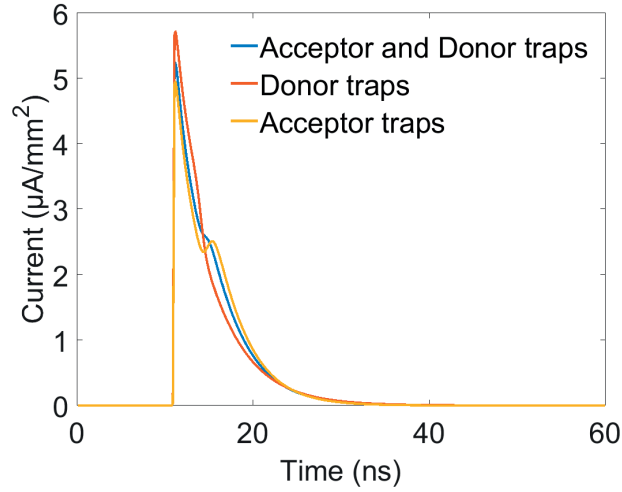
Figure 2.5 – Dependence of the TCT signal on the type of traps. Traps level $E_v + 0.55$ eV, concentration 3×10^9 cm^{-2}, bias voltage 4 V.

$E_t = E_v + 0.55$ eV) and without traps it is possible to observe that with an applied reverse bias of 4 V, the collected charge is the same and equals to 2.48×10^{-14} C. Therefore, traps present in the interface layer, in the investigated parameter range, do not cause detectable trapping of charges that travel through it as far as a high electric field sweeps then out. In the following, an analytical model for TCT characterization of embedded interface traps is proposed.
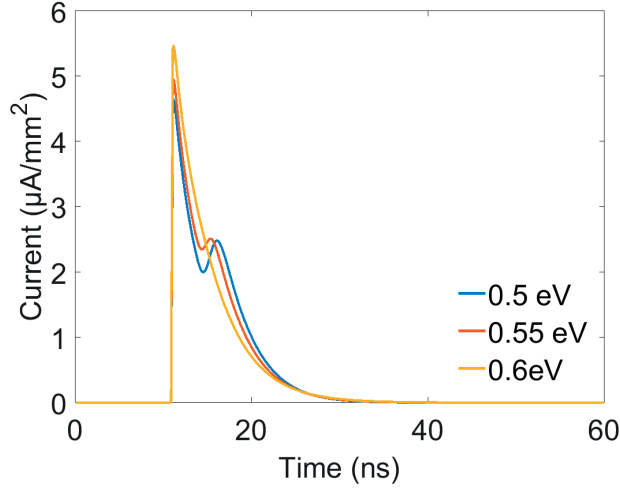
Figure 2.6 – Dependence of the TCT signal on the traps energy level. Acceptor traps, concentration 3×10^9 cm^{-2}, bias voltage 4 V.

2.2 Analytical modeling of TCT with interface traps

As already explained, the transient current signal is generated from the displacement of electric charges moving inside the space charge region following Ramo's theorem [78]. In this way, the time dependence of the current and the electric field profile are interrelated. After having validated the principle of the technique for interface characterization by means of numerical simulations, the aim of this section is to develop a full analytical model of TCT to get a detailed understanding of the physical process of it and provide a simple tool that can be used to optimize experimental conditions and estimate relevant physical parameters without being forced to perform complex TCAD simulations.

2.2.1 Modeling of the electric field profile

In a first step, the electric field across the whole structure is calculated. This is obtained by solving the Poisson equation inside and across the different layers of the diode shown in figure 2.2, using the same structure as in section 2.1. To avoid excessive complexity, the depletion approximation is assumed. This restriction is well supported by TCAD numerical simulations. Traps are considered to be located at the interface x_t in figure 2.7. Two different cases have to be analyzed whether the space charge region generated by the junction under reverse bias includes or not the interface layer (figures 2.7a and 2.7b). The different depletion regions where the Poisson equation has to be solved are identified by the black lines in figure 2.7. The depletion regions edges in the P and N type semiconductor are labeled x_p and x_n respectively, W_t is the total depletion width induced by the traps at thermal equilibrium, x_t is the position of the trap layer, x_L is the front side contact of the diode and x_R is the back side contact of the diode. The bias voltage is defined as $V = V_{x_R} - V_{-x_L}$ (where V_{-x_L} is the voltage applied to the P+ side and V_{x_R} is the voltage applied to the N+ side). The boundary conditions used to calculate the electric field in the whole structure are listed hereafter:
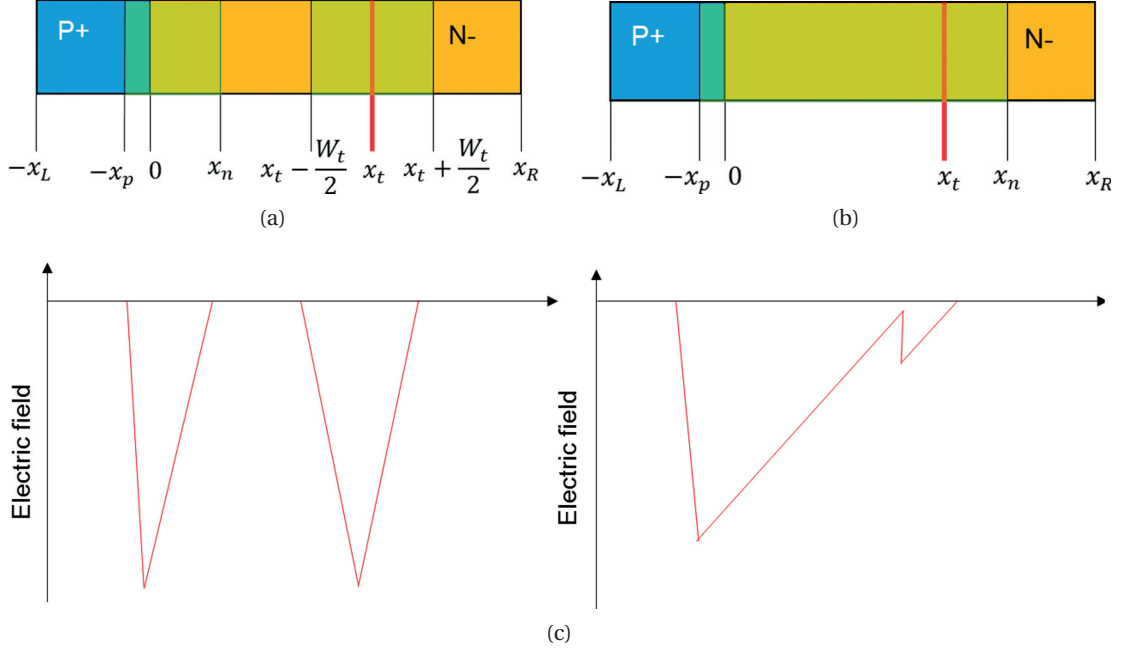
Figure 2.7 – Two possible configurations of the space charge region shape (green area) inside the diode: (a) the case where it does not reach the interface layer located at x_t, and (b) the case where it includes the layer. (c) The electric field profile is also sketched.

- At $-x_L$, the electrostatic potential is equal to $-V$ and the electric field is set to 0.

- The electrostatic potential $\Psi(x)$ must satisfy the semiconductor statistics:

$$V_{bi} = \frac{k_b T}{e} ln\left(\frac{N_A N_D}{n_i^2}\right) = \frac{\Psi(x_n) - \Psi(-x_p)}{e} \tag{2.1}$$

  where V_{bi} is the built in potential, k_b is the Boltzmann constant, T is the temperature, N_A is the concentration of acceptors, N_D is the concentration of donors, n_i is the intrinsic carriers concentration, $\Psi(x)$ is the potential.

- In the case of two separated space charge regions (Figure 2.7a), the electrostatic potential is assumed to be symmetric to the interface layer: $\Psi(x_t - W_t/2) = \Psi(x_t + W_t/2)$.

- The charge density generated by ionized traps inside the interface layer introduces a discontinuity of the electric field:

$$\varepsilon(x_t^-) - \varepsilon(x_t^+) = \frac{(N_D + N_t)e}{\epsilon_{Si}} d_t \tag{2.2}$$

  where $\varepsilon(x_t^-)$ and $\varepsilon(x_t^+)$ are respectively the electric fields evaluated at the left and at the right of the traps layer, N_t is the volume concentration of charged traps, d_t is the thickness of the traps layer.

In addition, charge conservation, continuity of the displacement vector (except at the trap interface) and electrostatic potentials are implicitly satisfied.

The derivation of equations for electric field and potential is considered for the two cases: double space charge region and single space charge region (respectively shown in figure 2.7a and 2.7b). The diode is divided in different regions, and for each region, positions referred to figure 2.7 and equations are listed.

Double charge regions case

- **Region P+,n**, position $-x_L < x < -x_p$: in this region, silicon is not depleted, and therefore the equations will be:

  - $\varepsilon_{P+,\,n}(x) = 0$;
  - $\Psi_{P+,\,n}(x) = -V$.

- **Region P+**, position $-x_p < x < 0$: in this region, silicon is depleted, and therefore, by solving the Poisson equations:

  - $\varepsilon_{P+}(x) = -\frac{N_A e}{\epsilon}(x + x_p)$;
  - $\Psi_{P+}(x) = \frac{N_A e}{2\epsilon}\left(x + x_p\right)^2 - V$.

- **Region 1**, position $0 < x < x_n$: also in this region silicon is depleted, and therefore:

  - $\varepsilon_1(x) = \frac{N_D e}{\epsilon}x - \frac{N_A e}{\epsilon}x_p$;
  - $\Psi_1(x) = -\frac{N_D e}{2\epsilon}x^2 + \frac{N_A e}{\epsilon}x_p x + \frac{N_A e}{2\epsilon}x_p^2 - V$.

- **Region 2**, position $x_n < x < x_t - \frac{W_t}{2}$: Si is not depleted:

  - $\varepsilon_2(x) = 0$;
  - $\Psi_2(x) = -\frac{N_D e}{2\epsilon}x_n^2 + \frac{N_A e}{\epsilon}x_p x_n + \frac{N_A e}{2\epsilon}x_p^2 - V$.

- **Region t,1**, position $x_t - \frac{W_t}{2} < x < x_t$: Si is depleted, in this case by the charge generated by traps:

  - $\varepsilon_{t,1}(x) = \frac{N_D e}{\epsilon}\left(x - x_t + \frac{W_t}{2}\right)$;
  - $\Psi_{t,1}(x) = -\frac{N_D e}{2\epsilon}\left[x^2 + x_n^2 + \left(x_t - \frac{W_t}{2}\right)^2\right] + \frac{N_D e}{\epsilon}\left(x_t - \frac{W_t}{2}\right)x + \frac{N_A e}{\epsilon}x_p x_n + \frac{N_A e}{2\epsilon}x_p^2 - V$.

- **Region t,2**, position $x_t < x < x_t + \frac{W_t}{2}$:

  - $\varepsilon_{t,2}(x) = \frac{N_D e}{\epsilon}\left(x + \frac{W_t}{2} - x_t\right) - \frac{(N_D + N_t)d_t}{\epsilon}e$;
  - $\Psi_{t,2}(x) = -\frac{N_D e}{2\epsilon}\left(x + \frac{W_t}{2} - x_t\right)^2 + \frac{(N_D + N_t)d_t}{\epsilon}e(x - x_t) + \frac{N_D e}{2\epsilon}\left(\frac{W_t}{2}\right)^2 - \frac{N_D e}{2\epsilon}\left[x_t^2 + x_n^2 + \left(x_t - \frac{W_t}{2}\right)^2\right] +$
    $\frac{N_D e}{\epsilon}\left(x_t - \frac{W_t}{2}\right)x_t + \frac{N_A e}{\epsilon}x_p x_n + \frac{N_A e}{2\epsilon}x_p^2 - V$.

- **Region N-**, position $x_t + \frac{W_t}{2} < x < x_R$: Silicon is not depleted:

- $\varepsilon_{N-}(x) = 0$;
- $\Psi_{N-}(x) = -\frac{N_D e}{2\epsilon} W_t^2 + \frac{(N_D+N_t)d_t}{\epsilon} e \frac{W_t}{2} + \frac{N_D e}{2\epsilon}\left(\frac{W_t}{2}\right)^2 - \frac{N_D e}{2\epsilon}\left[x_t^2 + x_n^2 + \left(x_t - \frac{W_t}{2}\right)^2\right] + \frac{N_D e}{\epsilon}\left(x_t - \frac{W_t}{2}\right)x_t + \frac{N_A e}{\epsilon}x_p x_n + \frac{N_A e}{2\epsilon}x_p^2 - V$.

To complete the set of equations, it is needed to determine the values of x_p, x_n and W_t.

$$x_p = \left(\frac{N_D}{N_D + N_A}\right) W \tag{2.3}$$

$$x_n = \left(\frac{N_A}{N_D + N_A}\right) W \tag{2.4}$$

$$W = \sqrt{\frac{2\epsilon}{e}\left(\frac{N_A + N_D}{N_A N_D}\right)(V_{bi} + V - 2k_b T)} \tag{2.5}$$

$$W_t = \frac{(N_D + N_t)\, d_t}{N_D} \tag{2.6}$$

Single space charge region case

- **Region P+,n**, position $-x_L < x < -x_p$: in this region, silicon is not depleted, and therefore the equations will be:

  - $\varepsilon_{P+,\,n}(x) = 0$;
  - $\Psi_{P+,\,n}(x) = -V$.

- **Region P+**, position $-x_p < x < 0$: in this region, silicon is depleted, and therefore, by solving the Poisson equations:

  - $\varepsilon_{P+}(x) = -\frac{N_A e}{\epsilon}(x + x_p)$;
  - $\Psi_{P+}(x) = \frac{N_A e}{2\epsilon}\left(x + x_p\right)^2 - V$.

- **Region 1**, position $0 < x < x_t$: also in this region silicon is depleted, and therefore:

  - $\varepsilon_1(x) = \frac{N_D e}{\epsilon}x - \frac{N_A e}{\epsilon}x_p$;
  - $\Psi_1(x) = -\frac{N_D e}{2\epsilon}x^2 + \frac{N_A e}{\epsilon}x_p x + \frac{N_A e}{2\epsilon}x_p^2 - V$.

- **Region 2**, position $x_t < x < x_n$: silicon is not depleted:

  - $\varepsilon_2(x) = \frac{N_D e}{\epsilon}x - \frac{N_A e}{\epsilon}x_p - \frac{(N_D+N_t)e}{\epsilon}d_t$;
  - $\Psi_2(x) = -\frac{N_D e}{2\epsilon}x^2 + \left(\frac{N_A e}{\epsilon}x_p + \frac{(N_D+N_t)e}{\epsilon}d_t\right)x + \left\{\frac{(N_D+N_t)e}{\epsilon}d_t x_t + \frac{N_A e}{2\epsilon}x_p^2 - V\right\}$.

- **Region N-**, position $x_n < x < x_R$: silicon is not depleted:

- $\varepsilon_{N-}(x) = 0$;
- $\Psi_{N-}(x) = -\frac{N_D e}{2\epsilon} x_n^2 + \left(\frac{N_A e}{\epsilon} x_p + \frac{(N_D+N_t)e}{\epsilon} d_t\right) x_n + \left\{\frac{(N_D+N_t)e}{\epsilon} d_t x_t + \frac{N_A e}{2\epsilon} x_p^2 - V\right\}$.

To complete the set of equations, it is needed to determine the values of x_p and x_n.

$$x_n = \frac{N_A}{N_D} x_p + \frac{(N_D + N_t)}{N_D} d_t \tag{2.7}$$

$$x_p = \frac{-\left(\frac{e}{\epsilon}\frac{N_A(N_D+N_t)}{N_D} d_t\right) + \sqrt{\left(\frac{e}{\epsilon}\frac{N_A(N_D+N_t)}{N_D} d_t\right)^2 - 4\frac{eN_A}{2\epsilon}\left(\frac{N_A}{N_D}+1\right)\left[\frac{(N_D+N_t)e}{\epsilon} d_t\left(\frac{1}{2}\frac{N_D+N_t}{N_D} d_t - x_t\right) - V_{bi} - V\right]}}{\frac{eN_A}{\epsilon}\left(\frac{N_A}{N_D}+1\right)} \tag{2.8}$$

From equations (A.5) and (A.6), knowing the full depletion voltage V_{fd} and the length of the bulk x_R, and that at full depletion $x_n = x_R$, it is possible to extract the charged traps volume density N_t. The set of equations A.7, A.8, A.9 and A.10 shows the relations that link N_t to V_{fd}.

$$a_{N_t} = \left(\frac{eN_D}{\epsilon}\right)^2 \left(1 + \frac{N_A}{N_D}\right) \tag{2.9}$$

$$b_{N_t} = \left(\frac{eN_D}{\epsilon}\right)^2 \left(\frac{N_A}{N_D} + 1\right) x_R + \frac{e^2 N_A}{\epsilon^2} x_t (N_A + N_D) \tag{2.10}$$

$$c_{N_t} = \left(x_R \frac{eN_D}{\epsilon}\left(\frac{N_A}{N_D}+1\right)\right)^2 - 2\left(V_{bi} + V_{fd}\right)\frac{eN_A}{\epsilon}\left(\frac{N_A}{N_D}+1\right) \tag{2.11}$$

$$N_t = N_D \left(\frac{b_{N_t} - \sqrt{b_{N_t}^2 - a_{N_t} c_{N_t}}}{d_t a_{N_t}} - 1\right) \cong N_D \frac{b_{N_t} - \sqrt{b_{N_t}^2 - a_{N_t} c_{N_t}}}{d_t a_{N_t}} \tag{2.12}$$

Figure 2.8 shows some cases of electric fields calculated with the analytical model and TCAD simulations for different reverse bias voltages. It is possible to see that the overall profiles obtained by analytical calculations match fairly well those obtained by TCAD simulations.

2.2.2 Modeling of traps occupancy

To evaluate the electric field, the charge generated by the traps must be calculated, but their state depends on the relative position of the energy level with respect to the Fermi level. Basically, traps can be acceptors (positively charged when they capture holes) or donors (negatively charged when they capture electrons) [79]. The general analysis relies on capture and emission rates but this can be quite complex to handle in the dynamic analysis of the
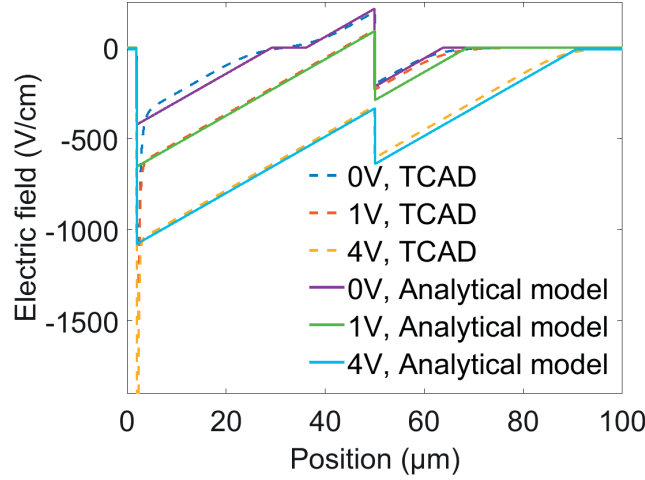
Figure 2.8 – Electric field comparison between TCAD simulations and the analytical model. Acceptor traps level $E_v + 0.55$ eV, concentration 3×10^9 cm^{-2}.

structure considered. However, depending on the energy configuration, two asymptotic expressions can be used instead. One applies for traps at equilibrium and the other for traps out of equilibrium, keeping in mind that the status depends on how the diode is operating.

Traps at equilibrium

In the case of two separated space charge regions as shown on figure 2.7a, traps are not subjected to the potential applied to the junction as they are somehow isolated from the applied voltages by adjacent neutral regions. This situation happens when the voltage remains relatively low so that only the depletion region generated by traps surrounds the layer at x_t. Since traps are in thermal equilibrium, it is possible to use the common relationship for acceptor and donor traps [79] given by:

$$N_{at,e} = N_{at,0} \left(\frac{1}{1 + g \exp\left(\frac{E_{at} - E_F}{k_b T} \right)} \right) \qquad N_{dt,e} = N_{dt,0} \left(\frac{1}{1 + g \exp\left(\frac{-E_{dt} + E_F}{k_b T} \right)} \right) \tag{2.13}$$

where $N_{at,0}$ and $N_{dt,0}$ are the acceptor and donor traps volume concentrations, $N_{at,e}$ and $N_{dt,e}$ are the charged acceptor and donor traps volume concentrations at equilibrium, g is the degeneracy factor (assumed to be equal 1), E_{at} and E_{dt} are the acceptor and donor traps energy levels, E_F is the Fermi level. Importantly, once traps are ionized, they modify the potential locally and bend the bands as shown on figure 2.9. The trap energy level must then include the energy shift self consistently. This is obtained by computing the difference $\Psi_{t,1}(x_t) - \Psi_{t,1}(x_t - W_{t/2})$ with W_t obtained from equation (2.6). Adding the bending of the electrostatic potential at the position of the traps x_t to the traps energy level gives finally:

$$E_{at} = E_{at,0} + \frac{eN_D}{8\epsilon_{Si}} \left(\frac{N_D + N_{t,e}}{N_D} d_t \right)^2 \qquad E_{dt} = E_{dt,0} + \frac{eN_D}{8\epsilon_{Si}} \left(\frac{N_D + N_{t,e}}{N_D} d_t \right)^2 \tag{2.14}$$

29

where $E_{at,0}$ and $E_{dt,0}$ are the acceptor and donor traps energy levels referred to valence band. To conclude, equation (2.15) allows to compute the total volume concentration of charge at equilibrium.

$$N_{t,e} = N_{at,e} - N_{dt,e} \tag{2.15}$$
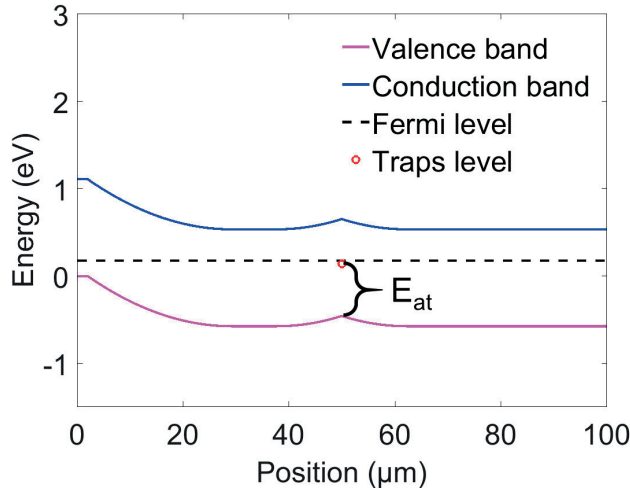
Figure 2.9 – Energy band diagram at equilibrium. The band bending affects the traps energy levels reference with respect to the Fermi Level. Acceptor traps level $E_v + 0.6$ eV, concentration 3×10^9 cm^{-2}.

Traps out of equilibrium

When the reverse bias potential increases so that the depletion regions limits x_n and $x_t - W_t/2$ start to overlap, a single depletion region is created such as shown in figure 2.7b, meaning that traps are out of equilibrium. In this case, instead of relations (2.13), one should consider the competition between emission and capture processes to get the ratio between ionized and neutral states, as explained in [80]. Unfortunately, these expressions are not tractable with the analytical model at aim in this work. Then, in order to simplify the analysis, two cases will be identified. The first case assumes that the depletion region x_n goes well beyond $x_t + W_t/2$, which happens for large reverse voltages. Then, it is possible to use the out of equilibrium equations for the traps charge density as given for example from Lutz et. al. [81]. In this work, the fraction of charged traps is evaluated assuming a fully depleted semiconductor, which gives:

$$N_{at,oe} = N_{at,0} \left(\frac{1}{1 + \frac{c_{n,a}}{c_{p,a}} \exp\left(2\frac{E_{at,0}-E_i}{k_b T}\right)} \right) \quad N_{dt,oe} = N_{dt,0} \left(\frac{1}{1 + \frac{c_{p,d}}{c_{n,d}} \exp\left(-2\frac{E_{dt,0}-E_i}{k_b T}\right)} \right) \tag{2.16}$$

where $N_{at,oe}$ and $N_{dt,oe}$ are the charged acceptor and donor traps volume concentrations out of equilibrium, E_i is the intrinsic Fermi level, $c_{n,a}$ and $c_{p,a}$ are the electrons and holes capture coefficient for acceptors traps, $c_{n,d}$ and $c_{p,d}$ are the electrons and holes capture coefficient for donors traps. In order to match the occupied fraction of the defects between the TCAD and the analytical model equation (2.16) was used in the following way. It is assumed that the intrinsic level E_i is $E_v + 0.55$ eV. Then the ratio $c_{n,i}/c_{p,i}$ was determined to be 0.52 to match TCAD results. For all further analytical calculations with different defect energy levels the ratio was fixed to this value. The total volume concentration of charged traps out of equilibrium is then $N_{t,oe} = N_{at,oe} - N_{dt,oe}$.

Traps at semi-equilibrium

The third case is the semi-equilibrium condition. This happens for voltages where the depletion regions are still competing against one another in a sense that satisfies the following inequality:

$$x_t - \frac{W_t}{2} < x_n < x_t + \frac{W_t}{2} \tag{2.17}$$

Considering equations (2.4), (2.5) and (2.6) and substituting them in (2.17), the corresponding voltage range for the semi-equilibrium condition can be derived:

$$\frac{e}{2\epsilon}\left(\frac{N_D+N_A}{N_A N_D}\right)\left(N_D x_t - \frac{(N_D+N_{t,e})\,d_t}{2}\right)^2 + \frac{2k_b T}{e} - V_{bi} < -V <$$
$$\frac{e}{2\epsilon}\left(\frac{N_D+N_A}{N_A N_D}\right)\left(N_D x_t + \frac{(N_D+N_{t,e})\,d_t}{2}\right)^2 + \frac{2k_b T}{e} - V_{bi} \tag{2.18}$$

In this case, there is a competition between equilibrium and out of equilibrium models. To avoid introducing excessive complexity, an empirical definition of a weighting parameter ω is introduced, to give an estimation of the ratio between the equilibrium and the out of equilibrium areas of the traps depletion region:

$$\omega = \frac{1}{W_t}\left(x_n - \left(x_t - \frac{W_t}{2}\right)\right) \tag{2.19}$$

Relation (2.19) represents the fraction of the depletion region generated by traps calculated when equilibrium is satisfied (region between $\left(x_t - \frac{W_t}{2}\right)$ and $\left(x_t + \frac{W_t}{2}\right)$ in figure 2.7a, with W_t given in equation (2.6)) which intersects the depletion region that is generated by the voltage applied to the junction, evaluated when there are two depletion regions (whose edge in the n-type silicon bulk is x_n, evaluated following equations (2.4) and (2.5)). Once ω is computed, the volume concentration of charged traps N_t is evaluated from equation (2.20).

$$N_t = \omega N_{t,oe} + [1 - \omega]\, N_{t,e} \tag{2.20}$$

Obviously, N_t reverts to $N_{t,oe}$ for a full out of equilibrium condition, i.e. when $x_n > x_t + \frac{W_t}{2}$. Considering different traps concentrations, energy levels and types, there is a good

matching between the charged traps concentrations obtained from the model and from TCAD simulations (see tables 2.2 and 2.3, where evaluations are done for two different applied voltages, 1 V and 4 V, and traps concentrations are considered as surface concentration, equal to $d_t N_t$). Moreover, in Figure 2.8 it is possible to observe the matching in the three different regimes, i.e. equilibrium (at 0 V), partially out of equilibrium (at 1 V) and fully out of equilibrium (at 4 V). In all these situations, the model agrees pretty well with a full numerical treatment.

Traps type	Traps energy level with respect to the valence band (eV)	Charged traps concentration from TCAD (cm⁻²)	Charged traps concentration from analytical model (cm⁻²)
Acceptor	0.5	3.0×10^9	3.0×10^9
Acceptor	0.55	2.0×10^9	2.0×10^9
Acceptor	0.6	5.8×10^7	5.8×10^7
Donor	0.55	1.0×10^9	1.0×10^9

Table 2.2 – Charged traps concentration from TCAD simulations and analytical model with a bias voltage equal to 4 V.

Traps type	Traps energy level with respect to the valence band (eV)	Charged traps concentration from TCAD (cm⁻²)	Charged traps concentration from analytical model (cm⁻²)
Acceptor	0.5	3.0×10^9	2.8×10^9
Acceptor	0.55	2.5×10^9	2.1×10^9
Acceptor	0.6	1.6×10^8	1.8×10^8
Donor	0.55	~ 0	3×10^5

Table 2.3 – Charged traps concentration from TCAD simulation and analytical model, with a bias voltage equal to 1 V.

2.2.3 Modeling of transient current

The link between the transient current and the electric field profile is provided by the Ramo's theorem which states that the current generated by a traveling charge inside a parallel plate capacitor is given by:

$$i(t) = \frac{qv}{L} \tag{2.21}$$

Where q is the charge moving at speed v, and L is the distance between the capacitor electrodes. In the case of our diode, electrodes are substituted by the edges of the space charge region. Therefore, since the electron velocity depends on the electric field following the law $v = \mu_e \varepsilon$,

for each moving electron, the related transient current will be proportional to the electric field evaluated where the electron is at time t, i.e. $r(t)$. In addition, the field mobility dependence based on the extended Canali model is introduced [82]:

$$\mu_e = \frac{\mu_{e,0}}{1 + \frac{\mu_{e,0}|\varepsilon(r)|}{v_{sat}}} \tag{2.22}$$

Where $\varepsilon(r)$ is the electric field, $\mu_{e,0}$ is the low field electron mobility (1417 cm^2/Vs for silicon), and $v_{sat} = v_{sat,0}\left(\frac{300\,\text{K}}{T}\right)^{0.87}$ is the saturation velocity ($v_{sat,0} = 1.07 \times 10^7$ cm/s). Considering that $v = \mu_e \varepsilon$, a differential equation in terms of position $r(t)$ and time can be derived:

$$\frac{dr}{dt} = \mu_e \varepsilon(r) \tag{2.23}$$

Equation (2.23) is then evaluated in each region of figures 2.7a or 2.7b using the correct expression for the electric field, and results are shown in the following paragraph.

Equations of motion of electrons

Solutions of the differential equation (2.23) are shown, for each region of the diode, in the one space charge region case (in the case with two space charge regions, it is possible to consider equations until Region 1, until time t_n, that is the time for which $r(t_n) = x_n$).

The notation $L_W(x)$ refers to the Lambert W function of x.

- **Region P+**, position $-x_p < x < 0$

$$r = -x_p + E L_W\left(\frac{1}{F}\exp\left(\frac{v_{sat}t + K_{0b}}{F}\right)\right) + K_{0,a} \tag{2.24}$$

  Where:

$$K_{0,b} = F\ln\left(-K_{0,a}\right) - K_{0,a} \tag{2.25}$$

$$K_{0,a} = -1 \tag{2.26}$$

$$F = \frac{\epsilon}{\mu_{e0}N_A e} v_{sat} \tag{2.27}$$

- **Region 1**, position $0 < x < x_t$. At time t_1, the middle of the electrons cloud will reach the position 0.

$$t_1 = \frac{x_p + E\ln\left(\frac{K_{0,a}-x_p}{K_{0,a}}\right)}{v_{sat}} \tag{2.28}$$

33

$$K_1 = \frac{N_A}{N_D}x_p + F_1\ln\left(\frac{N_A}{N_D}x_p\right) + v_{sat}t_1 \tag{2.29}$$

$$r = \frac{N_A}{N_D}x_p - F_1 L_W\left(\frac{1}{F_1}\exp\left(\frac{-v_{sat}t + K_1}{F_1}\right)\right) \tag{2.30}$$

Where

$$F_1 = \frac{v_{sat}\epsilon}{N_D q\mu_{e0}} \tag{2.31}$$

And N_D is the doping concentration of the N- region. The middle of the electrons cloud will reach the position x_n, in case of two separated depletion regions, at time t_n.

$$t_n = \frac{-x_n + \frac{N_A}{N_D}x_p + F_1\ln\left(-x_n + \frac{N_A}{N_D}x_p\right) - K_1}{-v_{sat}} \tag{2.32}$$

Since in the case of two separated depletion regions the electric fields vanishes at x_n, $t_n = +\infty$.

- **Region 2**, position $x_t < x < x_n$. At time t_2, the middle of the electrons clouds will reach the position x_n.

$$t_2 = \frac{-x_t + \frac{N_A}{N_D}x_p + F_1\ln\left(-x_t + \frac{N_A}{N_D}x_p\right) - K_1}{-v_{sat}} \tag{2.33}$$

$$K_2 = -x_t + \frac{N_A}{N_D}x_p + \frac{(N_D + N_t)}{N_D}d + F_1\ln\left(-x_t + \frac{N_A}{N_D}x_p + \frac{(N_D + N_t)}{N_D}d\right) + v_{sat}t_2 \tag{2.34}$$

$$r = \frac{N_A}{N_D}x_p + \frac{(N_D + N_t)}{N_D}d - F_1 L_W\left(\frac{1}{F_1}\exp\left(\frac{-v_{sat}t + K_2}{F_1}\right)\right) \tag{2.35}$$

The single charge picture

The TCT signal of a localized charge traveling across the structure choosing a trap energy level of $E_v + 0.5$ eV with a concentration 3×10^9 cm^{-2} and at a bias of 4 V is analyzed first and shown in figure 2.10.

The time dependence of the overall TCT signal is reasonably well reproduced between the analytical model and TCAD simulations, meaning that in essence the modeling approach and the principle behind it is correct. However, looking into the details reveals a quite different shape. This is attributed to the self diffusion of the initial bunch of carriers as time passes. Indeed, a rough estimation of the diffusion length gives about 5 µm after 10 ns (in line with
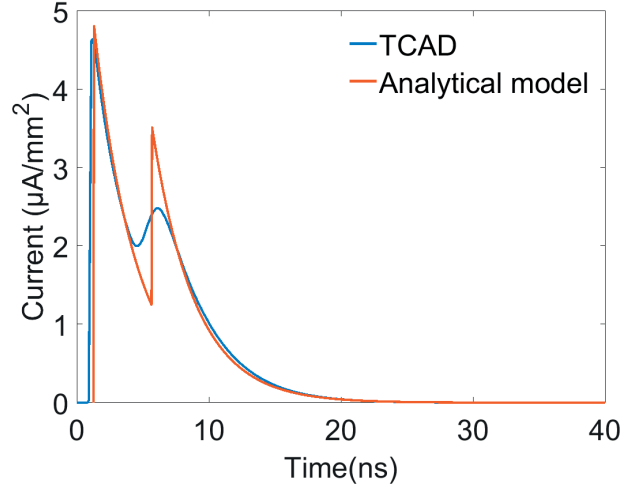
Figure 2.10 – TCT signal prediction between TCAD and analytical model simulations. Here a localized charge traveling across the structure is considered. Acceptor traps level $E_v + 0.5$ eV, concentration 3×10^9 cm^{-2}, bias voltage 4 V.

traveling times) considering an average mobility of 0.1 m^2/Vs, thus revealing that during their motion, the initial shape will extend over a non-negligible region in regard to the dimensions of the depletion region. Without entering into the details, it is possible to obtain the exact solution of the continuity equation with a linearly dependent electric field. However this requires numerical computations, and therefore an explicit analytical solution cannot be obtained.

The Gaussian approximation of the travelling carrier density

The sharp signal predicted by the model is still quite crude and cannot reproduce precisely the shape of numerical simulations. To this purpose, a diffusion process by introducing a Gaussian function whose center moves according to the mean value of the electric field is introduced:

$$n(x, t) = \frac{n_{inj}}{\sqrt{4\pi D_n t}} \exp\left(-\frac{(x - r(t))^2}{4D_n t}\right) \tag{2.36}$$

It is worth noticing that relation (2.36) still represents the solution of the continuity equation in a uniform electric field [83]. However, in our case, the electric field is non uniform and therefore relation (2.36) is merely an approximate solution. The Gaussian has the following features: the maximum equals the number of photo generated electrons n_{inj}, the center is still given by $r(t)$ that satisfies relation (2.23), and the variance changes with time following the diffusion law with D_n being the diffusion constant. The transient current density can

therefore be defined by the following equation:

$$i(t) = \Xi \int\limits_{Region}^{Depletion} n(x,t)\, v(x)\, dx = \Xi \int\limits_{Region}^{Depletion} n(x,t)\, \varepsilon(x)\, \mu_e(\varepsilon(x))\, dx \qquad (2.37)$$

Where Ξ is a scaling geometrical parameter defined to match the TCAD current density absolute value. Next, integrals needs to be solved for each region of the diode, in case of two separated space charge regions or a single space charge region, as already done to get the solutions of equation (2.23). Figure 2.11a illustrates the new TCT prediction given by the analytical model with the diffusion process included. It comes out that the approximate
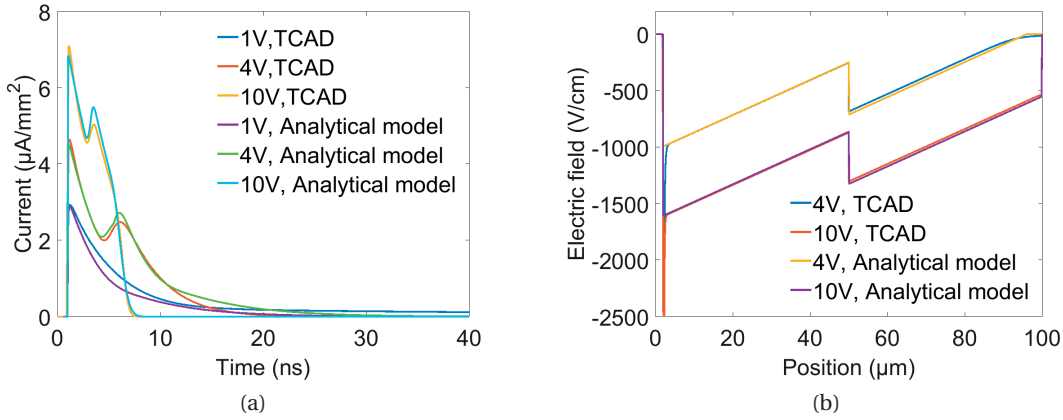
Figure 2.11 – TCAD and analytical model simulations of (a) TCT signal and (b) electric field shape under different biases. Acceptor traps level $E_v + 0.5$ eV, concentration 3×10^9 cm^{-2}.

analytical model is able to reproduce in many details the dependence of the TCT signal on traps characteristics and applied voltages. For instance, from the evaluation of x_p (equation (2.8)), it is possible to predict that the higher the applied voltage, the larger will be the absolute value of x_p and x_n (equation (2.7)). At some point the electric field will be high enough to drag carriers across the interface that generate a current that will mimic the electric field discontinuity. The dependence of the TCT signal on the trap density is also included since the discontinuity of the electric field at x_t is also related to traps density through equation (2.2). Another interesting information can be obtained from the analytical solution with the diffusion included. Indeed, it is possible to see that, after a certain voltage, the tail of the current is no more visible. This is due to the fact that, when the diode is fully depleted, the electric field is never negligible inside the diode. Therefore, electrons will be rapidly collected by drift, and diffusion will not affect the signal shape. For lower voltages, there exists a region beyond which the electric field is almost zero. Therefore, once the electron cloud reaches this position, carriers will be collected mainly by diffusion, thus increasing the collection time. In figure 2.11, it is possible to observe the current shape at 10 V (fully depleted diode, figure 2.11a), and the electric field shapes at 4 V and 10 V (figure 2.11b).

2.2.4 Dependence on the nature of the traps

A comment on the influence of the type of traps on the TCT signal is needed. In case of N-type doped silicon bulk, the sign of the discontinuity at the interface needs to be positive (considering the notation in equation (2.2)) in order to have a double peak in the electric field profile (that will cause a double peak in the TCT signal). This happens when charged acceptors are present in higher concentration than charged donors, as they introduce a net negative charge at the interface layer (that in the notation used in this work corresponds to a positive value of N_t). Conversely, the presence of donors causes a double peak shape of the transient current when the bulk is lightly P-type doped (and therefore, the doping profile of the testing diode is opposite with respect to the one presented in figure 2.2). This is due to the fact that they will introduce a positive charge inside a bulk where, when depleted, is negative, resulting in a discontinuity of the electric field. This will give rise to a double peak shape of the electric field, and then of the transient current. By looking at equations (2.13) for traps at equilibrium and (2.16) for traps out of equilibrium, it is possible to deduce that, generally speaking, when acceptor traps have an energy level below the band mid gap, they will be charged, while donors will behave in the opposite way. Therefore, double peak will be observed in cases where acceptors energy levels are below mid gap when the diode doping profile is as in figure 2.2, and donors energy levels are above mid gap when the diode doping profile is opposite to the one presented in figure 2.2.

2.3 Extraction of charged traps concentration inside the interface layer

Once the transient current signals are obtained for several voltages, the voltage corresponding to the full depletion of the diode can be extracted. From figure 2.11a it is possible to observe that the higher the voltage, the shorter (in time) the transient current due to the increase in the electric field and thus in carrier velocity. For voltages greater than the full depletion value, the diffusion process will become less relevant since the electric field spreads over the whole diode (see the difference between 4 V and 10 V in figure 2.11b). At this particular voltage (which can be estimated from the electric field distribution inside the diode using the model), we can evaluate the time needed by the center of the electrons cloud to reach the end of the diode (t_{end}) using equation (2.38). This condition is recovered from equation (2.33), where x_t is replaced with x_{end}, that is the value of the thickness of the n-type doped bulk.

$$t_{end} = \frac{-x_{end} + \frac{N_A}{N_D} x_p + E_1 \ln\left(-x_{end} + \frac{N_A}{N_D} x_p\right) - K_1}{-v_{sat}}$$

(2.38)

When evaluating for example t_{end} at 4 V (according to the model, this is close to the full depletion of 4.8 V for acceptor traps concentration equal to 3×10^9 cm^{-2} and an energy level equal to $E_v + 0.5$ eV), its value is 11.3 ns. For voltages higher than this value, the current becomes negligible when $t > t_{end}$, while this will not happen for lower voltages since the diffusion current is still important for non fully depleted diodes. Then, integrating the signal up to t_{end}, the integral will remain constant above a certain voltage as the current will be

negligible for $t > t_{end}$ (all carriers will have been collected). However, when performing experiments, the integration time discussed above is an indication, but its value should be fine tuned according to the measurements. In our case this would be about 10 ns. Results of the integral are shown in figure 2.12. It is visible that above depletion the current integral
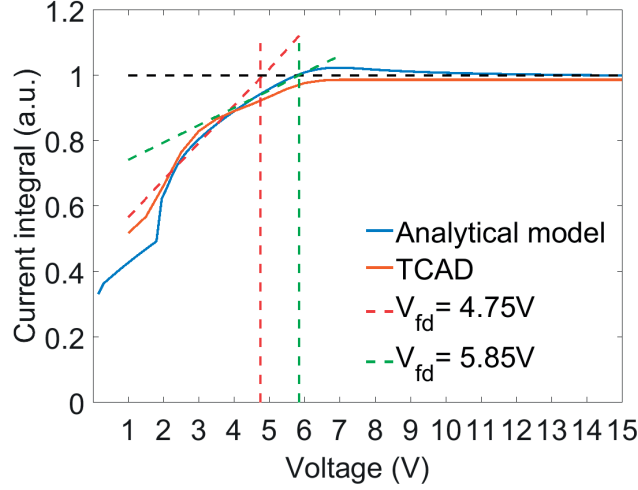
Figure 2.12 – TCAD and analytical model simulations of the normalized integral of the TCT current signals at different voltages. Acceptor traps level $E_v + 0.5$ eV, concentration 3×10^9 cm^{-2}.

starts to exhibit a plateau, same result obtained by Bates and Moll [84]. In an experiment, one could try to extract the voltage at which the plateau is reached as indicated by the lines in Figure 13. While the saturation value (horizontal line) is clearly defined, the second tangent is difficult to determine due to the shape of the curve. We have extracted a range of possible voltages for the intercept between $V_{fd} = 4.75$ V and $V_{fd} = 5.85$ V (the range is showed in figure 2.12, with the two relative tangents). From these voltages, the total charge density inside the volume can be calculated by using equation (2.12). Indeed, considering $x_n = x_R$ and $V = V_{fd}$ at full depletion, the only unknown is the volume concentration of the traps N_t (or the surface concentration $N_t d_t$ with $d_t = 3$ nm). From these calculations, it is obtained $N_t d_t = 2.78 \times 10^9$ cm^{-2} (for $V_{fd} = 4.75$ V) and $N_t d_t = 1.30 \times 10^9$ cm^{-2} (for $V_{fd} = 5.85$ V), while the charged traps surface concentration is 3×10^9 cm^{-2} (since acceptor traps with the energy level equal to $E_v + 0.5$ eV are fully ionized).Therefore, using TCT data, the method allows estimating the charged traps concentration, while fitting the TCAD model results to the obtained transient data will give a much more precise answer.

2.4 Validation with a non irradiated diode

2.4.1 Comparison between TCAD, analytical model and measurements

To validate the analytical model of TCT, a diode structure has been measured and compared to TCAD and analytical model simulation, where the bulk is lightly N-type doped (around 7×10^{11} cm^{-3}). The doping profile (PiN structure, as in figure 2.2) is the following: the P-type doped

Temperature	293 K
$\boldsymbol{\mu_{e,0}}$	900 cm^2/Vs
Doping concentration in the bulk	1.3×10^{12} cm^{-3}
P-type doping concentration	4×10^{18} cm^{-3}
Voltage (reverse bias)	100 V

Table 2.4 – Set of simulation parameters for analytical model validation.

contact is obtained by ion implantation with the doping peak around 4×10^{18} cm^{-3}, the N-type doped contact is realized with diffusion of phosphorus. The total thickness of the diode is 320 μm, and the surface is 4.41 mm^2. Fabrication has been performed at the clean room facility of the Center of Micronanotechnology (CMi) at the École Polytechnique Fédérale de Lausanne (EPFL), in the process that will be described in details in section 4.3.1. The measurements setup includes:

- a pulsed laser for the injection of carriers inside the diode, with a wavelength equal to 660 nm and a pulse length of the order of 100 ps long, applied to the P-type doped side of the diode;

- a voltage generator Keithley 2410, connected to the N-type contact, with the P-type contact connected to 0 V.

- an amplifier CIVIDEC C2HV Broadband Amplifier (gain 40 dB, bandwidth 2 GHz), connected to the N-type contact, to be used as a bias-tee and to amplify the TCT signal;

- an oscilloscope Agilent DSO9254A, to measure the hyperlinkabbrTCT signal.

All the experimental setup is provided by the CERN Solid State Detectors (SSD) group. Simulations have been performed with parameters listed in table 2.4. In figure 2.13, the comparison between the TCAD and analytical model simulation results and the measurement data is shown. By looking at the plot, some differences are observed between the different curves. Just after the light pulse, holes generated are immediately collected by the P+ contact and create the initial fast current pulse. Since the analytical model does not include this hole contribution, the first initial peak is absent from the analytical simulation, but this does not affect the TCT signal which originates from electrons displacement. In addition, parasite components during measurements (i.e. capacitances and inductances) are not accounted in the simulations (TCAD and analytical model) which could explain the slight mismatch with the measurements. To conclude, despite the differences analyzed above, the shapes of different signals are similar, and therefore it is possible to assess that the analytical model is validated for the purpose of predicting the TCT signal.

2.4.2 Parameters extraction

The analytical model can be used to extract important physical parameters: maximum electron mobility (or mobility at low electric field) and doping concentration in the bulk. However, there could be various set of parameters that could fit the experimental data. Basically, the
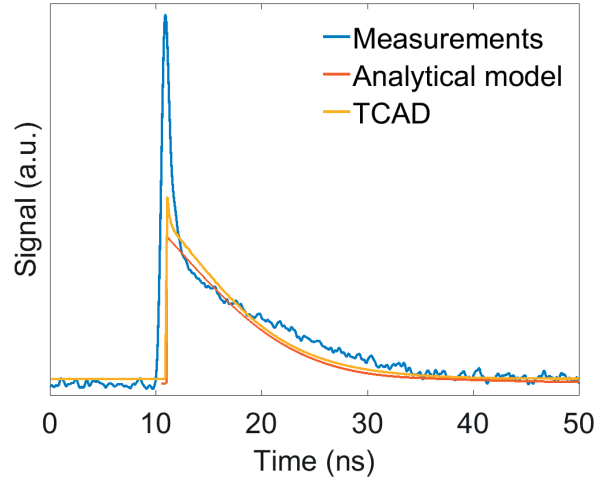
Figure 2.13 – Comparison between analytical model, TCAD simulations and measurement data.

Test	$\mu_{e,0}$ (cm^2/Vs)	Doping concentration in the bulk (cm^{-3})
1	600	1.3×10^{12}
2	900	1.3×10^{12}
3	1200	1.3×10^{12}
4	900	7×10^{11}
5	900	2×10^{12}

Table 2.5 – Parameters for extraction of mobility and doping concentration.

simulation parameters that can affect the shape of the transient current are the maximum electron mobility $\mu_{e,0}$, the doping concentration in the bulk and the temperature. The temperature and $\mu_{e,0}$ affect the mobility, and therefore the travel time of the electron cloud inside the diode (see equation 2.22). A higher $\mu_{e,0}$ leads to a higher electron mobility, i.e. a shorter current signal, while an higher temperature leads to a lower mobility. The doping concentration in the bulk also affects the electric field inside the diode. This happens in two different ways. First, it affects the depletion region width. Indeed, the lower the doping concentration in the bulk, the larger the depletion region. If the depletion region is large enough, the bulk will be totally depleted, and no current diffusion tail will be observed (that is the slower part of the signal). Secondly, the doping concentration affects the electric field intensity, and therefore the electron cloud velocity ($v = \mu\varepsilon$). In table 2.5 it is possible to see the various tests performed in order to find the parameters combination that allows to have the simulated current shape the most similar to the measured one. Figure 2.14 shows simulations and measurement where the combination of $\mu_{e,0}$ allows the best matching. Similarly, figure illustrates the impact of the doping. Evaluation of these graphs reveal that the best agreement is obtained for a $\mu_{e,0}$ of 900 cm^2/Vs, and a doping concentration of 1.3×10^{12} cm^{-3}. Figure 2.15 corresponds to the parameters in test 2. Note that the value of $\mu_{e,0}$ which better fits the data is below the one

expected for the low doped crystalline silicon substrate used in this work, since the maximum value of electron mobility in crystalline silicon is 1500 cm^2/Vs [83], much higher than the value reported in this paper. This difference could be due to presence of contaminants inside the silicon bulk.
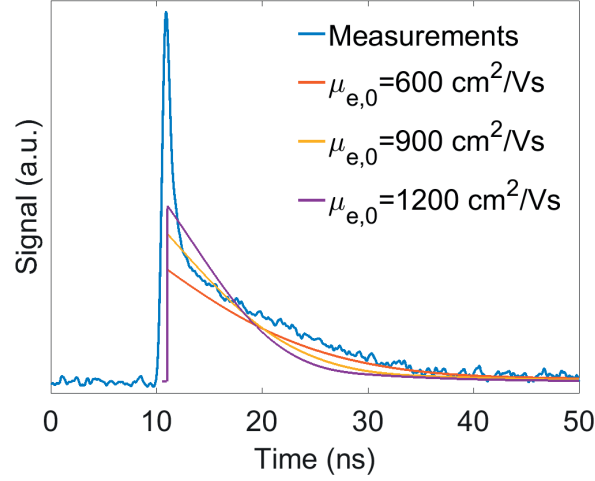
Figure 2.14 – Influence of maximum electron mobility on the transient current shape.
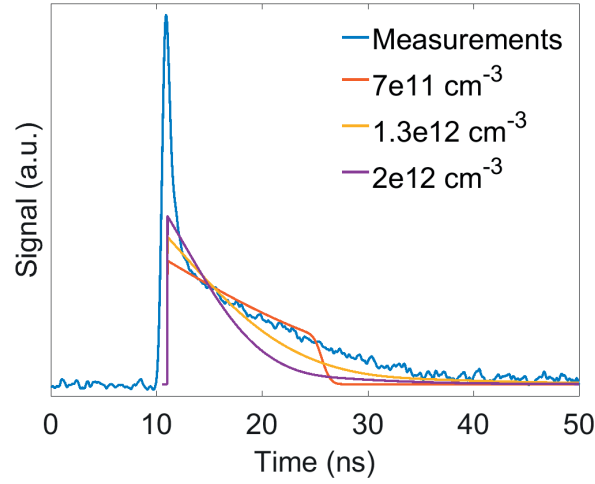
Figure 2.15 – Influence of the doping concentration in the bulk on the transient current shape.

2.5 Conclusions

In this chapter, a new characterization method for bonded interfaces with deep traps is investigated by means of numerical and analytical simulations of photo generated transient currents, the so-called TCT. It comes out that this technique is likely to be used to analyze the presence of traps inside ultra-thin interface layers in wafer bonded monolithic detectors,

and possibly in a variety of semiconductor heterostructures that can be fabricated with the promising low temperature wafer bonding technology. The physics based analytical model derived allows to extract physical parameters such as charge concentration in traps layers, and to easily analyze TCT signal without the need of complex TCAD simulations. The next chapter will be focused on measurements, and analysis, of diodes fabricated on silicon wafers bonded with a process similar to CMOS-compatible SAB of Flötgen et al. [58].

3 Schottky diodes for bonding interfaces characterization

*This chapter is based on the paper **"Transient Current Technique for Electrical Characterization of Bonded Interfaces in Bulk Silicon"**, submitted to the Journal of Applied Physics, by **J. Bronuzzi, D. Bouvet, C. Charrier, F. Fournel, M.F. Garcia, A. Mapelli, M. Moll, E. Rouchouze and J.M. Sallese**. Sections 3.1, 3.3, 3.4 and 3.5 are an original work performed by me, with the supervision of the other authors. Section 3.2 has been integrated with the description of the bonding process by the team at CEA-Leti.*

In this chapter, the analysis of bonding interfaces for CMOS-compatible SAB using TCT is described, with a method based on the study presented in chapter 2.

3.1 Introduction

For the analysis of the bonding interface by means of TCT it is necessary to have a diode whose role is to create an electric field inside the silicon. In chapter 2, simulations of the analysis were performed using a PiN diode. In the case of this study, however, it was not possible to bond a top wafer with diodes already fabricated, and therefore this step had to be performed after the bonding process. Doping is not compatible with the low temperature process since annealing or diffusion ask for high temperature steps that would affect the interface state. To circumvent this limitation, Schottky diodes were used instead of PN junctions since the processing temperatures did not exceed 160°C (for less than 2 min). In this chapter, a first section will contain the description the technology used for the low temperature silicon bonding. Then, a second section will deal with the integration of the Schottky diodes. Finally, the last section will present the TCT measurements and data analysis.

3.2 CMOS-compatible SAB

In this section, bonding of unprocessed wafers, performed by CEA-Leti in Grenoble, will be described. Twenty highly resistive (HR) P-type doped Czochralski wafers ($\rho > 5000$ Ωcm, 200 mm diameter) were used. A sketch of the process flow is summarized in figure 3.2. Wafers were first oxidized based on a wet thermal oxidation process to obtain a 1 µm thick silicon oxide layer. After this process, 18 wafers were divided into two groups depending on their role: top wafers and bottom wafers, sparing 2 of them that were kept as reference. Different bonding parameters were chosen (see table 3.1). Top wafers were first bonded to bulk silicon

(a)   (b)   (c)
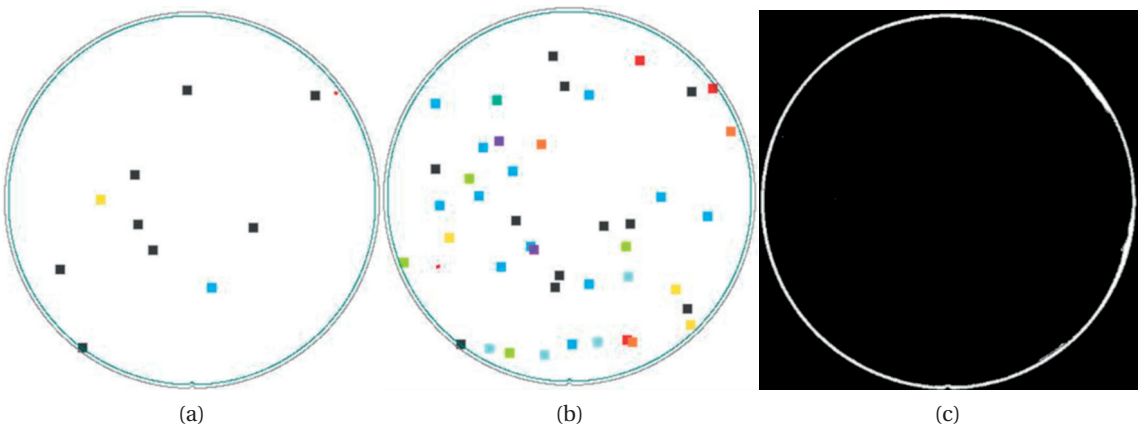
Figure 3.1 – SP2 particle characterization on 200mm silicon wafer with a threshold at 90 nm: a) before entering into EVG580CB and b) after the surface activation. c) Scanning Acoustic Microscopy of SAB Si/Si bonding after 400°C annealing.

carrier wafers with a direct hydrophilic bonding process before being thinned to the target thicknesses. These were determined through simulations to optimize the sensitivity of TCT to the traps concentration following the analytical model presented in chapter 2 (see table 3.1). After polishing and conditioning (for hydrophobic or hydrophilic processing) the bondable surfaces, top and bottom wafers were bonded using the EVG® 580 ComBond® machine using Ar sputtering and a bonding pressure of 0.95 MPa. The particle neutrality of the tool has been check with a Surfscan SP2 as shown on figure 3.1a and 3.1b in order to present any bonding defect or uncontrolled interface states. Only 33 adders with a threshold of 90 nm could be detected. Annealing of bonded substrates (called stacks) was performed at 400°C or at room temperature, as reported in table 3.1. An example of the bonding quality is checked by acoustic scanning microscopy as shown on figure 3.1c. The last step of the process was the release of the carrier wafer by grinding followed by complete etching of silicon using the 1 μm buried oxide as a convenient etch stop layer. The different batches of bonded wafers are listed in table 3.1.
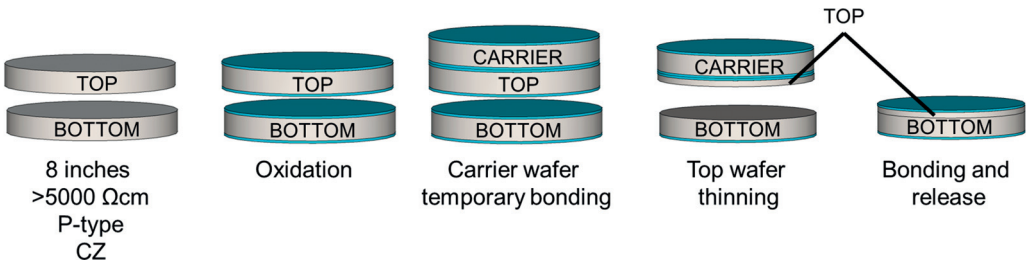
Figure 3.2 – Scheme of the process flow for CMOS-compatible SAB.

Stack name	Top wafer			Bottom wafer			Annealing
	Name	Th (µm)	Surface preparation	Name	Th (µm)	Surface preparation	
W1	P1	20	Hydrophobic	P10	725	Hydrophobic	400°C
W2	P2	20	Hydrophilic	P11	725	Hydrophilic	400°C
W3	P3	50	Hydrophobic	P12	725	Hydrophobic	400°C
W4	P4	50	Hydrophobic	P13	725	Hydrophobic	400°C
W5	P5	50	Hydrophobic	P14	725	Hydrophobic	Room T
W6	P6	50	Hydrophobic	P15	725	Hydrophobic	Room T
W7	P7	50	Hydrophilic	P16	725	Hydrophilic	400°C
W8	P8	50	Hydrophilic	P17	725	Hydrophilic	400°C
W9	P9	50	Hydrophilic	P18	725	Hydrophilic	Room T
W19	P19			Reference			
W20	P20			Reference			

Table 3.1 – List of wafers and bonding parameters for the different bonding tests performed.

3.3 Fabrication and characterization of Schottky diodes

3.3.1 Process flow

Fabrication of Schottky diodes on bonded (and reference) wafers was performed at CMi. In these laboratories, diameter of wafers are limited to 100 mm, and therefore a downsizing from 200 mm is needed. For this purpose, the top wafer surface was covered with 5 µm of photoresist, and laser cutting was performed at Sil'tronix, following the scheme in figure 3.3, where it is possible to see the notation used to label 100 mm wafers (that is, adding A or B to the stack label, according to the position of the wafer). 100 mm wafers W03A, W06A, W07A
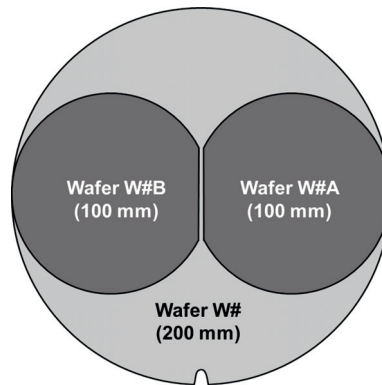
Figure 3.3 – Scheme for downsizing from 200 mm to 100 mm wafers.

and W20A were chosen to be processed. The top wafer contact (top side) was fabricated with aluminum, while the bottom wafer contact (bottom side) was fabricated with platinum. These metals were chosen after preliminary tests on Schottky diodes fabrication. Holes for top light injection TCT were also perfomed in the middle of the diode (in a matrix with 5 square holes
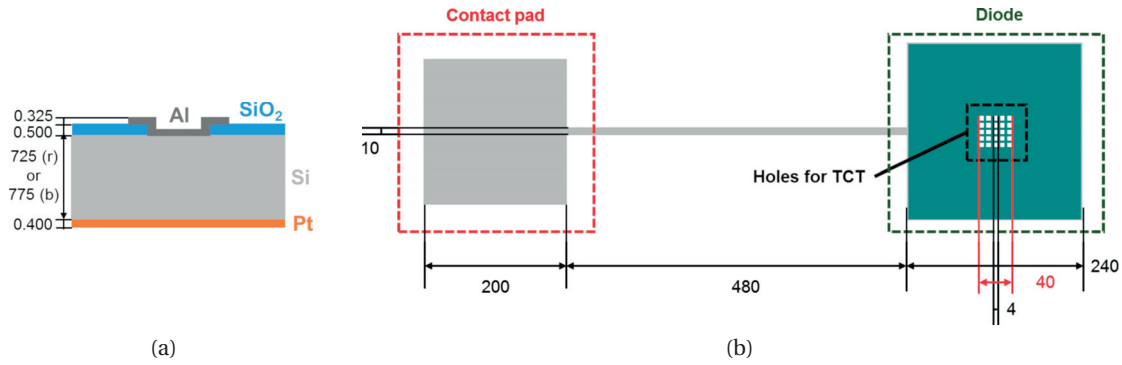
Figure 3.4 – (a) Cross section and (b) layout of a Schottky diode. Dimensions in figure are expressed in µm.

per edge, 4 µm wide). The footprint dimension of diodes was 240 µm, the footprint dimension of conctact pads was 200 µm, connected to the diode through a 10 µm wide, 480 µm long aluminum path. First wafers were cleaned, with Microposit® remover 1165 at 70°C (to remove the 5 µm thick photoresist) and then with RCA cleaning without HF. Then, silicon dioxide was thinned down to 500 nm by wet etching in BHF 7:1. After this step, the first lithography for the definition of diodes areas was performed on the top side using 1 µm of photoresist AZ ECI 3007, while the bottom side was protected with 4 µm of photoresist AZ ECI 3027. Etching of silicon dioxide was performed with BHF 7:1, to completely remove the oxide on the diode surface. Then, photoresist stripping and RCA cleaning step were performed to assure the cleaning of the diode surface, and aluminum was deposited by sputtering (325 nm thick), with a previous argon bombardment cleaning in the same tool. A second lithography, to pattern the diodes, the contact pads for measurements and the holes to assure light injection, was performed on the top side, using 1 µm of photoresist AZ ECI 3007, while the bottom side was protected with 4 µm of photoresist AZ ECI 3027. Aluminum dry etching was performed, and the photoresist stripped. The last step was the deposition of platinum. For this, the top side was protected with 4 µm of photoresist AZ ECI 3027, and then the bottom side was etched with BHF 7:1, and then sputtering of platinum (400 nm thick) was performed on the same side, with a previous argon bombardment cleaning. Figure 3.4a shows the cross section of the diode at the end of the process, while figure 3.4b shows the layout.

3.3.2 CV and IV measurements

Before the TCT characterization, the diodes were tested through IV (current versus voltage) and CV (capacitance versus voltage) measurements using a Keithley 2410 voltage generator for biasing, a Keithley 6485 for current measurements, and an Agilent E4980A LCR meter for capacitance measurements. The voltage was applied to the top contact, while the bottom contact was connected to ground. The IV (figure 3.5a) and CV (figure 3.5b) characterizations confirm a standard Schottky behavior [83]. Both CV and IV characteristics are consistent with a N-type doped substrate where the reverse biasing is obtained by setting the top electrode to negative values. However, since the doping of silicon is expected to be P-type, such a reverse
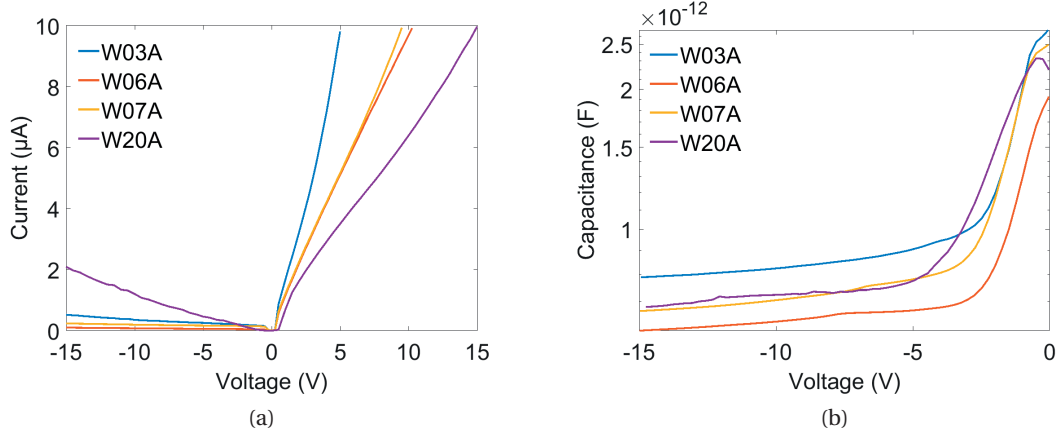
Figure 3.5 – (a) IV and (b) CV characteristics of Schottky diodes fabricated on different wafers.

bias configuration should occur with a positive voltage on the top contact. This unexpected behavior is also evidenced in measurements on MOS capacitors fabricated on the same substrates (figure 3.6). Evidently, the wafers happen to be N-type. This surprising finding can be explained by the generation of thermal donors that takes place during the high temperature process prior the wafer bonding (oxidation) and by the annealing (performed at 400°C on some wafer). Indeed, as reported by Bruzzi et al. [67], these processes could activate oxygen in silicon, generating donors, that could reach a concentration high enough to invert the doping type of silicon. The range of temperatures at which this occurs spans from 30°C to 900°C, with two peaks in the donors generation rate at 450°C and 750°C [79].
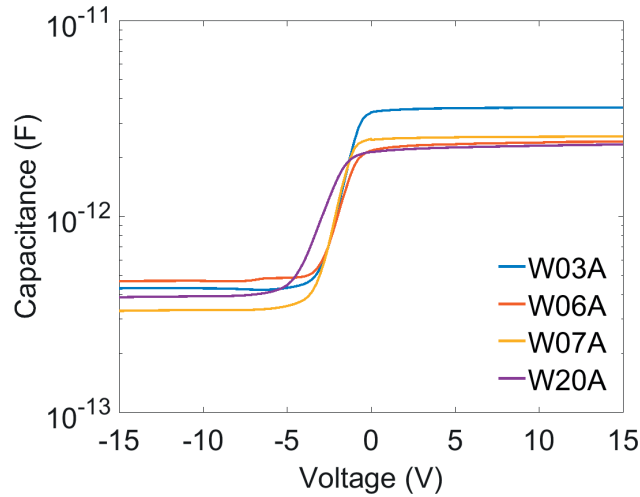
Figure 3.6 – CV characteristics of MOS fabricated on different wafers.

3.4 TCT Measurements of Schottky diodes

3.4.1 Edge TCT measurements

To confirm that Schottky diodes are properly working, and to start the study of the electrical properties of the bonding interface, eTCT measurements were performed. Charges were injected on the side of the diode bulk by means of an IR laser (wavelength 1064 nm), with a beam diameter of 10 µm at the focus point (located under the middle of the diode surface). The reverse bias voltage was applied with a Keithley 2410 through a CIVIDEC C2HV Broadband Amplifier (gain 40 dB, bandwidth 2 GHz) to the top side contact, from which also the transient current signal was recorded using an oscilloscope Agilent DSO9254A. The collected charge was measured by integrating the transient current signal, and a map of this charge was generated for diodes W20A (reference in figure 3.8a) and W03A (bonded, in figure 3.8b), at -60 V. Figure 3.7 shows the reference system. From plots in figure 3.8 it is possible to observe the extension
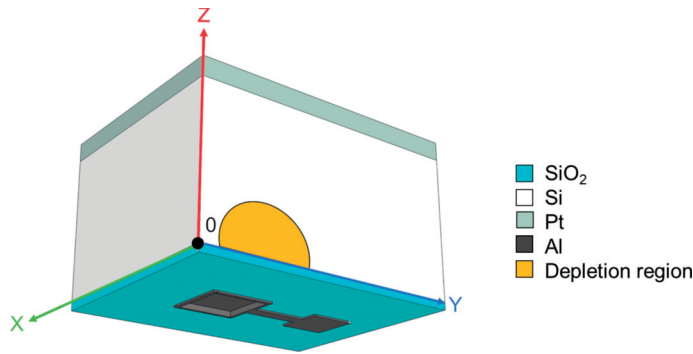
Figure 3.7 – Reference system of 2D plots shown in figure 3.8. The black dot indicates the position of the 0, while the yellow semicircle shows where the depletion region is located.

of the depletion region under the diode surface, since charge collection occurs only in the depletion region. From figure 3.8a, it is possible to observe that silicon depletes in all directions, since there is not any barrier in the bulk, and from depletion width estimation it is possible to

(a)   (b)
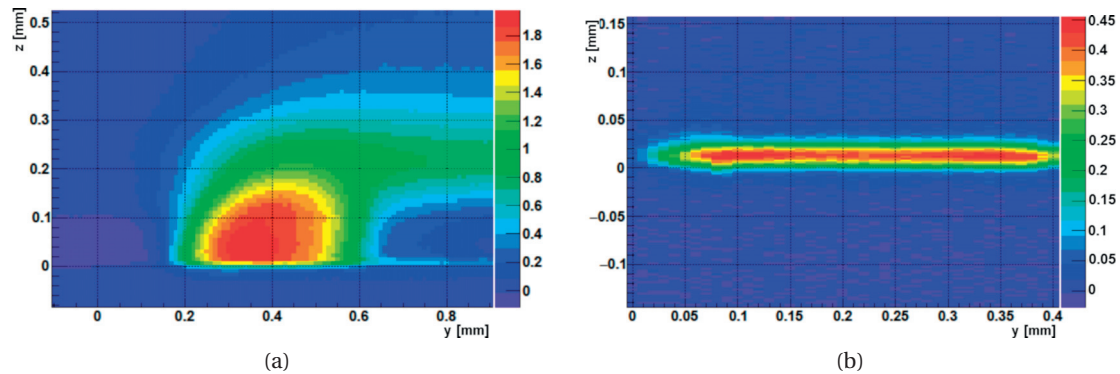
Figure 3.8 – (a) Collected charge for the reference diode (W20A) and (b) for the bonded diode (W03A).

estimate the effective doping concentration (of donors), that is 10^{12} cm^{-3} (a value consistent with previous studies of thermal generation of donors [67]). The long tail on the right of the plot represents a field that is generated by capacitive coupling between the contact pad, the conduction path and the silicon (see figure 3.4b), through the passivation oxide. Figure 3.8b shows a completely different shape of the depletion region. Indeed, it is only 25 μm thick (while in the case of the reference diode it is around 300 μm thick). Since the only difference between the two diodes is the presence of the bonding interface, a first conclusion is that this layer of amorphous silicon blocks the collection of charges generated between the interface and the bottom side of the diode. The reason for which the depletion region is only 25 μm thick and not 50 μm (full thickness opf the top part of the stack, see table 3.1) is the deflection of the IR laser. Indeed, the light beam is tilted by the borders of the device due to the Snell law $n_{air}\sin\theta_{air} = n_{Si}\sin\theta_{Si}$, where $n_{air} = 1$ [85] is the refractive index of air, $n_{Si} = 3.55$ [86] is the refractive index of silicon, θ_{air} is the angle of incidence with the edge of the diode and θ_{Si} is the angle of refraction inside silicon, as shown in figure 3.9a. During measurements, the diode was not perfectly flat, and therefore this tilting impedes the charge generation at the edges of the depletion region. Moreover, imperfections in the edges caused by dicing also could generate light deflection. However, if the diode is diced in the middle, then all the depletion region would be illuminated, and observed to be 50 μm thick. Results are shown in figure 3.9b, where the tail on the right of the image is again due to capacitive coupling between the contact pad, the conduction path and silicon through the passivation oxide (see figure 3.4b).

(a)   (b)
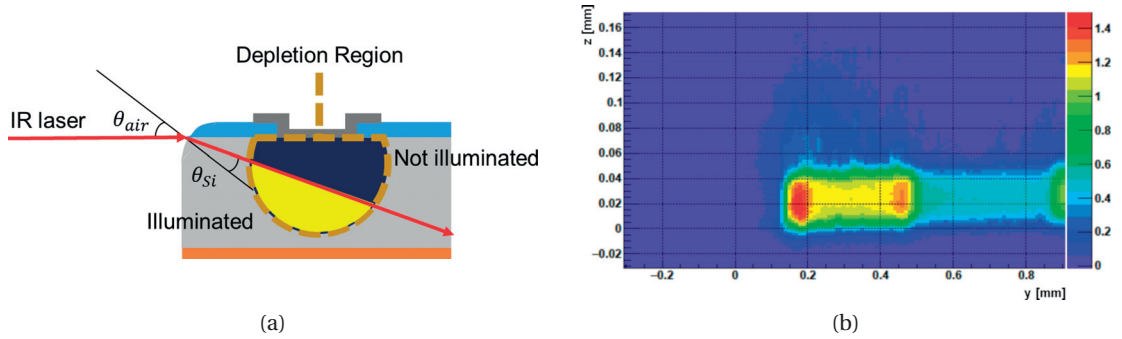
Figure 3.9 – (a) Light deflection causes by edge imperfections, where it is possible to observe the effects of Snell law on measurements, and (b) eTCT measurements of diced diode.

3.4.2 Top TCT measurements

Top TCT measurements are conducted with a 50 ps pulsed laser emitting at a wavelength of 660 nm. The spot diameter on the surface of the device is 10 μm and illumination occurs through the pinholes in the center of the diode (see figure 3.4b). The biasing and the measurements are conducted with the same setup used for eTCT. First measurements were performed on diodes fabricated on the same wafers investigated in the previous analysis. Results for the diode W20A (reference) show a standard behavior (see figure 3.10a) of a TCT signal generated by a fully depleted region. In this case, different bias voltages are applied, and the shape of
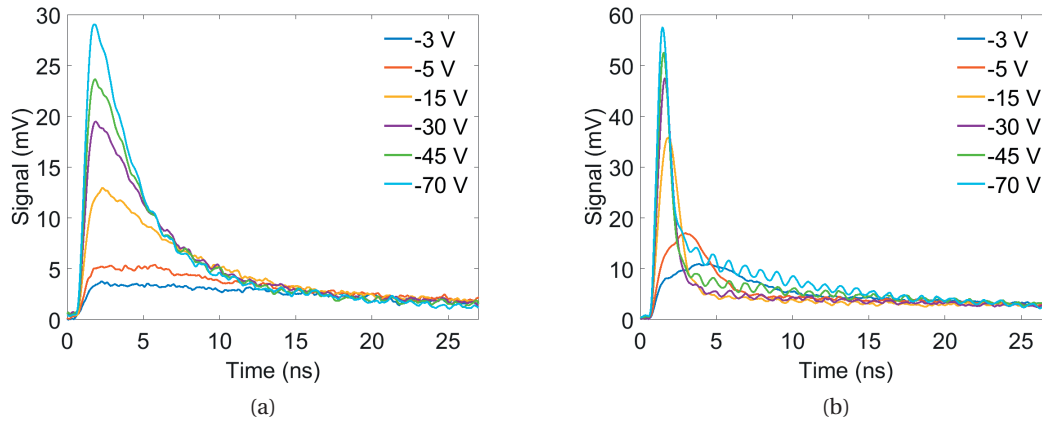
Figure 3.10 – TCT signals from measurements on diodes (a) W20A (reference) and (b) W03A (bonded), at different bias voltages.

the TCT signal is decaying according to the Ramo's theorem [87] in case of a linear electric field, as it happens in a ideal diode in reverse bias. The situation is different for the bonded wafers W03A where a different behavior is reported in figure 3.10b. The currents decay have a different shape. A first peak is observed at around 2 ns, followed by a slowly decaying tail. As in eTCT, this is a clear signature of the effect of the bonding interface. This anomalous behavior is further confirmed in figure 3.11 reporting TCT measurement of two additional bonded diodes, W06A (figure 3.11a) and W07A (figure 3.11b). These shapes are similar to the one observed in diode W03A, but W06A is slightly different when looking at the long tail after 3 ns. Indeed, for diodes W03A and W07A the long decay starts increasing in amplitude with the bias for applied voltages higher than -45 V. For diode W06A, we can also observe such a behaviour, but for voltages higher than -70 V. In the next section, an analysis of TCT curves is performed in details with additional simulations using the analytical model presented in chapter 2.
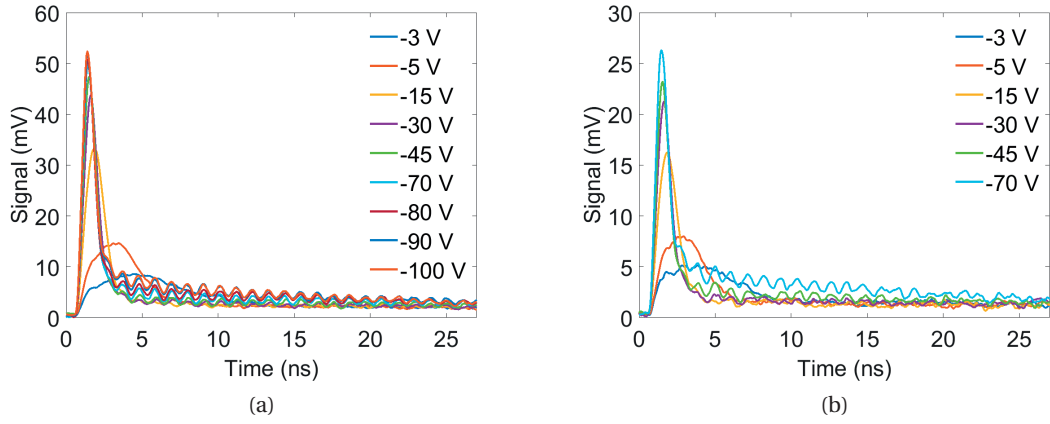
Figure 3.11 – TCT signals from measurements on diodes (a) W07A (bonded) and (b) W06A (bonded), at different bias voltages.
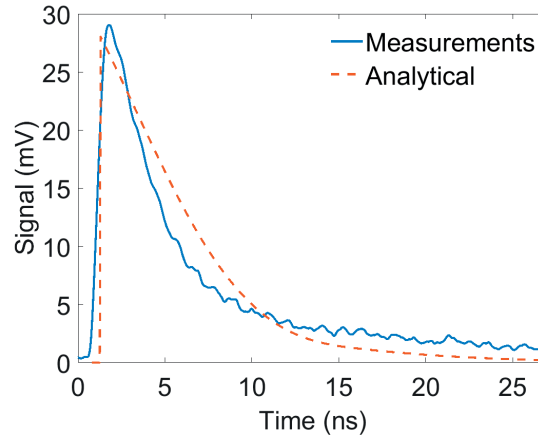
Figure 3.12 – Comparison between analytical simulations and measurements on diode W20A (reference) at -70 V.

3.4.3 Discussion

In order to understand the behavior of the bonding interface, the analytical model developed in chapter 2 is used. This gives a fast and comprehensive analysis of the main phenomena induced by the interface. A first simulation is performed in order to determine the doping concentration in the silicon bulk, by comparing the results of the analytical model for a standard diode with the measurements on the reference not bonded wafer W20A. In figure 3.12 it is possible to observe a good matching between simulations and measurements for a diode with a N-type bulk doping concentration of 1.5×10^{12} cm^{-3} (close to the value obtained from e-TCT measurements analysis), at -70 V. In the work of Flötgen et al. [58] the bonding interface generated by the wafer bonding technique was found to be an amorphous layer spreading in 3 nm. Introducing this thickness in the analytical model (chapter 2), a good matching with experimental data is obtained for a traps density of the order of 3×10^{9} cm^{-2}.

Indeed, simulations of bonded diodes show that the introduction of an interface layer with these traps concentration gives curves with the same shape of measured ones. The most important parameter in this case happens to be the quantity of ionized traps, which influences the electric field profile of the diode by introducing a discontinuity at the interface. In figure 3.13, it is possible to observe 3 simulated curves for different ionized traps densities (2.7×10^{10} cm^{-2}, 5.7×10^{10} cm^{-2} and 8.7×10^{10} cm^{-2}) and compare them with measurements of diode carried out on W03A (bonded) at -70 V. Obviously, there is a strong influence of the interface trap density on the whole TCT shape, and the best matching is obtained unambiguously for a density of charge of 5.7×10^{10} cm^{-2} (donor traps, positively charged). Note that the long tail
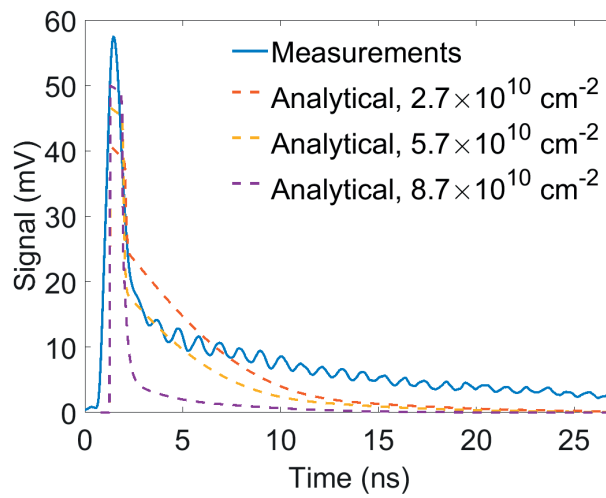
Figure 3.13 – Comparison between analytical simulations with different ionized traps densities and measurements on diode W03A (bonded) at -70 V.

that is visible after 3 ns in measurements (figures 3.10 and 3.11) is not present in the analytical model simulations. By performing the same simulations with TCAD, it is possible to observe that this tail is related to diffusion processes in the undepleted bulk. Indeed, in figure 3.14 the simulations performed at -45 V of the Schottky diodes are shown, with 5.7×10^{10} cm^{-2} ionized traps, with the 725 μm thick bulk and without it, compared to measurements. The tail disappears in absence of the bulk. To add the contribution of the undepleted bulk to the analytical model, the tail from measurements was fitted with an exponential decay such as $\exp(-\xi t)$, with $\xi = 0.0203$ ns^{-1} . Adding this exponential to the model (in figure 3.15), it is possible to observe good matching (similar shapes of the transient current) between the simulated and the measured data, in both cases, bonded and reference diodes, using the same parameters of simulations in 3.12 and 3.13. To explain the reason for which the long tail after 3 ns starts to be influenced by the applied voltage for values higher than a certain threshold, it is necessary to observe the electric field profile, shown in figure 3.16a for TCT with an ionized trap density equal to 5.7×10^{10} cm^{-2}. From this plot, we observe 2 regimes: one where the discontinuity of the electric field cancels it at the interface (depth of 50 μm), which happens at relatively low voltages, and the other at higher voltages where, the electric field
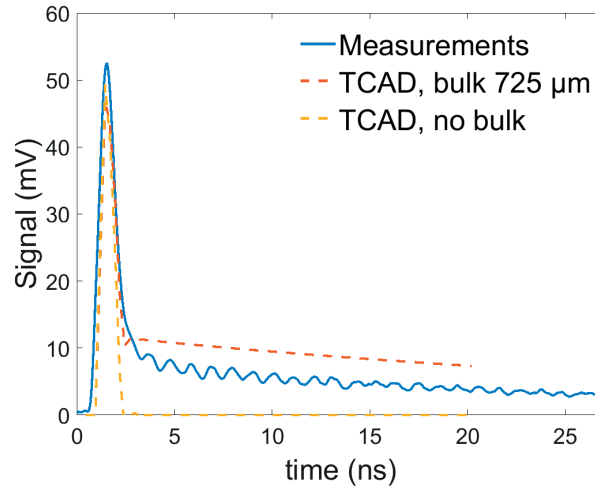
Figure 3.14 – Comparison between Sentaurus TCAD simulations and measurements of TCT, with and without the 725 μm bulk, at -45 V, with 5.7×10^{10} cm^{-2} ionized traps.
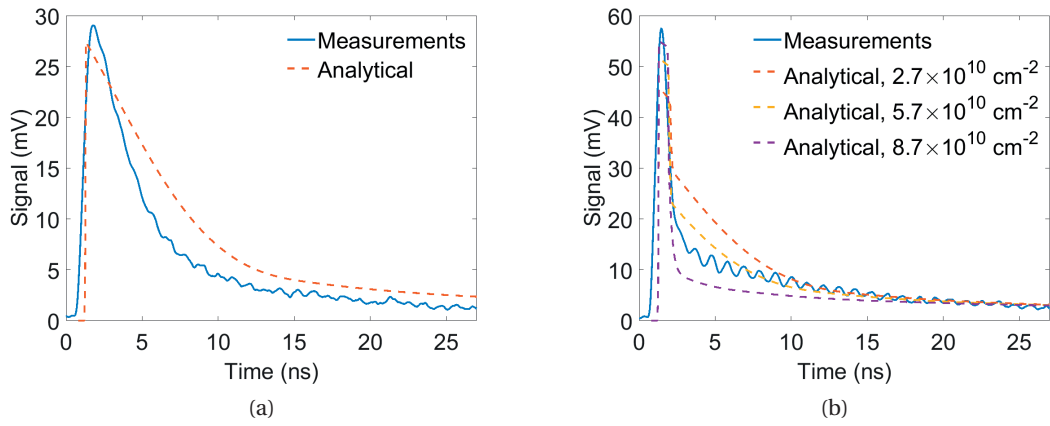
Figure 3.15 – Comparison between analytical model with exponential tail and measurements.

extends beyond the interface, creating a depletion in the subsequent bonded wafer. Indeed,

(a)   (b)
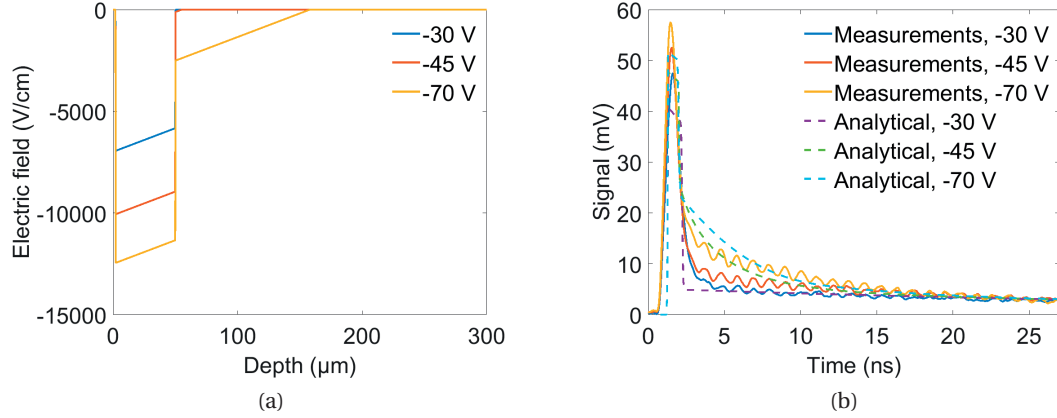
Figure 3.16 – (a) Electric field profile from analytical simulations of diode W03A (bonded) for different applied voltages, at an ionized traps density of 5.7×10^{10} cm^{-2} and (b) TCT signal simulations with the same parameters.

considering measurements on the diode W03A (figure 3.10b), if the bias voltage is smaller than -45 V, the long tail does not depend on the voltage since the bulk of the bottom wafer is not depleted, and it can be explained by the extrinsic capacitive discharge as in measurements on diode W20A. However, when the voltage is larger than -45 V, the electric field discontinuity at the interface is smaller than its value at the interface, and therefore the depletion region will extend in the bottom part of the wafers stack. The presence of an electric field will generate a drift across the bonding interface, meaning that the tail of the TCT signal will now be generated by the electric field. This result is evidenced by the analytical model for two different regimes. The first one is when a diode of 50 µm thick is considered, and is valid for low voltages (-45 V in case of diode W03A) where the depletion region is confined by the charged interface (for instance, -30 V in figure 3.16a). The second case is when the depletion region extends further in the bottom wafer, which occurs for higher voltages (for instance, -70 V in figure 3.16a). Figure 3.16b illustrates the currents simulated with the analytical model that are compared with measurement done on diode W03A (bonded). The density of equivalent ionized traps can therefore be obtained by simulating a TCT curve with the same ratio between the peak and the tail for voltages where depletion extends over the bonding interface. The values obtained for the diodes considered in this work are presented in table 3.2. These values give a first hint

Diode	Voltage Threshold (V)	Traps density (cm^{-2})	Surface treatment	Annealing
W03A	-45	5.7×10^{10}	Hydrophobic	400°C
W06A	-70	9.3×10^{10}	Hydrophobic	Room T
W07A	-45	5.7×10^{10}	Hydrophilic	400°C

Table 3.2 – Values of interface traps densities for measured bonded diodes.

on the impact of different process bonding parameters. For instance, it seems that annealing at 400°C reduces the density of ionized traps, while the surface treatment prior bonding does not affect this parameter. Similarly, a lower traps density could be related to a better quality interface, consistent with the fact that stacks W03A and W07A were annealed, while stack W06 was not.

3.5 Conclusions

In this chapter, a method for the characterization of amorphous interfaces in bulk silicon wafers using TCT was presented and discussed in details. This characterization method can be used to study interface charged defects generated during the bonding process. Importantly, despite the interface being electrically conductive in the common sense, extracting free carriers across it is not guaranteed because of electrostatic issues arising with interface charge traps. An estimation of the traps density is then mandatory, which is proved to be feasible with the TCT technique. In this context, the bonding process analyzed in this paper generates an interface which effect is to prevent mobile charges to be collected by an active circuit implemented across the interface. Considering the working principle of radiation detectors, their fabrication using CMOS-compatible SAB could strongly affect charge collection, and therefore detection performances. A different characterization method is presented in appendix A, and also in this case, results suggest that the interface could strongly affect the performances of radiation detectors. To solve this problem, two solutions have been identified, on two different levels. From a process level, it could be possible to reduce the number of traps by changing the bonding parameters, for instance by using a different plasma source for the surface preparation prior bonding, or by changing the annealing time. In this case, the discontinuity of the electric field at the interface would decrease, reducing its field blocking effect. From a design level, a solution to reduce the effects on radiation detectors performances could be to place the bonding interface at the position of the PN junction. This comes directly from the consideration that the maximum of the electric field intensity is located at this point. Therefore, the electric field discontinuity should be less effective. This can be studied by TCAD simulations.

Figure 3.17 (where results from TCAD are compared to the analytical model) shows that substituting Schottky diodes with PN diodes, in case of traps interface presence at 50 µm from the junction, does not change the TCT signal and the electric field, that are similar to figure 3.16. In simulations, the bulk silicon doping concentration is 1.5×10^{12} cm^{-3}, N-type, the traps concentration is 5.7×10^{10} cm^{-2}, and the reverse bias is 70 V. In figure 3.18 it is possible to observe the effects on TCT signal and electric field of bonding interface placed at the junction (simulations are performed with TCAD using the same parameters of the ones presented in figure 3.17, except for the position of the interface). The TCT signal is similar to the one of a standard diode. Also the electric field is similar (figure 3.18b), with the exception of the peak at the junction, that however does not affect the signal, and therefore the charge transport in the diode. To conclude, by combining this design solution with process optimization, it could be possible to fabricate a radiation detector with this technique with CMOS-compatible SAB, with performances that are not affected by this process. In the next chapter, the development

(a) (b)
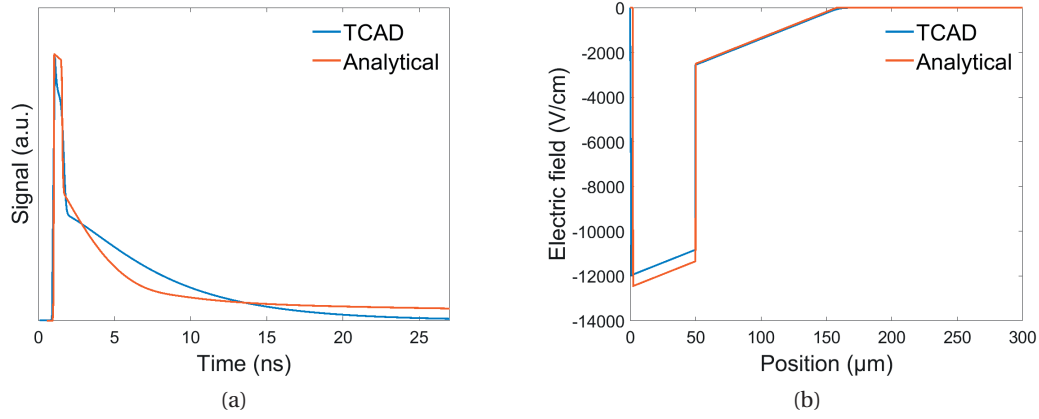
Figure 3.17 – Comparison between TCAD simulations and analytical model of (a) TCT signal and (b) electric field of a PN Diode, in case of interface located at 50 μm from the junction. The signal shape, as well the electric field profile, are similar to Schottky diodes measurements shown in figure 3.16. Traps concentration is 5.7×10^{10} cm^{-2}, reverse bias is 70 V.

(a) (b)
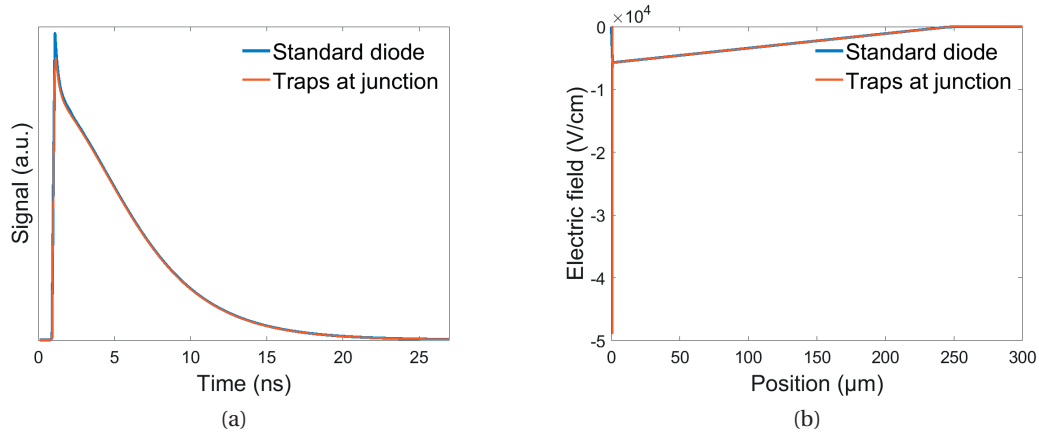
Figure 3.18 – Comparison of (a) TCT signal and (b) electric field between a standard diode and a diode with bonding interface at the PN junction. The signal shape, as well the electric field profile, are similar. Traps concentration is 5.7×10^{10} cm^{-2}, reverse bias is 70 V.

of a new charge injection method for TCT, to enable the use of setups simpler than lasers for light injection, is described.

4 Electrical injection TCT

*This chapter is based on the paper **"Principle of the electrically induced Transient Current Technique"**, edited by JINST, volume 13, May 2018, doi: https://doi.org/10.1088/1748-0221/13/05/P05021, by **J. Bronuzzi, M. Moll, D. Bouvet, A. Mapelli and J.M. Sallese**. The paper is an original work performed by me, with the supervision of the other authors.*

In this chapter, a new approach to charge injection for TCT analysis is presented, the electrical injection TCT (el-TCT). It is obtained through the implementation of a lateral PiN structure in an operational device, that is assumed to give only little or no impact on its performance and would allow to apply the TCT technique during irradiation tests and experiments. Such characterization is impossible to perform with light injection TCT. A proof of concept for el-TCT is presented, while the implementation of structures in operating devices is not studied in detail. This study is perfromed through numerical simulations carried out with the Sentaurus TCAD software, resulting in an adaptation of the silicon diode layout for el-TCT applications. These simulations are followed by the design, fabrication and experimental characterisation of silicon structures.

4.1 Principle and simulations of el-TCT

4.1.1 The device architecture

A cross section of an el-TCT device structure is shown in figure 4.1a. and table 4.1 summarises the device parameters used for the TCAD simulations.

P_W	N_W	S	Th	C_p	$C_{B,n}$	$C_{C,n}$	DL_p	$DL_{B,n}$	$DL_{C,n}$
7	3	2	320	4.5×10^{18}	5.82×10^{19}	10^{19}	1.25	1.02	0.7

Table 4.1 – List of doping parameters for TCAD simulation. P_W, N_W, S, Th, DL_p, DL_n, DL_n are expressed in μm and C_p, $C_{B,n}$, $C_{C,n}$ are expressed in cm^{-3}. C_p is the peak P-type doping concentration at surface, $C_{B,n}$ is the peak N-type doping concentration at surface (front side, contact B), $C_{C,n}$ is the peak N-type doping concentration at surface (back side, contact C), DL_p is the P-type doping Gaussian width, $DL_{B,n}$ is the N-type doping Gaussian width (front side, contact B), $DL_{C,n}$ is the N-type doping Gaussian width (back side, contact C).

(a)   (b)
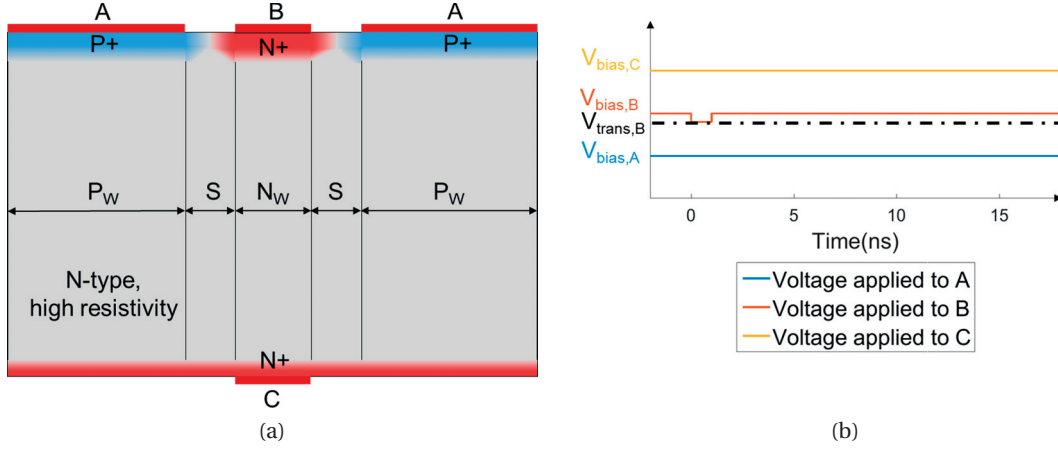
Figure 4.1 – (a) Cross-section of a device for el-TCT and (b) scheme of the applied voltage signals. Diffusion doping is shown in the gap between the electrodes. P+ and N+ indicates respectively p-type and n-type doped regions.

The N-type substrate doping concentration was set to 7×10^{11} cm^{-3}. Gaussian doping profiles with maximum concentrations at the surface have been used to simulate the strongly doped silicon regions generated by implantation and then diffusion. The doping of the top side extends into the P_W and N_W regions, that are the P-type (P+) and N-type strongly (N+) doped region on the front side of the device (see figure 4.1a). In the S regions (corresponding to the spaces between the P_W and the N_W regions), the doping is obtained by lateral diffusion from the P_W and the N_W regions. The thickness Th of the device is 320 μm. The simulated structure represents only a small part of the devices produced in this work (see Figure 8). In the el-TCT concept, injection of free charge carriers (electrons in our case) is done by means of N-type implants surrounded by P-type doped regions (respectively red and blue regions in figure 4.1a). Note that the P-type doped layers constitute the front electrodes of the detector which are also implemented in devices for optical TCT, while the N-type doped layers are specific to el-TCT architectures. The electrons are injected into the lightly doped substrate by pulsing node B from $V_{bias,B}$ to $V_{trans,B}$ (e.g. for 1 ns), while the voltage difference between nodes A and C is set to operate the PN junction in reverse bias (e.g. $V_{bias,A} - V_{bias,C} < 0$) creating an electric field in the bulk of the PiN structure. A biasing scheme (including the voltage waveform applied to contact B) is shown in figure 4.1b. This architecture and the related biasing sequence are optimized so that injection takes place at node B. The principle of operation and device optimization will be addressed in the next section.

4.2   Physical principle

The injection of carriers into the lightly doped region depends strongly on the shape of the doping profiles and the distance S between the peaks of the Gaussian profiles of the implants, i.e. the distance between the edges of the implanted areas (see figure 4.1a and table 4.1). A static IV characteristic obtained from TCAD simulations of the current exiting at node C versus
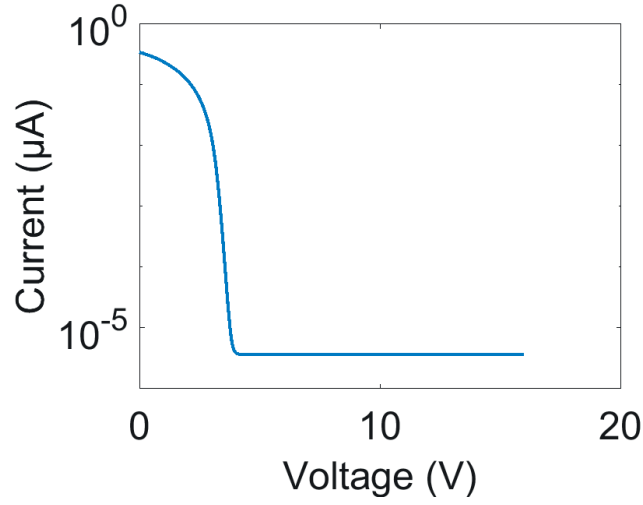
Figure 4.2 – Static IV characteristic of the current at node C versus the positive voltage at node B (voltages applied at node C and A are respectively +200 V and +0 V).

the voltage applied at node B (the voltages applied at nodes C and A are respectively +200V and +0V) is shown in figure 4.2. As long as the voltage at node B is higher than +4 V, current does not flow. In other words, applying a voltage between A and C so that the PiN diode remains reverse-biased blocks injection of electrons from B to C. The injection of electrons becomes effective only when the voltage on the N-type node B is lower than +4 V. For these voltage values, the IV characteristic follows a resistive behaviour. A current appears between nodes B and C during injection, whereas the lateral PN junction remains reverse biased and controls the electrostatic potential below the N-type doped region at node B. In fact, the injection process is controlled by the fringing electric field created by the lateral P-type and N-type doped layers. In order to understand how electrical injection is controlled by external voltages, a cross-section of the potential profile at the centre of the device is plotted in figure 4.3 during transient operation for two relevant biasing conditions: (a) with no voltage pulse applied (before 0 ns, with $V_{bias,B}$ equal to +4 V) and (b) with a pulse voltage of $V_{trans,B}$ equal to +3 V. The 2D plot of the conduction band edge energy before the pulse reveals the presence of an energy barrier that blocks electrons to be injected. This barrier is visible in the conduction band edge potential plot of figure 4.3 obtained along the centre of the device, i.e. along the injection channel. The voltage applied to that P-type doped layer creates a lateral barrier which encloses and isolates the source of electrons (N-type node). Similarly, the electron density along the same line is shown in figure 4.3a and it is possible to see that the channel ends when the electron density becomes negligible, which corresponds to a depth of about 4 μm. Next, when the voltage applied at node B is lowered to +3 V during 1ns, the shape of the potential is modified and a channel starts to open (see figure 4.3b). Indeed, the energy barrier for electrons is decreased. After 1 ns, the electron concentration at 4 μm is about 3×10^{13} cm^{-3}, much higher than before the pulse (3×10^{10} cm^{-3}). Finally, when the potential at node B is reset to the off-state potential after 1 ns, the energy barrier goes back to its initial value and

the channel switches off again. The time scale of the pulse corresponds to the time needed for electrons to reach the region where the electric field created by the reverse biased PiN junction will make them drift towards node C (corresponding to the blue area in figure 4.3) preventing electrons to flow towards node B. It is this displacement current that creates the transient current signal at the output node C.

4.2.1 Thermionic emission

To get a deeper understanding of the electrical injection principle, the influence of bias voltages is analysed by carrying out TCAD simulations. Six combinations of voltages have been used and are listed in table 4.2. In all cases, the voltage applied to contact A is equal to 0 V, the voltage applied to node C is equal to +200 V, and the duration of the pulse applied to node B is 1 ns, as shown in figure 4.1b. The current is always recorded at node C. As shown in

Combination	$V_{bias,B}$ (V)	$V_{trans,B}$ (V)
1	+4	+3
2	+5	+4
3	+7	+6
4	+4	+2
5	+7	+1
6	+6	+2

Table 4.2 – List of voltage combinations applied at node B in TCAD simulations.

figures 4.4a and 4.4b, the current height depends solely on the pulse voltage $V_{trans,B}$, which can be seen by comparing the current signals of combinations 4 and 6. Combination 3 shows no current pulse, as the barrier blocks the electron injection. In case of combination 5, we observe a significant change of the shape of the pulse. This is because the injected charge is high enough to locally modify the electric field of the diode during the drift (see figure 4.4c, where the electric field profile during the drift is shown when the electron cloud is located at position 150 µm). A similar result is obtained by comparing the injected charge Q_{in} and the potential barrier height $\Phi_{B,0}$ (considering figure 4.3, it is defined as the difference between the maximum of the conduction band edge potential and its value at position 0 µm) at time 0 ns (i.e. during the voltage pulse) between the combinations as listed in table 4.3. Values reported in table 4.3 suggest that a higher potential barrier during the voltage pulse leads to a lower density of injected electrons per unit volume, while the height of the barrier before the pulse does not seem to be relevant. It can be assumed that injection of electrons inside the silicon bulk from the N-type doped injector occurs mainly through thermionic emission. To show this, a new series of simulations is performed, whose results are showed in figure 4.5a, and then compared with the analytical formula for thermionic emission, in equation (4.1) [83]:

$$J = A^* T^2 \exp\left(\frac{-\Phi_B}{kT}\right) \tag{4.1}$$
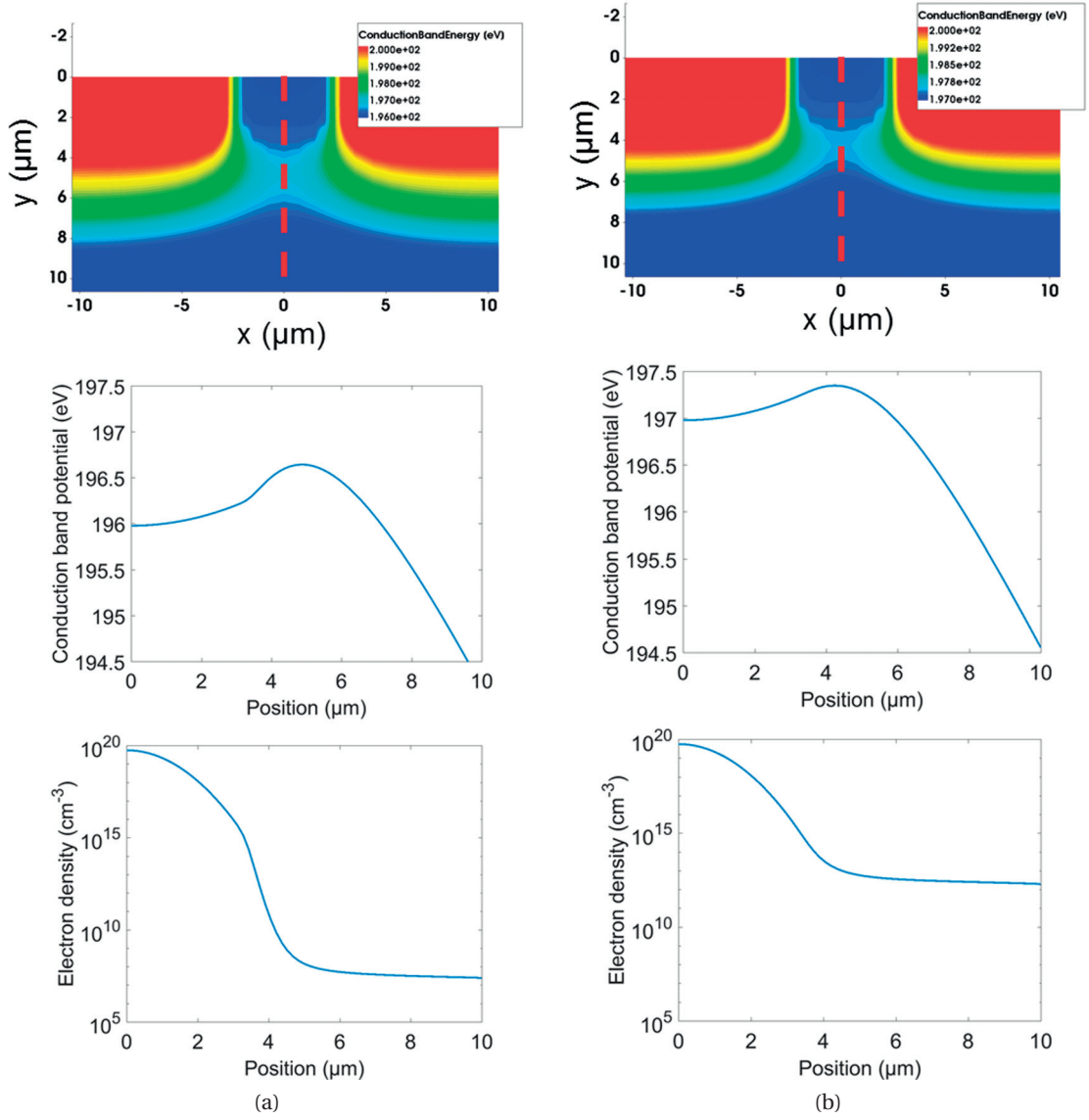
Figure 4.3 – Plots of the conduction band edge potential and injected electron density (a) before the voltage injection pulse and (b) during the pulse. The voltage applied to the p-type doped areas generates a barrier in front of the n-type doped well. When the voltage pulse is applied, the barrier is lowered and electrons can be injected inside the device bulk.
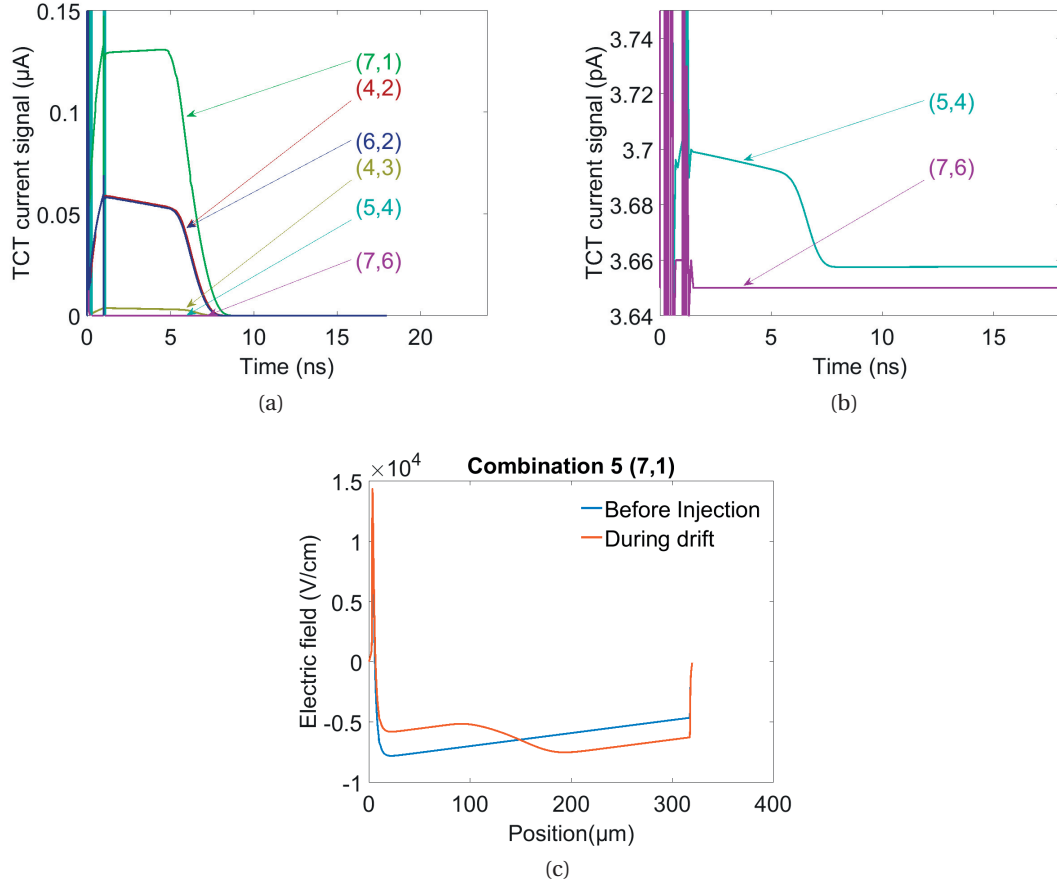
Figure 4.4 – (a,b) TCT signal currents of the first six combinations, in which the arrows show the combination of positive voltages $V_{bias,B}$ and $V_{trans,B}$, following this notation: ($V_{bias,B}$, $V_{trans,B}$), and (c) electric field profile in case of combination 5, before injection and during the drift.

Combination	$\mathbf{\Phi_{B,-t}}$ (eV)	$\mathbf{\Phi_{B,0}}$ (eV)	$\mathbf{Q_{in}}$ (C)
1	0.665	0.371	1.82×10^{-17}
2	1.086	0.665	2.64×10^{-20}
3	2.090	1.568	2.60×10^{-20}
4	0.665	0.315	2.94×10^{-16}
5	2.091	0.306	6.83×10^{-16}
6	1.568	0.315	2.90×10^{-16}

Table 4.3 – Comparison between injected electrons density and potential barrier height. $\Phi_{B,-t}$ is the potential barrier height before the voltage pulse, $\Phi_{B,0}$ is the potential barrier height during the pulse, at 0 ns, Q_{in} is the injected charge.

where J is the emission current density, k and A^* are the Boltzmann and Richardson constants, T is the temperature and Φ_B is the height of the potential barrier. If injection proceeds from thermionic emission, the current densities should scale exponentially with the values of the potential barriers. In figure 4.5a, it is possible to observe this behaviour. The same is observed for the analytical expression, shown in figure 4.5a. An important difference between the two curves for the highest value of the potential barrier is observed. In this case, the emission current should be smaller than the reverse bias current value obtained in TCAD simulations, which is the value shown in plot. The similar behaviour of the two currents

(a)   (b)
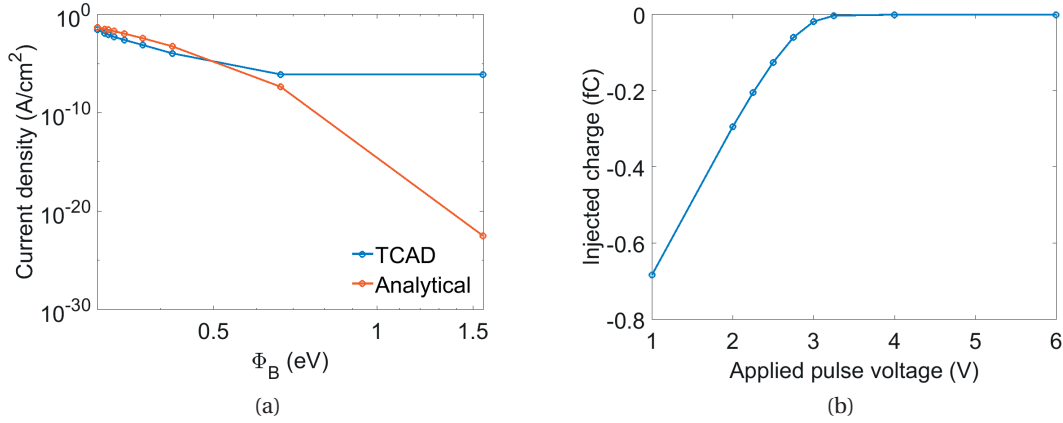
Figure 4.5 – (a) Comparison between TCAD and the thermionic emission formula of current densities, and (b) injection charge versus applied pulse voltage, i.e. the positive voltage applied to node B during the pulse.

supports the hypothesis that thermionic emission can describe the physical mechanism for charge injection. Figure 4.5b represents the dependence of the injected charge with respect to the pulse applied at node B (while voltage levels for nodes A and C are kept the same, respectively 0 V and +200 V). Since the barrier height at node B is not proportional to the applied voltage, the dependence of the injected charge density with voltage is not exponential.

4.2.2 Electrical versus optical excitation

The next step in the study of el-TCT is to perform a qualitative comparison between the TCT signals obtained with light and electrical excitation techniques on a standard diode and an el-TCT device. Except for the N-type injector implant, the simulated structures share the same technological parameters, therefore, in case of the diode the P-type doping is Gaussian. Concerning the simulation parameters, the voltage difference applied between opposite P-type and N-type doped layers (nodes C and A in figure 4.1a) is fixed to +200 V (positive on node C and 0 V on node A). Other parameters such as the voltage at node B and the parameters of light injection such as the pulse duration, the pulse bias and the intensity of light are listed in table 4.4. In case of el-TCT device, light is injected from the top, between the contacts A and B, to simulate the masking of the aluminium contacts. The pulse length is 1 ns. Note that these parameters are tuned to obtain concordance between transient current for optical and

Electrical injection			Light injection			
$V_{bias,C}$ (V)	$V_{bias,B}$ (V)	$V_{trans,B}$ (V)	λ_{LASER} (nm)	I (mW/cm^2)	t_{pulse} (ps)	V_{bulk} (V)
+200	+4	+3	660	1	50	+200

Table 4.4 – Parameters of simulations of el-TCT and light injection TCT. λ is the laser wavelength, I is the laser intensity, t_{pulse} is the pulse time width, V_{bulk} is the reverse bias voltage.

el-TCT as shown in Figure 4.6, which does not hamper the formal analysis. According to the

(a)

(b)
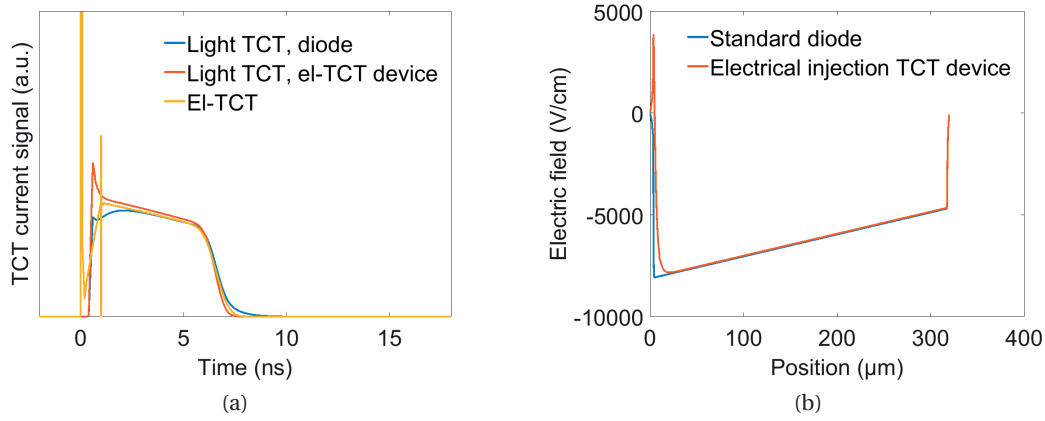
Figure 4.6 – Comparison between TCAD simulations of light injection TCT and el-TCT. The left plot (a) shows a comparison between light injection TCT on a standard diode and on a device for el-TCT, and electrical injection on an el-TCT device. The right plot (b) shows the profile of the Y component of the electric field at the centre of a standard diode compared to the one at the centre of an el-TCT device.

numerical simulations, removing the N-type injector does not affect the electric field profile inside the silicon bulk (see figure 4.6b, where the Y component of the electric field is taken at the centre of the devices), which is a prerequisite to compare both methods. In case of el-TCT, a positive electric field is observed from 0 to 5 μm. This is due to the doping of the N-type implant, and does not cause any hole accumulation since holes quickly recombine due to the high N-type doping of the injector. Similarly, the transient currents (see figure 4.6a) reveal that electrical and light injection TCT are consistent, providing evidence that the concept of el-TCT is meaningful. It is possible to observe peaks in case of light injection between 0 and 2 ns. They are due to the fact that holes are also generated and immediately collected in case of light injection. For electrical injection, only electrons are injected. Moreover, the curve corresponding to the light injection in the diode is smaller than the others between 0 and 2 ns. This is due to the Gaussian profile of the P-type doped silicon, which generates a slow increase of the electric field before the PN junction.

4.3 Devices and experimental characterization

4.3.1 Devices and measurement setup

Based on numerical simulations, a device was designed and fabricated at CMi, to demonstrate the proof of concept. The device consists of a matrix of N-type doped wells surrounded by a P-type doped silicon, which represent respectively contacts A and B in figure 4.1a. The substrate is a 4-inch N-type silicon wafer and constitutes the i region of the PiN diode. In order to achieve a large depletion region, the silicon wafer has a nominal resistivity greater than 5000 Ωcm, which corresponds to a doping concentration smaller than 10^{12} cm^{-3} (similar to the one used in TCAD simulations). The fabrication process flow is summarized in table 4.5, and the following machines and services have been used: ACS200 Gen3 for automatic coating and development, Heidelberg VPG200 for direct i-line (355-365 nm) laser writing lithography with 5 mm head, IBS (Ion Beam Service) for ion implantation, Tepla GIGAbatch for photoresist oxygen plasma stripping, Pfeiffer SPIDER600 for sputtering, SPTS APS dielectric etcher for dry etching of SiO2, Disco DAG810 for wafer grinding, Steag Mecapol E460 for chemical mechanical polishing (CMP), Centrotherm furnaces for POCl$_3$ doping, STS multiplex for Al dry etching, Alliance Concept DP650 for Al sputtering. At the end of the process, spreading resistance profiling (SRP) [88] measurements were performed, showing a bulk doping concentration of 3×10^{12} cm^{-3}. This difference from the nominal resistivity value before processing could be due to high temperature steps during the processing that can lead to thermal donor generation [67]. Figure 4.7 shows the top view and cross section of the designed diodes (figure 4.7a) as well as an optical microscope picture of the top of the fabricated devices (figure 4.7b). Different

n-type doped silicon
p-type doped silicon
Silicon dioxide
Aluminum
High resistivity silicon

n-type doped silicon
Aluminium
Silicon dioxide
Spacing between n and p-type doped silicon
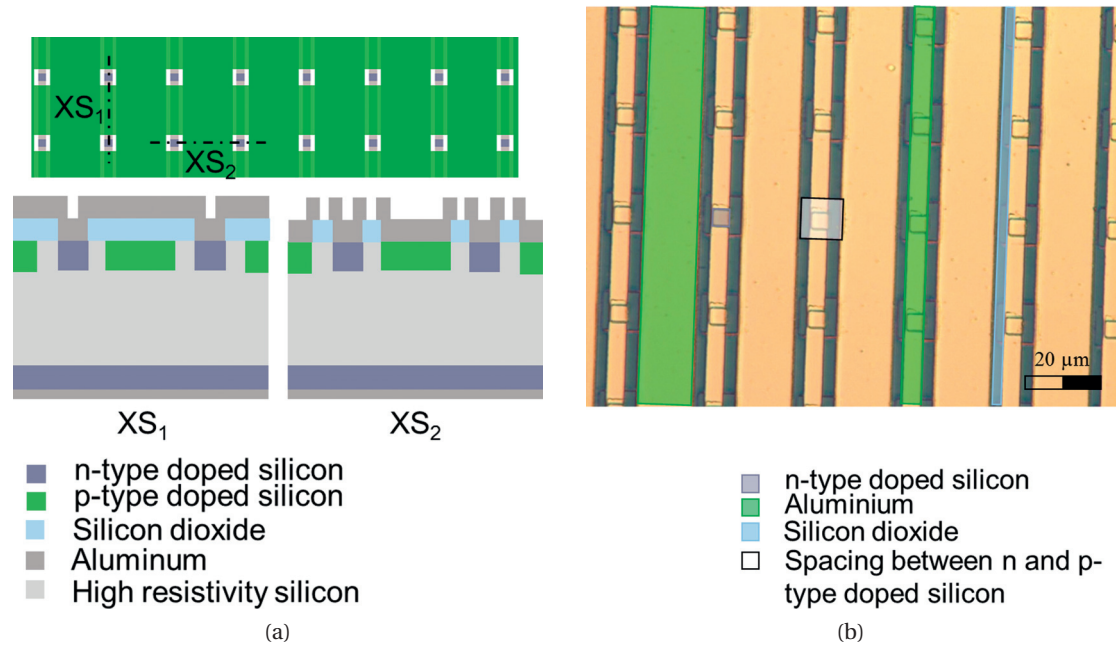
(a)   (b)

Figure 4.7 – (a) Top view of the layout and cross-sections in the vertical (XS$_1$) and horizontal (XS$_2$) directions and (b) optical microscope picture of the fabricated device top side.

Step	Process	Parameters
1	Photolithography	Photoresist: AZ ECI 3027, thickness 4 μm
2	Boron ion implantation	Dose 10^{15} cm^{-3}, Energy 30 keV
3	Photoresist stripping	First plasma oxygen, then remover microposit 1165
4	SiO$_2$ sputtering	Thickness 2 μm
5	Photolithography	Photoresist: AZ ECI 3007, thickness 1.5 μm
6	SiO$_2$ etching	Reactive ion etching
7	Photoresist stripping	First plasma oxygen, then remover microposit 1165
8	Phosphorus ion implantation	Dose 10^{16} cm$_{-3}$, Energy 30 keV
9	Photoresist coating	Photoresist: AZ ECI 3027, thickness 4 μm
10	Back side wafer thinning	Grinding and CMP, final thickness 320 μm
11	Photoresist stripping	Remover microposit 1165
12	SiO$_2$ etching	BHF diluted in water 7:1
13	SiO$_2$ sputtering	Thickness 2 μm
14	Phosphorus doping	Furnace with POCl$_3$ atmosphere during 15 min at 1100°C
15	SiO$_2$ etching	BHF diluted in water 7:1
16	SiO$_2$ sputtering	Thickness 400 nm
17	Photolithography	Photoresist: AZ ECI 3007, thickness 1.5 μm
18	SiO$_2$ etching	Reactive ion etching
19	Photoresist stripping	First plasma oxygen, then remover microposit 1165
20	Al with 1% of Si sputtering	Thickness 300 nm
21	Photolithography	Photoresist: AZ ECI 3007, thickness 1.5 μm
22	Al with 1% of Si etching	Reactive ion etching
23	Photoresist stripping	First plasma oxygen, then remover microposit 1165
24	Photolithography	Photoresist: AZ ECI 3027, thickness 4 μm
25	Al with 1% of Si sputtering	Thickness 300 nm
26	Photoresist stripping	Remover microposit 1165
27	Dicing	

Table 4.5 – Process flow for the fabrication of devices for el-TCT.

versions of the read-out circuit have been developed before the final configuration. First, the signal generator Picosecond Pulse Labs (model 10,050A) was used for the generation of the nanosecond voltage pulse, that needed to be attenuated, since it is positive, fixed at +10 V of amplitude, too much for experiments on electrical injection (attenuators were added to reduce the pulse amplitude). This pulse was applied directly to the node A, while node B was connected to ground (see figure 4.1a for references). This was to apply a forward bias for the lateral junction only during the pulse, to emulate the configuration of simulations. The signal was recorded through the oscilloscope Agilent DSO9254A from the node C (see figure 4.1a), using a bias-tee Picosecond Pulse Labs model 5531, useful to apply also the bias voltage to the same contact using a Keithley 2410 voltage generator . This first simple configuration had the drawback that there was not a reverse bias configuration of the lateral junction when the pulse was not applied, and that the pulse was applied to the A node instead of the B node (as in simulations). To obtain a configuration closer to the one simulated with

TCAD, a signal inverter was applied to the output of the pulse generator, the Phillips Scientific model 460. In this case, the pulse was applied to the N-type doped injectors, while the P-type doped contact was connected to ground. Also in this case, measurements were not the same as the simulations. The last step was the addition of a second bias-tee, the Mini-Circuits ZFBT-6GW, to add a bias to the applied pulse connected to the N-type doped contact. The final configuration of the circuit used for the el-TCT measurements is shown in figure 4.8. Concerning the device, the Bulk contact represents the contact to the strongly doped N-type back implant (node C in figure 4.1a), the N-type contact represents the N-type doped well (node B in figure 4.1a) and the P-type contact represents the P-type doped silicon (node A in figure 4.1a). In case of light injection, a 50 ps pulse laser (wavelength 660 nm), with a spot
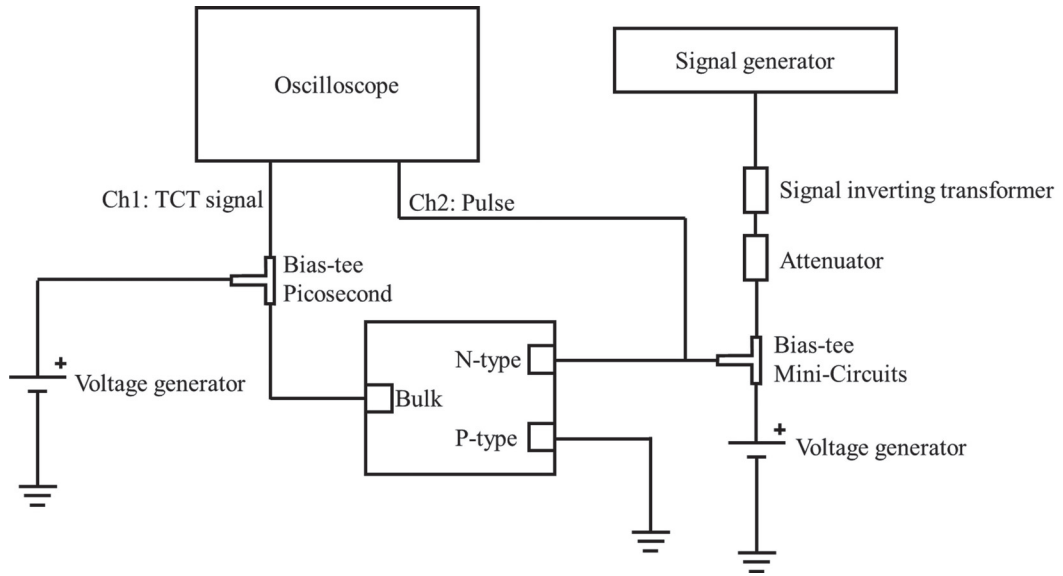
Figure 4.8 – Schematic of the circuit used for measurements.

diameter of 10 μm positioned in the middle of the device (i.e. shining on the centre of the n-type wells matrix shown in Figure 4.7b). The N-type contact is biased at a value close to the offset voltage used for electrical injection (+4.1 V), and the TCT signal is amplified using the CIVIDEC C2HV Broadband Amplifier (gain 40 dB, bandwidth 2 GHz), connected on the back side of the device. The measured capacitance of the device is 3.54 pF at 100V, 3.04 pF at 120V and 2.64 pF at 140V.

4.4   Transient current measurements and analysis

The electrical pulse that is applied to the N-type doped well (node B in figure 4.1a) is shown in figure 4.9a. The overall pulse duration is about 1 ns during which the voltage changes abruptly from +3.75 V to +0.2 V. The transient current generated by the drift of the injected carriers is shown in figure 4.9b for different back side voltages. It is possible to observe a small distortion at 12 ns. This is due to a parasitic signal inside the circuit for voltage pulse generation, since it is possible to observe the same feature on the injection pulse in figure 4.9a. Another parasitic pulse is observed at 25 ns, which however is out of the time window of interest for the TCT

measurement in figure 4.9b. Increasing the voltage between nodes A and C (V_{AC}) modifies the shape of the transient current. Up to 2 ns after the electrical pulse, the current increases. This could be due to the increase in the electric field in the lightly doped region, as observed in the TCAD simulations of optical TCT on standard diode in figure 4.9b, but also due to the finite rise time of the read-out circuit. After 10 ns, it is possible to observe a signal that fades, since the device is not fully depleted. In order to compare el-TCT with light induced TCT, the normalized transient currents obtained from both methods are shown in Figure 4.9b (V_{AC} are listed in the legend for different measurements), where the reverse PiN diode biases are kept the same for optical and electrical injection methods. The normalization has been performed by introducing a constant U (the same for all measurements), according to $i(t)_{el-TCT} = U i(t)_{light\ injection}$. Both methods lead to similar shapes of TCT curves (in both
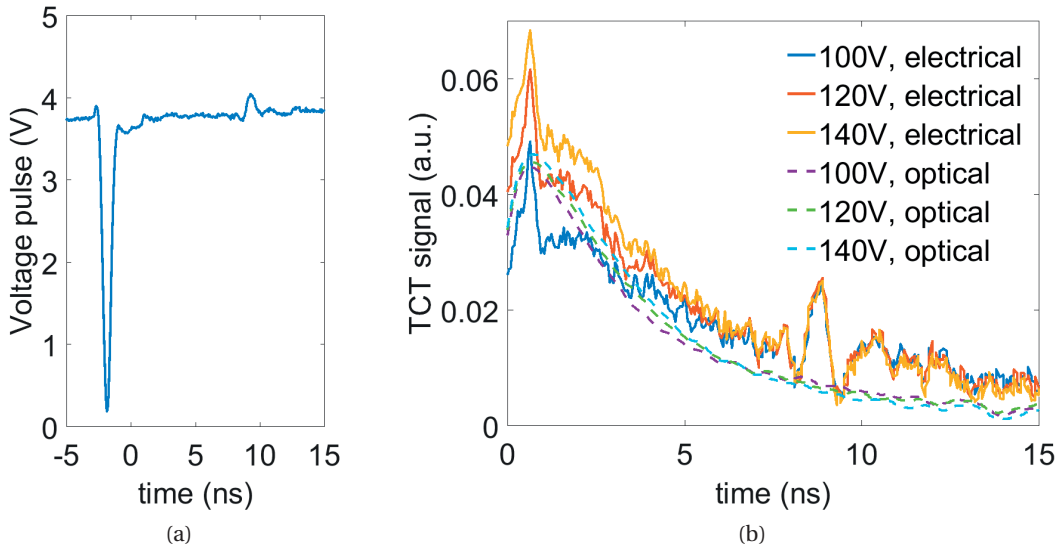

Figure 4.9 – (a) Voltage pulse applied to the n-type doped wells with positive sign and (b) comparison between TCT signals obtained by light and electrical injection.

cases the time between the rising and decaying of the currents is close to 10 ns), even if the difference between curves obtained from optical TCT is small (a similar behavior observed in TCAD simulations in figure 4.10b). This confirms that electrical and light injection methods yield equivalent results. The signal-to-noise ratio can be improved by using a dedicated board in which generation of the signal and readout are performed close to the device. A last validation of the el-TCT comes from TCAD simulations. A modified version of the structure presented in figure 4.1a (where the parameter S and the bulk doping profile are used as matching parameters, since the doping profile at the end of the fabrication process is different from the nominal one) was used to carry out numerical simulations of el-TCT. The best matching between TCAD and measurements was obtained for a bulk doping of 3×10^{12} cm^{-3} (as the one measured with SRP at the end of the process) and an S parameter equal to 0 μm (meaning that in this simulations the regions P_W and N_W are not spaced). In section 2.4.2,

the bulk doping concentration is found to be 1.3×10^{12} cm^{-3}. One explaination for the fact that this value is different with the one found in the present section is the slight difference in the doping profile between a standard diode and the device for el-TCT. A comparison between the simulated and the measured el-TCT signals is presented in figure 4.10a (see V_{AC} in the legend). An overall agreement with experiments can be observed for light injection TCT in Figure 4.10b. This supports the hypothesis that the signal measured after electrical injection
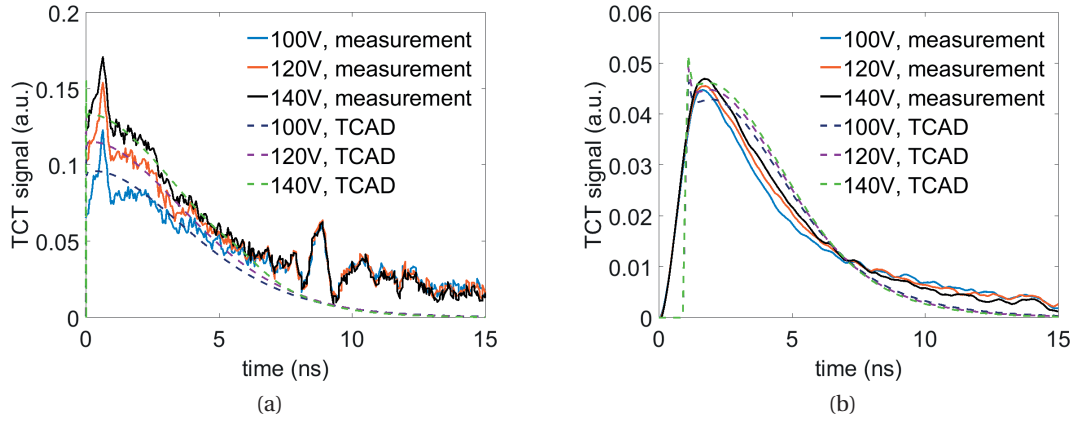

Figure 4.10 – Comparison between TCAD simulations and experimental data of TCT signals obtained by electrical (a) and light (b) injection.

can be attributed to the drift of the electrons injected in the low doped silicon. The injected charge can be controlled by the voltage applied to the N-type doped wells and observed as integral of transient current in time-induced charge. This analysis has been carried out both for experimental data and TCAD simulations. The results presented in figure 4.11 (the value of the peak voltage is the absolute value) reveal a dependence on the $V_{trans,B}$, similar to the behaviour shown in figure 4.5b.

4.5 Conclusions

A new method of carrier injection for TCT characterization, called el-TCT and relying on the concept of electrical charge injection in PiN diodes has been proposed, simulated with TCAD and demonstrated experimentally. The fabricated device structures for el-TCT validated the feasibility to use the electrical charge injection method for device characterization. This new concept allows the integration of a charge injection mechanism into an operational device like photon or particle detectors. Such modified devices no longer need complex external excitation sources (alpha particles, lasers, etc.) to perform TCT. The co-integration of el-TCT with active sensors, where injection and detection can be implemented concurrently, should pave the way to in-situ characterization of solid-state particle or photon detectors. To reduce the costs, and to simplify the fabrication process, a different design of el-TCT devices can be implemented, with the use of Schottky junctions instead of PN junctions (Schottky diodes do not require implantation steps). In this case, the device structure would be different, as
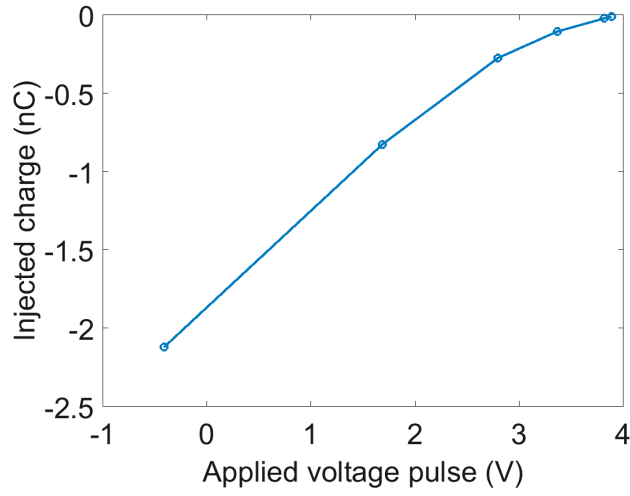
Figure 4.11 – Measured injected charge as a function the voltage applied to node B during the pulse.

Sch_W (μm)	N_W (μm)	S (μm)	Th (μm)	$V_{bias,B}$ (V)	$V_{trans,B}$ (V)	$V_{bias,A}$ (V)	$V_{bias,C}$ (V)
7	3	2	320	+4	+3	0	+200

Table 4.6 – Simulations parameters for el-TCT with Schottky junctions.

shown in figure 4.12. The working principle is the same of PN junction devices, where the Schottky junction has the same role of the P-type doped contact of the diode. The biasing configuration and voltage pulse for the use of this device are the same of the ones presented in figure 4.1b. TCAD simulations show that it is possible to obtain signals similar to PN junction el-TCT devices (figure 4.13), by using parameters in table 4.6, where the doping of silicon is 7×10^{11} cm^{-3}. Moreover, figure 4.14 shows that, during the voltage pulse, the conduction band changes, as in the case of PN junctions (see figure 4.3). The barrier is lowered, and it is restored to the starting value at the end of the pulse.
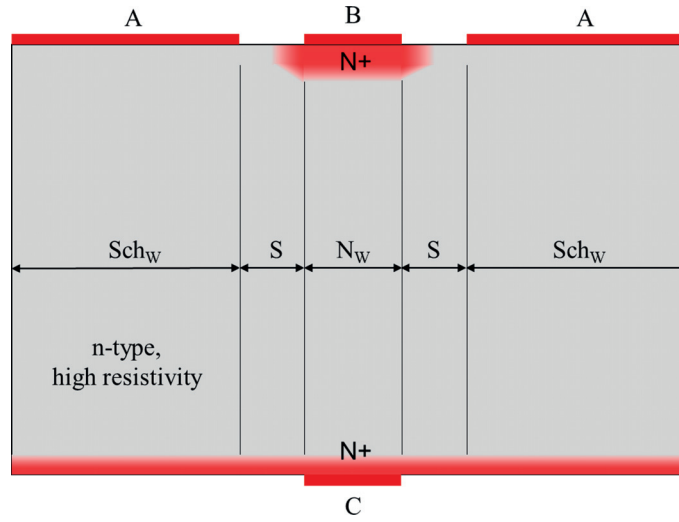
Figure 4.12 – Structure for el-TCT with Schottky junctions. Sch_W is the width of the Schottky contacts , N_W is the width of the N-type doped well, to obtain ohmic contact, S is the spacing between Schottky junctions and ohmic contact.
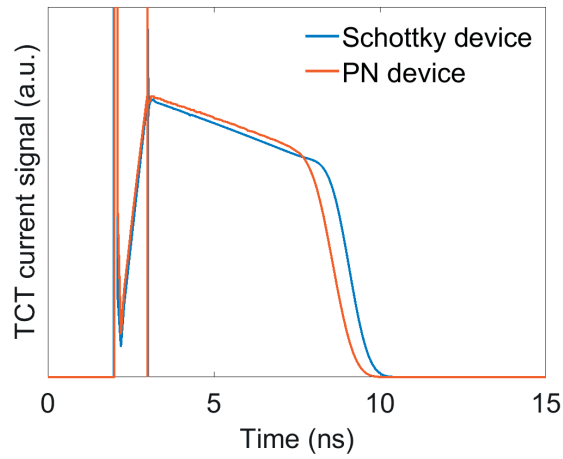
Figure 4.13 – TCT signal obtained by el-TCT with Schottky junctions. Simulation parameters are listed in table 4.6.
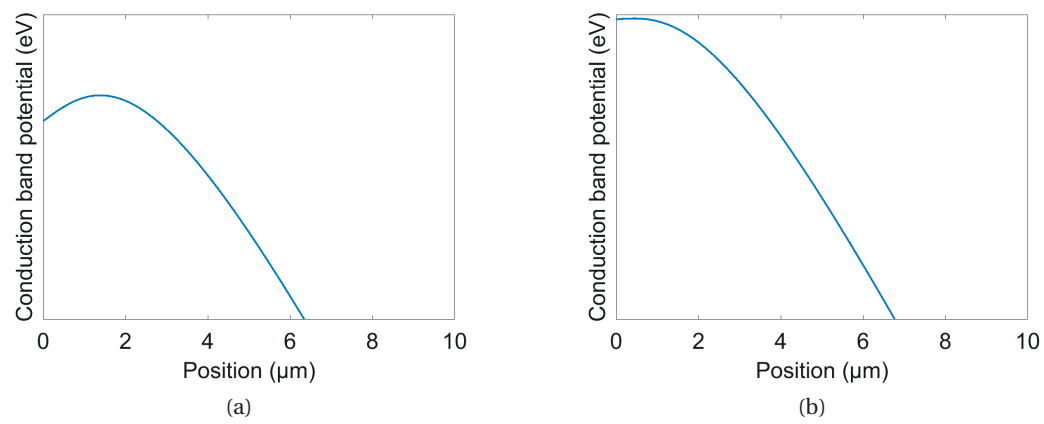
Figure 4.14 – Conduction band barrier (a) during and (b) after the voltage pulse, for Schottky el-TCT devices.

5 Conclusions and outlook

This thesis presents a new characterization method of electrical properties for thin bonding interfaces in silicon based on TCT. It has been developed for the evaluation of a novel CMOS-compatible bonding process for the fabrication of monolithic radiation detectors. Moreover, within this thesis, a new method for charge injection in TCT measurements, that relies on the application of voltage pulses instead of light pulses, was introduced. This approach could lead to new possibilities such as in-situ and online measurements.

An analytical study of a method for thin bonding interface characterization has been presented, showing that the analysis of a TCT signal can give information about the traps types and concentration inside it. As a result of this study, an analytical model has been developed, to perform fast analysis of TCT signals, without the use of complex simulation tools as Sentaurus TCAD. The characterization has been performed by TCT measurements of Schottky diodes, a simple and cheap method, since it requires to perform only the process itself on standard high resistivity wafers, and then to fabricate the diodes. Despite the simplicity of this method, it has been possible to understand the conduction properties of the interface, and to have a hint on the concentration of ionized traps. The results of this characterization indicate that the bonding interface blocks the passage of electrons clouds at low voltages, by considerably decreasing the intensity of the electric field in the region located in the bottom part of the diode. This could represent an important issue related to the fabrication of monolithic detectors, since the charge generated in the silicon bulk would not be collected by the read-out electronics. To solve this problem, two possible solutions have been identified: one is to optimize the bonding process, in order to reduce the number of traps at the interface (for instance by using different plasma sources), the other is to design the detector in such a way that the bonding interface is located at the PN junction.

In the second part of this work, a new method for charge injection through voltage pulses for TCT measurements has been demonstrated. The integration of devices for this purpose is based on standard CMOS-compatible processes, to introduce N-type doped wells (to which a nanosecond voltage pulse is applied) for charge injection in P-type doped contacts in PiN diodes. First TCAD numerical simulations have been carried out to study the principle and the feasibility of the charge injection. Results show good agreement between standard TCT, obtained by means of light injection with laser, and el-TCT, i.e. the transient current signals are similar in shape. Moreover, what observed is that the electric field shape in the bulk is not

influenced by the presence of N-wells. After this study, fabrication has been performed at CMi, obtaining devices that have been measured at the SSD group of CERN. Experimental results confirmed what was obtained by simulations, giving a proof of principle of el-TCT.

Outlook

If implemented in the same silicon substrate of radiation detectors, el-TCT devices would introduce a new tool for the study of radiation damage during the sensor lifetime. Since the measurements need only electrical connections between the device and the setup (composed of a pulse generator and an oscilloscope), that could be placed on the same support of radiation detectors, there would be no need of dismounting them from the experiment to perform TCT measurements. This characteristic could be used also to study the electric field in silicon during irradiation tests, without pausing them to extract the detector from the setup.

It has been demonstrated that CMOS-compatible SAB, together with design solutions, can be used to fabricate radiation detectors. Instead of using high resistivity silicon as sensing bulk, other materials could be used, such as Germanium, in which charge carriers mobility is higher than in silicon [89]. This would help, since the diffusion would be faster, that is positive for charge collection in radiation detectors, as seen in section 1.2.2. This process could be used not only for electrical connection between two substrates, but also to fabricate microchannels for electronics cooling. Indeed, mechanical strength has been demonstrated to be high [58], and therefore, a silicon substrate on which microchannels have been etched could be bonded on a CMOS wafer. In this case, the cooling would be optimal, since both the channels and the electronics share the same bulk.

Bibliography

[1] The hystory of CERN. https://timeline.web.cern.ch/timelines/The-history-of-CERN.

[2] The accelerator complex. https://home.cern/about/accelerators.

[3] L. Evans and P. Bryant. LHC Machine. *Journal of Instrumentation*, 2008.

[4] CMS Collaboration. The CMS experiment at the CERN LHC. *Journal of Instrumentation*, 2008.

[5] The ATLAS Collaboration. The ATLAS Experiment at the CERN Large Hadron Collider. *Journal of Instrumentation*, 2008.

[6] ALICE. https://home.cern/about/experiments/alice.

[7] The ALICE Collaboration. The ALICE experiment at the CERN LHC. *Journal of Instrumentation*, 2008.

[8] LHCb Large Hadron Collider beauty experiment. http://lhcb-public.web.cern.ch/lhcb-public/.

[9] The LHCb Collaboration. The LHCb Detector at the LHC. *Journal of Instrumentation*, 2008.

[10] The CERN Large Hadron Collider: Accelerator and Experiments. https://jinst.sissa.it/lhc/.

[11] CERN cds. https://cds.cern.ch/record/1463546.

[12] ALICE experiment. http://aliceinfo.cern.ch/Public/en/Chapter2/Chap2_DAQ.html.

[13] J. Willem van Hoorne. *Study and Development of a novel Silicon Pixel Detector for the Upgrade of the ALICE Inner Tracking System*. PhD thesis, Technische Universität Wien, 2015.

[14] The origins of the Brout-Englert-Higgs mechanism. https://home.cern/topics/higgs-boson/origins-brout-englert-higgs-mechanism.

[15] G. F. Knoll. *Radiation Detection and Measurement Third Edition*. John Wiley & Sons, Inc., 2000.

Bibliography

[16] Yu. K. Akimov. Silicon radiation detectors (Review). *Instruments and Experimental Techniques*, 50(1):1–28, 2007.

[17] G. Dearnaley and D.C. Northrop. *Semiconductor counters for nuclear radiations.* Wiley, 1963.

[18] J.-L. Autran and D. Munteanu. *Soft Errors from particles to circuit.* CRC Press, 2015.

[19] K. Nakamura et al. Review of particle physics. *Journal of Physics G: Nuclear and Particle Physics*, 37(7 A), 2010.

[20] A. Holmes-Siedle and L. Adams. *Handbook of Radiation Effects.* Oxford science publications. OUP Oxford, 2002.

[21] S. J. Watts et al. A new model for generation-recombination in silicon depletion regions after neutron irradiation. *IEEE Transactions on Nuclear Science*, 43(6):2587–2594, 1996.

[22] K. L. Brower. EPR of a (001) Si interstitial complex in irradiated silicon. *Physical review B*, 14(3):872–883, 1976.

[23] V. Eremin, E. Verbitskaya, and Z. Li. The origin of double peak electric field distribution in heavily irradiated silicon detectors. *Nuclear Instruments and Methods in Physics Research, Section A: Accelerators, Spectrometers, Detectors and Associated Equipment*, 476(3):556–564, 2002.

[24] T. H. Ning. High-field capture of electrons by Coulomb-attractive centers in silicon dioxide. *Journal of Applied Physics*, 47(7):3203–3208, 1976.

[25] N. Wermes. Pixel detectors for particle physics and imaging applications. *Nuclear Instruments and Methods in Physics Research, Section A: Accelerators, Spectrometers, Detectors and Associated Equipment*, 512(1-2):277–288, 2003.

[26] N. Wermes. Pixel detectors for tracking and their spin-off in imaging applications. *Nuclear Instruments and Methods in Physics Research, Section A: Accelerators, Spectrometers, Detectors and Associated Equipment*, 541:150–165, 2005.

[27] L. Rossi, P. Fischer, T. Rohe, and N. Wermes. *Pixel Detectors: From Fundamentals to Applications.* Particle Acceleration and Detection. Springer Berlin Heidelberg, 2006.

[28] M. Moll. Displacement Damage in Silicon Detectors for High Energy Physics. *IEEE Transactions on Nuclear Science*, pages 1–1, 2018.

[29] W. Snoeys. Monolithic pixel detectors for high energy physics. *Nuclear Instruments and Methods in Physics Research, Section A: Accelerators, Spectrometers, Detectors and Associated Equipment*, 731:125–130, 2013.

[30] P. Riedler. Monolithic silicon pixel sensors and technology challenges of the ALICE ITS. In *PH-DT Training Seminars*, CERN, 2015.

[31] E. H.M. Heijne et al. First operation of a 72 k element hybrid silicon micropattern pixel detector array. *Nuclear Inst. and Methods in Physics Research, A*, 349(1):138–155, 1994.

[32] I. Perić. A novel monolithic pixel detector implemented in high-voltage CMOS technology. *IEEE Nuclear Science Symposium Conference Record*, 2:1033–1039, 2007.

[33] I. Perić et al. Status of HVCMOS developments for ATLAS. *Journal of Instrumentation*, 12(2), 2017.

[34] M. Novelli et al. Semiconductor pixel detectors for digital mammography. *Nuclear Instruments and Methods in Physics Research, Section A: Accelerators, Spectrometers, Detectors and Associated Equipment*, 509(1-3):283–289, 2003.

[35] G. Mettivier, M. C. Montesi, and P. Russo. Digital autoradiography with a medipix2 hybrid silicon pixel detector. *IEEE Transactions on Nuclear Science*, 52(1):46–50, 2005.

[36] J. Ulrici et al. Imaging performance of a DEPFET pixel Bioscope system in Tritium autora-diography. *Nuclear Instruments and Methods in Physics Research, Section A: Accelerators, Spectrometers, Detectors and Associated Equipment*, 547(2-3):424–436, 2005.

[37] G. Claus et al. Particle tracking using CMOS monolithic active pixel sensor. *Nuclear.Instruments.and Methods in Physics.Research, Section.A: Accelerators., Spectrometers., Detectors.and Associated.Equipment.*, 465(1):120–124, 2001.

[38] A. Dorokhov et al. High resistivity CMOS pixel sensors and their application to the STAR PXL detector. *Nuclear Instruments and Methods in Physics Research, Section A: Accelerators, Spectrometers, Detectors and Associated Equipment*, 650(1):174–177, 2011.

[39] B. Abelev et al. (ALICE). Technical Design Report for the Upgrade of the ALICE Inner Tracking System. *Tech. Rep. CERN-LHCC-2013-024*, ALICE-TDR-017, 2014.

[40] W. Snoeys et al. A process modification for CMOS monolithic active pixel sensors for enhanced depletion, timing performance and radiation tolerance. *Nuclear Inst. and Methods in Physics Research, A*, 871(June):90–96, 2017.

[41] J. Willem van Hoorne et al. The investigator - an efficient tool to optmize design parameters of a CMOS pixel sensor. *IEEE NSS/MIC 2016 conference*, 2016.

[42] W. M. Haynes. *CRC Handbook of Chemistry and Physics*. CRC Press, 96 edition, 2016.

[43] C. Harendt, H. G. Graf, B. Hofflinger, and E. Penteker. Silicon fusion bonding and its characterization. *Journal of Micromechanics and Microengineering*, 2(3):113–116, 1992.

[44] V. Masteika, J. Kowal, N. S. J. Braithwaite, and T. Rogers. A Review of Hydrophilic Silicon Wafer Bonding. *ECS Journal of Solid State Science and Technology*, 3(4):Q42–Q54, 2014.

[45] Q. Y. Tong, E. Schmidt, U. Gösele, and M. Reiche. Hydrophobic silicon wafer bonding. *Applied Physics Letters*, 64(5):625–627, 1994.

[46] K. Ljungberg, A. Söderbärg, and Y. Bäcklund. Spontaneous bonding of hydrophobic silicon surfaces. *Applied Physics Letters*, 62(12):1362–1364, 1993.

[47] P. Ramm, J.-Q. J. Lu, and M. M. V. Taklo. *Handbook of wafer bonding*. WILEY-VCH, 2012.

[48] Q. Y. Tong, G. Cha, R. Gafiteanu, and U. Gösele. Low Temperature Wafer Direct Bonding. *Journal of Microelectromechanical Systems*, 3(1):29–35, 1994.

[49] S. N. Farrens, J. R. Dekker, J. K. Smith, and B. E. Roberds. Chemical Free Room Temperature Wafer To Wafer Direct Bonding. *Journal of The Electrochemical Society*, 142(11):3949–3955, 1995.

[50] H. J. Quenzer and W. Benecke. Low-Temperature Silicon Wafer Bonding. *Sensors and Actuators A*, 32:340–344, 1992.

[51] R.F. Wolffenbuttel. Low-temperature intermediate Au-Si wafer bonding; eutectic or silicide bond. *Sensors and Actuators A*, 62:680–686, 1997.

[52] R. F. Wolffenbuttel and K. D. Wise. Low-temperature silicon wafer-to-wafer bonding using gold at eutectic temperature. *Sensors and Actuators: A. Physical*, 43(1-3):223–229, 1994.

[53] C. B. Collins, R. O. Carlson, and C. J. Gallagher. Properties of gold-doped silicon. *Physical Review*, 105(4):1168–1173, 1957.

[54] D. Haneman, W. D. Roots, and J. T. P. Grant. Atomic mating of germanium surfaces. *Journal of Applied Physics*, 38(5):2203–2212, 1967.

[55] U. Gösele et al. Self-propagating room-temperature silicon wafer bonding in ultrahigh vacuum. *Applied Physics Letters*, 67(1995):3614, 1995.

[56] T. Suga et al. Structure of Al-Al and Al-Si3N4 interfaces bonded at room temperature by means of the surface activation method. *Acta metall. mater.*, 40:133–137, 1992.

[57] H. Takagi et al. Surface activated bonding of silicon wafers at room temperature. *Applied Physics Letters*, 68(16):2222–2224, 1996.

[58] C. Flötgen, N. Razek, V. Dragoi, and M. Wimplinger. Novel Surface Preparation Methods for Covalent and Conductive Bonded Interfaces Fabrication. *ECS Transactions*, 64(5):103–110, 2014.

[59] J. Burggraf, J. Bravin, H. Wiesbauer, and V. Dragoi. Monolithic thin wafer stacking using low temperture direct bonding. *ECS Transactions*, 64(5):95–101, 2014.

[60] V. Eremin, N. Strokan, E. Verbitskaya, and Z. Li. Development of transient current and charge techniques for the measurement of effective net concentration of ionized charges (Neff) in the space charge region of p-n junction detectors. *Nuclear Instruments and Methods in Physics Research, Section A: Accelerators, Spectrometers, Detectors and Associated Equipment*, 372(3):388–398, 1996.

[61] G. Kramberger et al. Investigation of irradiated silicon detectors by edge-TCT. *IEEE Transactions on Nuclear Science*, 57(4):2294–2302, 2010.

[62] M. F. García et al. High-resolution three-dimensional imaging of a depleted CMOS sensor using an edge Transient Current Technique based on the Two Photon Absorption process (TPA-eTCT). *Nuclear Instruments and Methods in Physics Research Section A: Accelerators, Spectrometers, Detectors and Associated Equipment*, In press:1–3, 2016.

[63] A. A. Quaranta et al. On the information available from the rise-time of the charge pulse supplied by semiconductor particle detectors. *Nuclear Instruments and Methods*, 35:93–99, 1965.

[64] B. L. Cohen and C. L. Fink. Pulse shapes in surface barrier detectors. *Nuclear Instruments and Methods*, 57:93–99, 1967.

[65] K. R. Zanio, W. M. Akutagawa, and R. Kikuchi. Transient currents in semi-insulating cdte characteristic of deep traps. *Journal of Applied Physics*, 39(6):2818–2828, 1968.

[66] H. W. Kraner, Z. Li, and E. Fretwurst. The use of the signal current pulse shape to study the internal electric field profile and trapping effects in neutron damaged silicon detectors. *Nuclear Inst. and Methods in Physics Research, A*, 326(1-2):350–356, 1993.

[67] M. Bruzzi et al. Thermal donors formation via isothermal annealing in magnetic Czochralski high resistivity silicon. *Journal of Applied Physics*, 99(9):1–8, 2006.

[68] T. Wang et al. Characterization of Various Stress-Induced Oxide Traps in MOSFET ' s by Using a Novel Transient Current Technique. *IEEE Transactions on Electron Devices*, 45(8):1791–1796, 1998.

[69] C. Schinke et al. Uncertainty analysis for the coefficient of band-to-band absorption of crystalline silicon. *AIP Advances*, 5(6), 2015.

[70] I. Mandić et al. Edge-TCT measurements with the laser beam directed parallel to the strips. *Journal of Instrumentation*, 10(8), 2015.

[71] A. Gorišek et al. The edge transient-current technique (E-TCT) with high energy hadron beam. *Nuclear Instruments and Methods in Physics Research, Section A: Accelerators, Spectrometers, Detectors and Associated Equipment*, 831:250–253, 2016.

[72] E. W. Van Stryland et al. Two Photon Absorption, Nonlinear Refraction, And Optical Limiting In Semiconductors. *Optical Engineering*, 24(4):244613–244613–, 1985.

[73] M. Göppert-Mayer. Elementary processes with two quantum transitions. *Annalen der Physik (Leipzig)*, 18(7-8):466–479, 2009.

[74] D. McMorrow et al. Subbandgap laser-induced single event effects: Carrier generation via two-photon absorption. *IEEE Trans. Nucl. Sci.*, 49(6):3002–3008, 2002.

Bibliography

[75] Synopsys. *TCAD Sentaurus.* I-2013.12 edition, 2013.

[76] W. R. Fahrner and S. Löffler. Determination of the Trap Density in Amorphous Silicon by Quasi-Static Capacitance-Voltage Measurements. *Journal of The Electrochemical Society,* 145(5):1786–1790, 1998.

[77] R. Eber. *Investigations of new Sensor Designs and Development of an effective Radiation Damage Model for the Simulation of highly irradiated Silicon Particle Detectors.* PhD thesis, Karlsruher Institut für Technologie, 2013.

[78] J. Fink, H. Krüger, P. Lodomez, and N. Wermes. Characterization of charge collection in CdTe and CZT using the transient current technique. *Nuclear Instruments and Methods in Physics Research, Section A: Accelerators, Spectrometers, Detectors and Associated Equipment,* 560(2):435–443, 2006.

[79] M. Moll. *Radiation Damage in Silicon Detectors.* PhD thesis, Universität Hamburg, 1999.

[80] W. Shockley and W. T. Read. Statistics of the Recombination of Holes and Electrons. *Physical Review,* 87(5):835–842, 1952.

[81] G. Lutz. Effects of deep level defects in semiconductor detectors. *Nuclear Instruments and Methods in Physics Research, Section A,* 377:234–243, 1996.

[82] G. Sasso, N. Rinaldi, G. Matz, and C. Jungemann. Analytical models of effective DOS, saturation velocity and high-field mobility for SiGe HBTs numerical simulation. *International Conference on Simulation of Semiconductor Processes and Devices, SISPAD,* (5):279–282, 2010.

[83] S. M. Sze. Wiley, 2nd edition, 1981.

[84] A. G. Bates and M. Moll. A comparison between irradiated magnetic Czochralski and float zone silicon detectors using the transient current technique. *Nuclear Instruments and Methods in Physics Research, Section A,* 555:113–124, 2005.

[85] P. E. Ciddor. Refractive index of air: new equations for the visible and near infrared. *Applied Optics,* 35(9):1566, 1996.

[86] M. A. Green. Solar Energy Materials & Solar Cells Self-consistent optical parameters of intrinsic silicon at 300 K including temperature coefficients. *Solar Energy Materials & Solar Cells,* 92:1305–1310, 2008.

[87] S. Ramo. Currents Induced by Electron Motion. *Proceedings of the I.R.E.,* 27(9):584–585, 1939.

[88] T. Bergauer et al. Measuring doping profiles of silicon detectors with a custom-designed probe station. *JINST,* 7:1–10, 2012.

[89] O. Madelung, U. Rössler, and M. Schulz, editors. *Germanium (Ge), electron mobility*, pages 1–17. Springer Berlin Heidelberg, Berlin, Heidelberg, 2002.

[90] G-ray. https://www.g-ray.ch/.

A INVESTIGATOR chips fabricated by CMOS-compatible SAB

In this appendix, a method for the characterization of bonding interfaces based on the use of INVESTIGATOR chip developed for the upgrade of the ALICE ITS. This work has been performed using the INVESTIGATOR measurements setup of the ALICE ITS group at CERN. Informations about the INVESTIGATOR chip, designed by this group, are based on the work of Jacobus Willem Van Hoorne [13]. Measurements have been carried out in collaboration with Qasim Malik.

A.1 INVESTIGATOR chip from ALICE ITS upgrade

The INVESTIGATOR chip has been designed to allow the study of the influence of different layouts parameters on the particle detection performance of MAPS for the ALICE ITS upgrade. It is composed by a sensitive layer with P-type epitaxial silicon (resistivity higher than 1000 Ω cm) deposited on a low resistivity silicon bulk. It is divided in different mini-matrices (MM) of 8 pixels per edge, each of them with different dimensions. Each pixel is composed of one N-well surrounded by a P-well, and it is reversely biased (with a back bias voltage V_{bb}), to obtain a depletion region extending from the N-well into the epitaxial layer. The cross section of the chip is shown in figure A.1, where layout parameters under study are marked. Measurements to analyze the influence of different layout parameters are usually performed by irradiating the chip with X-rays from a ^{55}Fe source and electrons from a ^{90}Sr source (radiation is applied from the front side, where CMOS circuitry is present). The charge generated inside silicon by radiation can be collected in two different ways: by drift, when the charge is located inside the depletion region of the N-well of the pixel, and by diffusion, when the charge is generated outside the depletion region. If diffusing charges reach the low resistivity bulk, they are reflected into the epitaxial silicon. In case of diffusion, charges generated by the passage of a radiation particle (called event) can reach more than one N-well, and therefore they can be collected by more than one pixel. The read-out relies on a voltage drop (V_{ev}) on the collection pixel due to the discharge of the pixel input capacitance (C_{px}) caused by the charge (Q_{ev}) collection (see equation (A.1)).

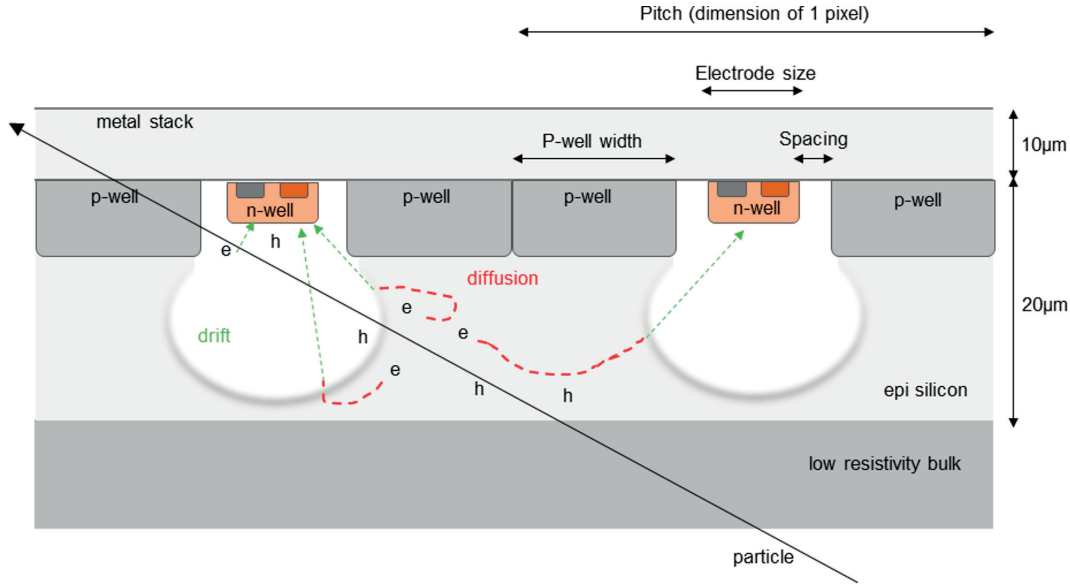$$V_{ev} = \frac{Q_{ev}}{C_{px}}$$ (A.1)

Figure A.1 – Cross section of two INVESTIGATOR pixels. The white regions are the depletion regions of pixels. Two different color are used to mark the drift and the diffusion paths, respectively green and red.

The following nomenclature is usually considered during measurements analysis: cluster (the group of pixels that collect charge from one event), cluster multiplicity (the number of pixels that compose a cluster. When higher than one, than more than one pixel collected charge in one event (charge sharing)), seed pixel (the pixel that collects the largest number of charges in one event). Signals from INVESTIGATOR measurements consist in the collection of number of events that occurs for each voltage drop caused by charge collection. The two most used radiation sources for INVESTGATOR testing are ^{55}Fe and ^{90}Sr. In measurements with the first one, an example of signal is shown in figure A.2. Fe55 sources generate X-rays with two different energies: 5.9 keV and 6.5 keV. The probability of having these energies are respectively 90% and 10%, with penetration profile inside silicon shown in figure A.3. From signal in figure A.2, it is possible to observe two peaks at high voltage values: these are the signals generated by events where the charge is entirely collected inside the depletion region of one pixel. The highest peak corresponds to the 5.9 keV photons (90% of probability), and therefore it can be used to calculate the number of electrons per mV of voltage drop ($V_{5.9}$), by following equation (A.2) and considering that this X-ray energy generates in average 1640 electrons.

$$n_{el/mV} = \frac{1640\ el}{V_{5.9}} \tag{A.2}$$

The part of signal at lower voltages is composed by events where charge sharing occurs. Measurements with ^{90}Sr sources give different signals. In this case, a continuous spectrum of electrons is generated, resulting in a typical signal that presents a Landau shape as the one shown in figure A.4. It is usually plotted as the number of events versus the number
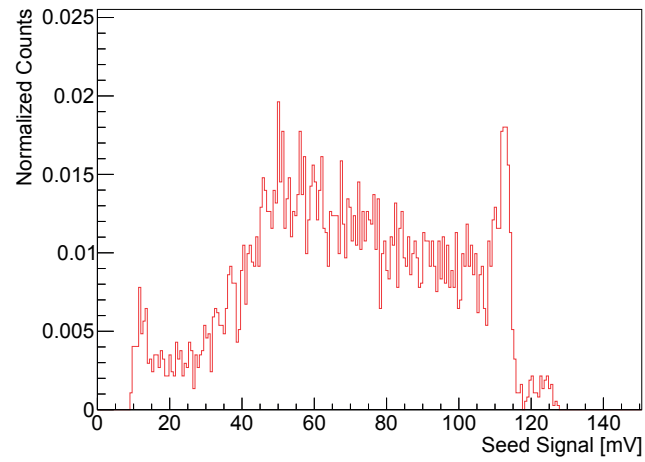
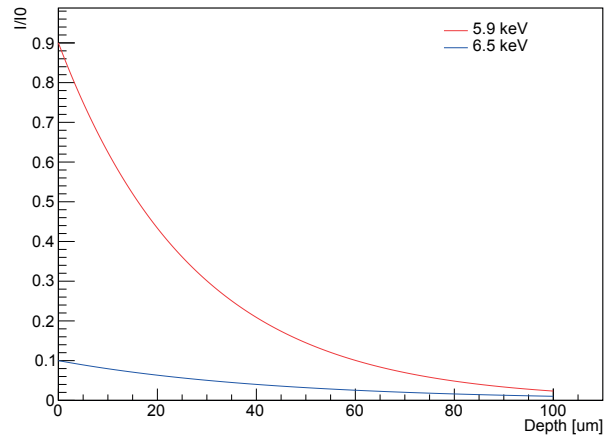Figure A.2 – Example of seed signal from ^{55}Fe measurements.

Figure A.3 – Intensity penetration profiles of X-rays in silicon. The intensity is plotted as the ratio between the actual and the starting value.

of generated electrons (that is calculated by considering the conversion value from ^{55}Fe measurements). Since the penetration length for electrons in this case is much higher than the
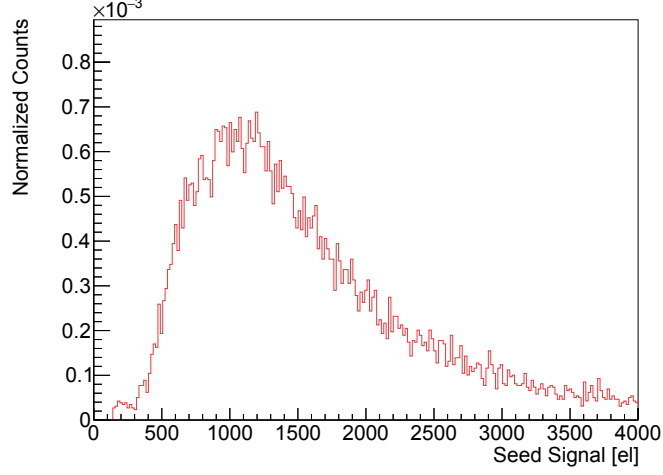

Figure A.4 – Example of seed signal from ^{90}Sr measurements.

pixel thickness, charge is considered to be generated linearly with the particle path length (60 electrons per µm in the case of these measurements). Therefore, the thickness of the sensitive region of the pixel t_{px} can be extracted by looking at the number of electrons with the highest number of events $n_{el,max}$ considering equation (A.3).

$$t_{px} = \frac{n_{el,max}}{60\ el/\mu m} \tag{A.3}$$

From these measurements, other parameters that can be extracted are the charge collection efficiency (the ratio between the detected charge and the total charge that is generated) and the relative depletion volume (the ratio between the depleted volume and the total volume). For more information about the INVESTIGATOR chip, it is possible to consult the PhD thesis of Jacobus Willem Van Hoorne [13].

A.2 INVESTIGATOR chip for bonding interface characterization

To characterize the bonding interface electrical properties with the INVESTIGATOR chip, it is necessary to modify its structure at the wafer level, by removing the low resistivity silicon part (this step reduces the thickness of this layer to 17 µm) and then by performing the CMOS compatible wafer bonding with a substrate, of different kinds: full thickness high resistivity silicon wafer (resistivity higher than 5000 Ω cm, 750 µm thick), thinned high resistivity silicon wafer (two different thicknesses have been tested: 55 µm and 90 µm), high resistivity epitaxial silicon wafers (whose properties are the same of the wafer on which the INVESTIGATOR chip has been fabricated). Fabrication of these chips has been performed by G-ray Switzerland [90]. For each case, measurements described in the previous section are performed, and results are shown in the following sections.

A.2.1   List of chips

Table A.1 shows the list of chips that have been provided by G-ray. The delivery number is listed in the chronological order of chips arrival at CERN. Table A.2 shows the list of mini-matrices

Delivery #	Chip ID	Batch #	Bonded substrate	Th (µm)
1	GRAY-1; GRAY-2; GRAY-3; GRAY-4; GRAY-5; GRAY-6	1	Resistivity > 5000 Ω cm	777
2	1C; 1E; 2B; 3B; 3F; 4F; 5C; 5D	1	Resistivity > 5000 Ω cm	777
3	GRAY-55um	2	Resistivity > 5000 Ω cm	55
3	GRAY-90um	2	Resistivity > 5000 Ω cm	90
4	GRAY-epi-1; GRAY-epi-2	3	Resistivity > 5000 Ω epitaxial 20 µm thick on low resistivity silicon	752

Table A.1 – List of chips provided by G-ray.

that have been measured, with the different dimensions corresponding to the ones in figure A.1.

MM	Pitch (µm)	Electrode size (µm)	Spacing (µm)	P-well width (µm)
26	20	3	3	5.5
27	20	3	4	4.5
28	20	3	5	3.5
90	28	5	3	8.5
4	20	3	5	3.5
110	30	2	3	11

Table A.2 – List of mini-matrices measured in this work, with the corresponding dimensions.

A.2.2   Delivery 1

The first chips received have been measured under [55]Fe and ^{90}Sr irradiation, from the front side. The back side of chip GRAY-6 has been also irradiated, but since the thickness of the chip is much higher than the penetration length of X-rays (see figure A.3), no data have been recorded. Table A.3 shows the list of measurements performed. All results have been compared with a standard INVESTIGATOR chip, called 252.

[55]Fe measurements

Results from [55]Fe measurements on MM 110 are shown in figure A.5. From the seed pixel signal (figure A.5a) of G-ray chips it is possible to see that the component of signal corresponding to

Chip	MM	Source	V_{bb} (V)
GRAY-1	110	^{55}Fe	-3, -6
	110	^{90}Sr	-6
GRAY-3	110	^{55}Fe	-6
GRAY-4	110	^{55}Fe	0, -6
	110	^{90}Sr	-6
GRAY-5	110	^{55}Fe	0,-1,-3,-6
	28	^{55}Fe, ^{90}Sr	-6
GRAY-6	110	^{55}Fe, ^{90}Sr	0,-1,-3,-6
	26, 27, 28	^{55}Fe, ^{90}Sr	-6
Standard chip 252	110	^{55}Fe, ^{90}Sr	0,-1,-3,-6

Table A.3 – List of measurements performed on G-ray chips from the first delivery.

the charge sharing is very small, compared with the same measurement performed on the standard INVESTIGATOR chip. By looking at the cluster multiplicity (figure A.5b), it is possible to observe the absence of charge sharing, while in case of the standard chip cluster multiplicity is higher than 1. This first results show no collection of charges that are not generated into the drift region.
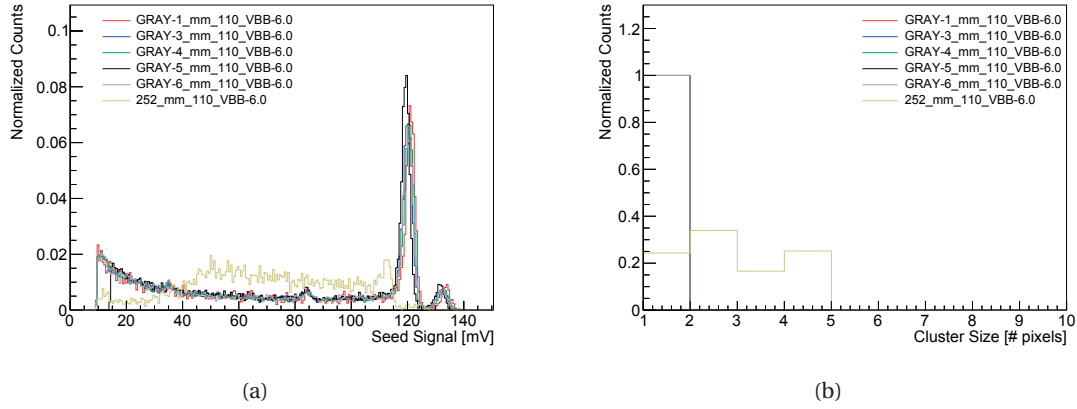

(a)   (b)

Figure A.5 – Seed signal (a) and cluster multiplicity (b) of ^{55}Fe measurements performed on MM 110, at $V_{bb} = -6$ V.

^{90}Sr measurements

Results from Sr90 measurements are shown in figure A.6. Also in this case, it is possible to observe the absence of charge sharing (by looking at the cluster multiplicity in figure A.6b). Moreover, the position of the peak of the seed signal (figure A.6a) is at around 250 electrons. This corresponds to 4.16 µm of sensitive layer. Similar measurements have been performed on MM 26, 27 and 28. In this case, the P-well width is decreasing from MM 26 to MM 28 (see Table II). The distance between two different N-wells is also decreasing, and therefore the

(a)   (b)
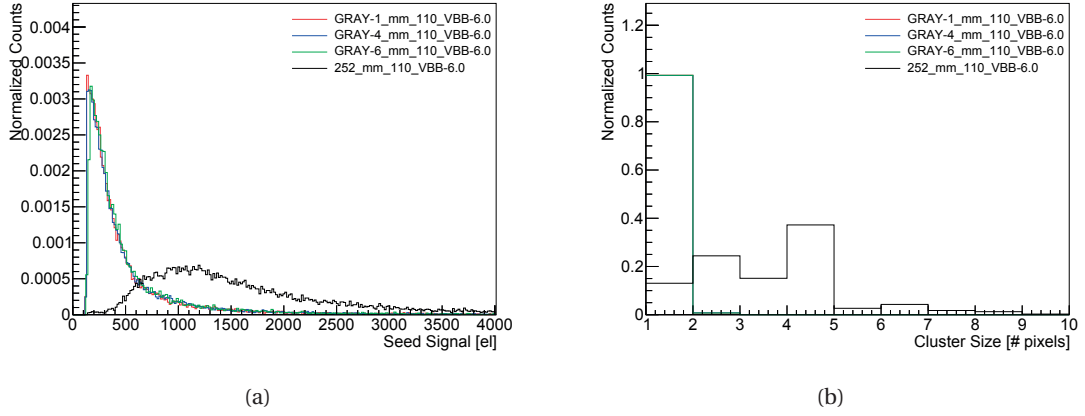
Figure A.6 – Seed signal (a) and cluster multiplicity (b) of ^{90}Sr measurements performed on MM 110, at $V_{bb} = -6$ V.

probability of having charge sharing should increase. The results are shown in figure A.7, and it is possible to observe that charge sharing increases from MM 26 to MM 28. The comparison
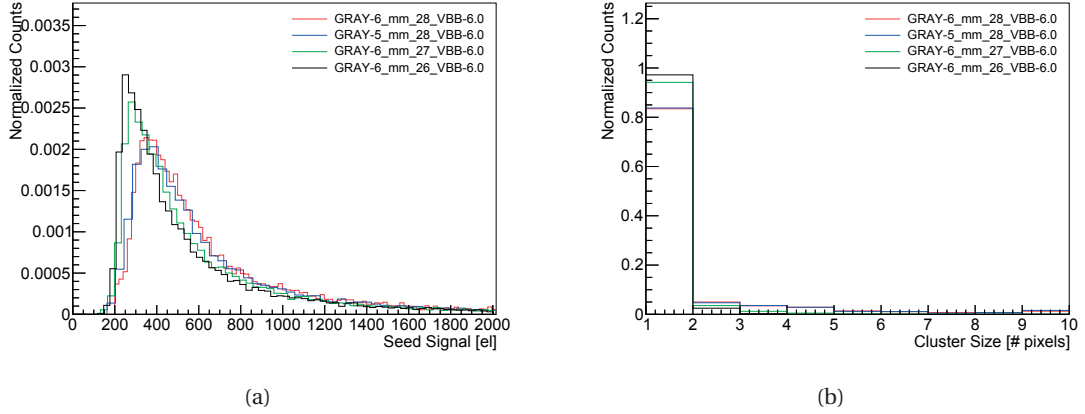

(a)   (b)

Figure A.7 – Seed signal (a) and cluster multiplicity (b) from measurements with ^{90}Sr on MM 26, 27 and 28, at bias voltage $V_{bb} = -6$ V.

with the standard chip 252 anyway shows that charge sharing in case of G-ray chips is much weaker than in the case of the standard chip (figure A.8).

Conclusions

From measurements on MM 110, it is difficult to draw conclusions on the properties of the bonding interface. Indeed, since the high resistivity bulk is 750 μm thick, charges diffusing into the bulk will be never reflected (as they are in case of epitaxial silicon, when reflection occurs at the junction with the low resistivity silicon). Therefore, the absence of charge sharing could be due to the trapping of charges at the bonding interface, or to the transmission into the bulk. Measurements on MM 26, 27 and 28 do not add any new conclusion, since the charge sharing
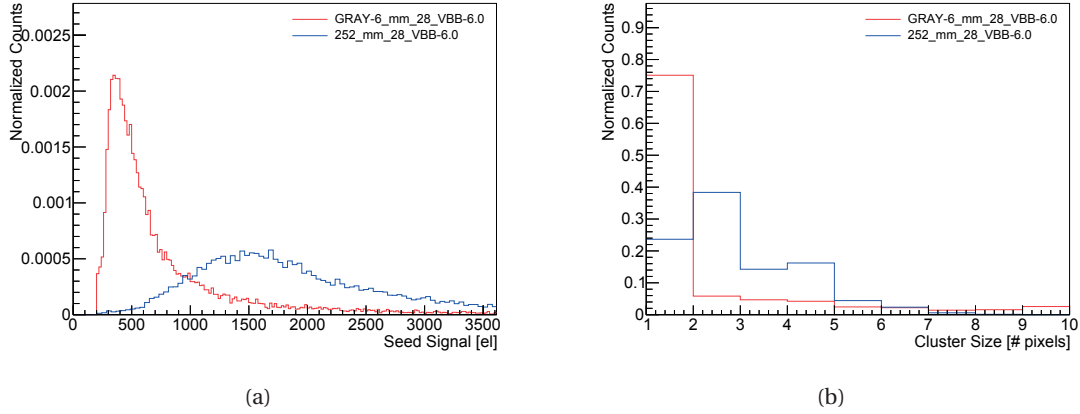
(a)   (b)

Figure A.8 – Comparison of seed signal (a) and cluster multiplicity (b) between chip 252 and GRAY-6 on MM 28, at bias voltage $V_{bb} = -6$ V.

that has been measured is too weak, and could occur in the silicon layer between the CMOS circuitry and the bonding interface.

A.2.3   Delivery 2

Chips from delivery 2 have been sent from G-ray to test the process uniformity on one wafer. Therefore they all come from the same wafer, taken from different positions. Table A.4 resumes the measurements performed on these chips that have been irradiated from the front side.

Chip	MM	Source	V_{bb} (V)
1C; 1E; 2B; 3B; 3F; 4F; 5C; 5D	28	^{55}Fe	-6

Table A.4 – Measurements on chips from second delivery.

Chip 3F was not working (the leakage current was too high, and therefore it was impossible to perform any analysis). The other chips show a similar behavior (figure A.9). Therefore, it is possible to conclude that the bonding process is uniform across the same wafer.

A.2.4   Delivery 3

In the third delivery, chips with different thicknesses have been tested. Table A.5 resumes the measurements performed on these chips.

^{55}Fe measurements

Since the thickness of the chips is much smaller than in the previous cases, it has been possible to measure a signal from back side irradiation with ^{55}Fe. Indeed, X-rays can penetrate through silicon, reaching the front side of the chip. Therefore, there should be both the contributions of drift and diffusion. Most of the generated charges will be located out of the depletion region, and therefore should be collected by diffusion, giving a charge sharing higher than
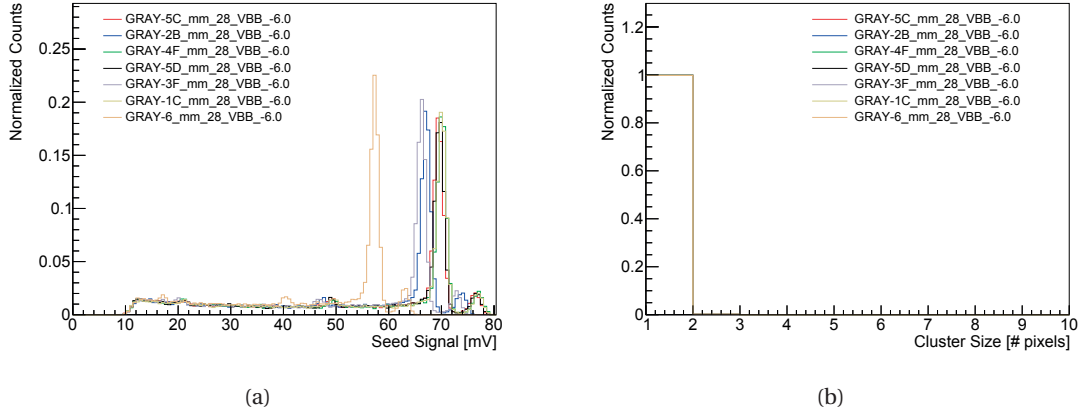
(a)

(b)

Figure A.9 – Seed signal (a) and cluster multiplicity (b) from measurements of chips from second delivery, on MM 28 at bias voltage $V_{bb} = -6$ V.

Chip	MM	Source	V_{bb} (V)
GRAY-55um	28	^{90}Sr	-6
GRAY-90um	28	^{90}Sr	-6
GRAY-55um	90	^{55}Fe	-6
GRAY-90um	90	^{55}Fe	-6
252	90	^{55}Fe	-6

Table A.5 – Measurements performed on thinned chips.

in the front side illumination case. Since ^{90}Sr electrons penetration length is bigger than the chips thickness, back and front side illumination measurements are similar. Results from ^{55}Fe measurements are shown in figure A.10. Measurements on the standard chip 252 have been performed, in order to have a comparison with the G-ray chips.
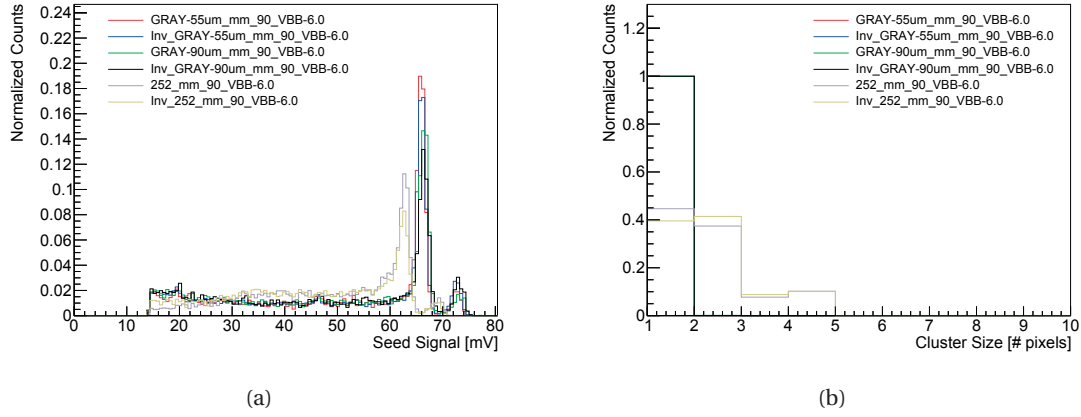

(a)

(b)

Figure A.10 – Seed signal (a) and cluster multiplicity (b) from ^{55}Fe measurements on thinned chips, on MM 90 at bias voltage $V_{bb} = -6$ V.

^{90}Sr measurements

Measurements with ^{90}Sr (figure A.11) are similar to the previous measurements of the chips from the first delivery (see figure A.6).
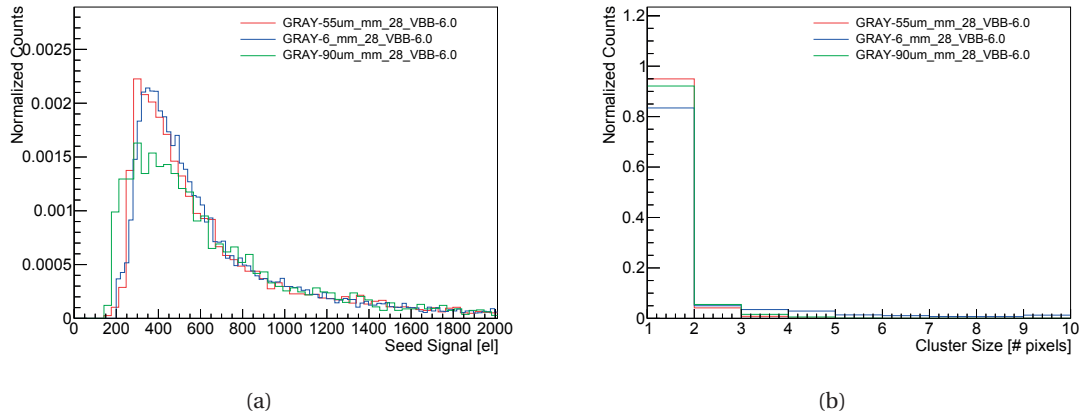

(a)

(b)

Figure A.11 – Seed signal (a) and cluster multiplicity (b) from ^{90}Sr measurements on thinned chips, on MM 28 at bias voltage $V_{bb} = -6$ V.

Conclusions

From these results, it is difficult to draw conclusions on the charge transfer across the bonding interface. Indeed, in case of back side illumination, X-rays can reach the upper part of the

bonded INVESTIGATOR (see figure A.1) in both cases, 55 µm and 90 µm (see figure A.3). Therefore, the obtained signal could come from charges that are generated between the CMOS circuitry and the bonding interface, and that do not need to pass through it to be collected. It is important to notice that, since the total thickness of the chips is much smaller than in the case of the first delivery, charges diffusing into the bulk should be reflected by the end of the chip. In this case, we should observe charge sharing, in both cases, front and back side illumination. The fact that the cluster multiplicity is always 1 could be a hint of the fact that the interface is blocking charges passage. This is valid for both ^{55}Fe and ^{90}Sr measurements.

A.2.5 Delivery 4

Chips from the last delivery have been bonded on a silicon epitaxial layer with high resistivity (larger than 1000 Ω cm), 20 µm thick, that has been grown on a low resistivity silicon bulk. By checking the powering of the chips, the first one (GRAY-1-epi) was not working properly, showing a high leakage current. Therefore, it was impossible to measure it. Table A.6 resumes the measurements performed on the second chip.

Chip	MM	Source	V_{bb} (V)
GRAY-2-epi	4, 110	^{55}Fe, ^{90}Sr	0, -3, -6

Table A.6 – Measurements performed on chips with bonded epitaxial layer.

^{55}Fe measurements

Results from ^{55}Fe measurements are shown in figure A.12 (for MM 110) and in figure A.13 (for MM 4). MM 4 has been used for the same reason of MM 28 (they are the MM with the minimum distance between two N-wells, see table A.2). The difference between these two mini-matrices is the position of the input transistor (for MM 4, it is outside the N-well, for MM 28 it is inside). From figures A.12 and A.13, it is possible to observe that measurements results are similar to the ones performed on G-ray chips from the first delivery (see figure A.5), as it is possible to see by comparing with measurements on GRAY-6.

^{90}Sr measurements

A similar result is obtained in case of ^{90}Sr measurements, shown in figures A.14 and A.15.

Conclusions

As in the previous measurements, also in this case it is difficult to draw conclusions on the charge transport across the bonding interface.

A.3 Conclusions

The measurements on bonded INVESTIGATOR chips cannot be used to draw conclusions on the charge sharing across the bonding interface. Indeed, in all cases, the absence of charge sharing could be due to trapping at the interface or diffusion into the bulk without any reflection. In case of measurements of thinned chips (delivery 3) and chips bonded on

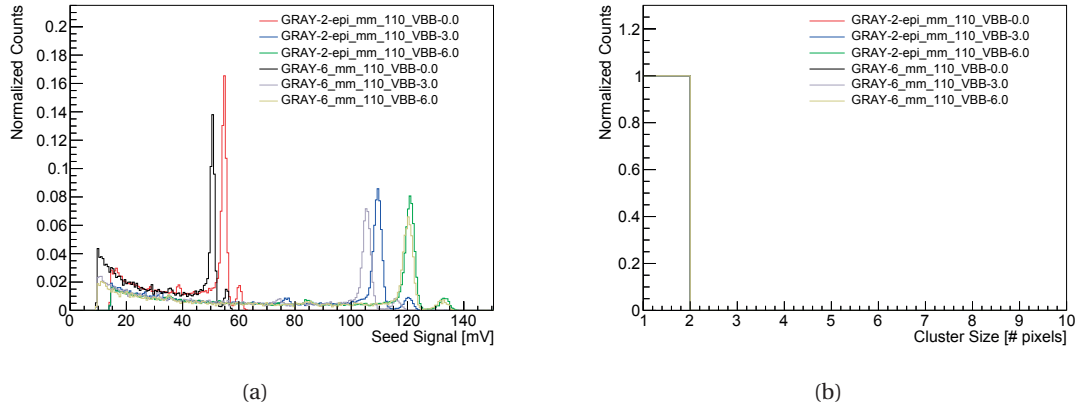Figure A.12 – Seed signal (a) and cluster multiplicity (b) from ^{55}Fe measurements on chips bonded on epitaxial silicon, on MM 110.
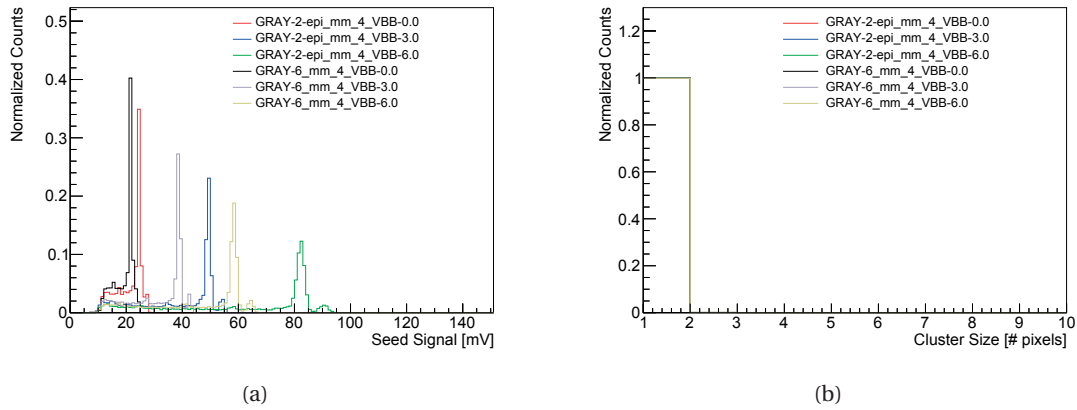

Figure A.13 – Seed signal (a) and cluster multiplicity (b) from ^{55}Fe measurements on chips bonded on epitaxial silicon, on MM 4.
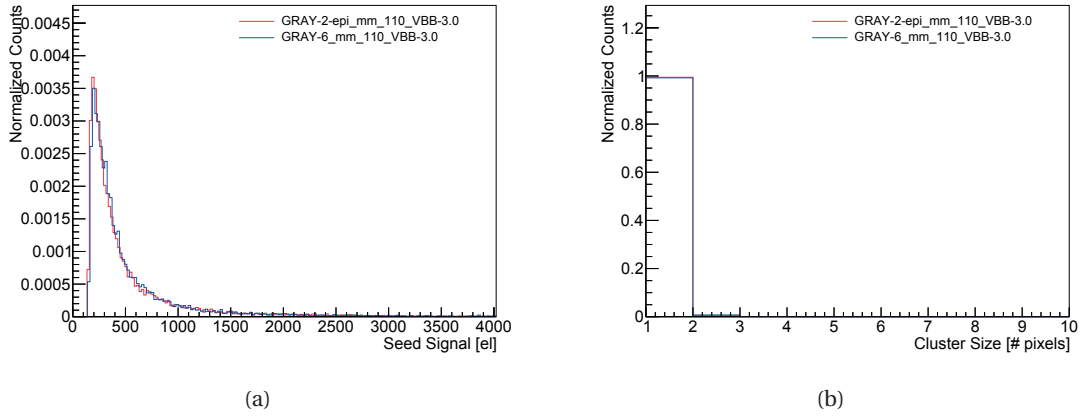
Figure A.14 – Seed signal (a) and cluster multiplicity (b) from ^{90}Sr measurements on chips bonded on epitaxial silicon, on MM 110.

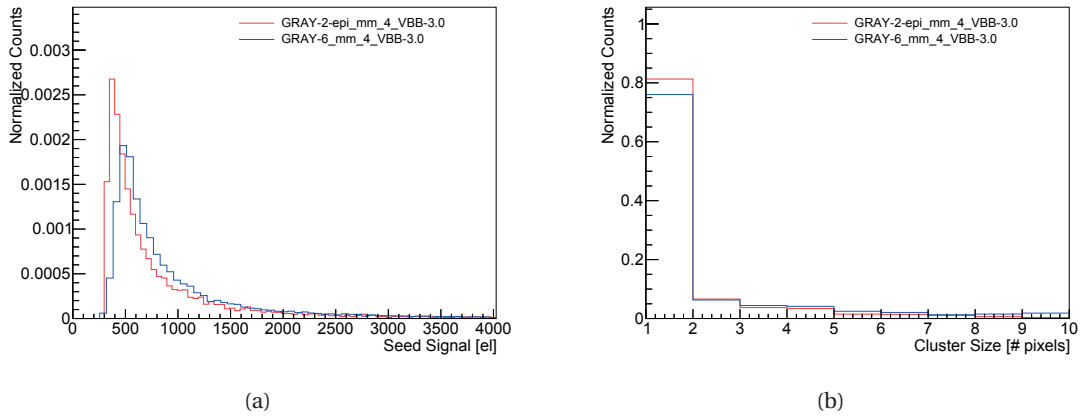Figure A.15 – Seed signal (a) and cluster multiplicity (b) from ^{90}Sr measurements on chips bonded on epitaxial silicon, on MM 4.

epitaxial silicon (delivery 4), one could expect the reflection of diffusing charges, and therefore charge sharing. In these two cases, its absence could indicate poor charge transport across the interface. These results could be consistent with the ones reported in chapter 3, that are that the bonding interface blocks the passage of generated charges through it, but due to the complexity of the test structures, it is difficult to draw a conclusion on these measurements (the absence of charge sharing could also be due to INVESTIGATOR chips damage during fabrication).

JACOPO BRONUZZI

Rue de Genève 79
1004 Lausanne (CH)

+41 (0)78 831 55 29

jacopo.bronuzzi@gmail.com

https://www.linkedin.com/in/jacopo-bronuzzi

19.10.1991

Italian

Italian (Mother tongue)

English (Fluent)

French (Fluent)

EDUCATION

EPFL, Lausanne, Switzerland – PhD September 2015 – September 2018	Doctoral program in Microsystems and Microelectronics
Politecnico di Torino, Torino, Italy; **INP de Grenoble**, Grenoble, France; **EPFL**, Lausanne, Switzerland – Master degree September 2013 – September 2015	Nanotechnologies for ICTs. Diplomas: ✓ **Diplôme d'ingenieur** ✓ **Laurea Magistrale**
Politecnico di Torino, Torino, Italy – Bachelor degree September 2010 – September 2013	Physics engineering. Diploma: ✓ **Laurea**

WORK EXPERIENCE ⋮ PROJECTS

CERN, Geneva, Switzerland **PhD project** September 2015 – August 2018	➢ Characterization of electrical properties of low temperature covalent bonding interface in silicon ➢ Design, modeling, fabrication and characterization of devices for electronic injection of charges in silicon, for characterization of radiation damage (TCT) ➢ Clean-room fabrication of metallic mockups of electronics chips for ATLAS experiment ➢ Characterization of silicon pixel detector performances ➢ Fabrication of silicon microchannels on the back side of electronic chips for cooling
CERN, Geneva, Switzerland **Master thesis internship** February 2015 – August 2015	➢ Fabrication of PMMA microchannels for applications in scintillation radiation detectors
IMEP-LAHC, Grenoble, France **Internship** June 2014 – August 2014	➢ Simulation and spectrum analysis of optical waveguides

PROFESSIONAL SKILLS

Micro and nano fabrication
- Photolithography and Electron beam lithography
- Dry and wet etching
- Lift-off
- Sputtering and evaporation deposition
- Dicing
- Wire bonding
- Silicon microchannels fabrication
- Diodes fabrication

Semiconductor devices modeling
- TCAD modeling of silicon devices
- Analytical modeling of silicon devices

Semiconductor devices characterization
- Transient Current Technique characterization
- CV characterization
- IV characterization
- Pixel detectors characterization and analysis

Programming languages
- C, C++, bash script, Matlab, VHDL

INTERESTS

✓ Climbing ⋮ ✓ Hiking ⋮ ✓ Snowboard ⋮ ✓ Music

List of publications

[1] J. Bronuzzi, A. Mapelli, M. Moll and J.M. Sallese. Principle and modelling of Transient Current Technique for interface traps characterization in monolithic pixel detectors obtained by CMOS-compatible wafer bonding. *Journal of Instrumentation*, 11:1-23, 2016

[2] J. Bronuzzi, A. Mapelli and J.M. Sallese. Analytical model for Transient Current Technique (TCT) signal prediction and analysis for thin interface characterization. *Journal of Instrumentation*, 11:1-6, 2016

[3] J. Bronuzzi et al. Principle of the electrically induced Transient Current Technique. *Journal of Instrumentation*, 13:1-16, 2018

[4] J. Bronuzzi et al. Transient Current Technique for Electrical Characterization of Bonded Interfaces in Bulk Silicon. *Journal of Applied Physics*, Submitted, 2018